

THE EFFECTS OF ALIGNMENT SEQUENCES ON A TWO-DIMENSIONAL KINEMATIC COUPLING

MASTER THESIS

F.M. van Ruiten BSc

S2096633

Precision Engineering (MS3)

Mechanical Engineering – Specialisation Robotics

Examination committee

Dr. Ir. J.J. de Jong EngD (Supervisor)

Prof. Dr. Ir. D.M. Brouwer EngD (Chair)

Dr. T. Mishra

June 19, 2025

**UNIVERSITY
OF TWENTE.**

Acknowledgements

Dear reader,

Before you is my thesis of the Master Mechanical Engineering. This research marks the end of my beautiful student time. This work not have been possible without the help and support of a number of people.

I would like to thank Jan de Jong for his supervision during the thesis. Our weekly meetings have taken my work to the next level. Next, I would like to thank Dannis Brouwer and my fellow students of the precision engineering department for their input during the graduation process.

My work in the lab would not have been possible without the advice of Roy Kooijman. Special thanks goes to Andre Eppingbroek of TCO for the excellent production of the leaf spring mechanism. The supporting staff of the Cube delivered the other aluminium parts for the test set-up fast as well.

The thesis support group of Deirdre Brandwagt got me on track and kept me sane during the process. Thanks to all my friends who kept up with me, especially Marlize Kramer, Carlijn Grimberg and Thijmen Masin.

Furthermore, my family has always supported me. Special thanks goes out to my mother, who read my report and improved my grammar and sentence structures. Any mistakes which are still left are entirely up to me.

Finally I want to thank my boyfriend, Jorrit Elgersma. He not only gave me mental support during the long university days and late nights, but also proofread parts of my report and acted as my personal help-desk.

I did not use AI for this entire research, because friends and family are infinitely better.

Glossary

Symbol	Description	Unit
s_v	Virtual play	mm
W	Friction force	N
c	Stiffness	N/mm
F_{nest}	Nesting force	N
M_{nest}	Nesting moment	Nmm
F_i	Force of point i	N
$F_{n,i}$	Normal force of point i	N
$F_{t,i}$	Tangential force of point i	N
$l_{c,i}$	Location contact i	mm
$l_{F,x}$	Location nesting force x-direction	mm
$l_{F,y}$	Location nesting force y-direction	mm
h	Height of the chuck	mm
w	Width of the chuck	mm
α	Angle of the nesting force	rad
μ_i	Friction coefficient of point i	—
E^*	Reduced modulus of elasticity	MPa
E	Modulus of elasticity	MPa
ν	Poisson ratio	—
r	Ball radius	mm
G	Shear modulus	MPa
$\delta_{n,i}$	Normal indentation of contact i	mm
$\delta_{t,i}$	Tangential indentation of contact i	mm
a_i	Contact radius of point i	mm
x	x-location of the centre point of the chuck	mm
y	y-location of the centre point of the chuck	mm
θ	Rotation of the centre point of the chuck	rad
R	Rotation matrix	
X	x- and y-location of all contact points of the chuck. (Including z-location in 3D)	mm
X_0	x- and y-location of the centre point of the chuck. (Including z-location in 3D)	mm
X_i	x- and y-location of point i . (Including z-location in 3D)	mm
X_n	Locations of the normal directions of all contact points of the chuck	mm
X_t	Locations of the tangential directions of all contact points of the chuck	mm
x_i	x-location of point i	mm
y_i	y-location of point i	mm
z_i	z-location of point i	mm
$dx_{slip,i}$	Slip in x-direction of point i	mm
$dy_{slip,i}$	Slip in y-direction of point i	mm
$s_{v,x}$	Virtual play in x-direction	mm
$s_{v,y}$	Virtual play in y-direction	mm
$F_{a,i}$	Applied force of point i	N
$x_{s,i}$	Measured x-location of sensor i	μm
$y_{s,i}$	Measured y-location of sensor i	μm
σ_x	Standard deviation in x-direction of measured test results	μm
σ_y	Standard deviation in y-direction of measured test results	μm
$k_{n,i}$	Normal stiffness of point i	N/mm
$k_{t,i}$	Tangential stiffness of point i	N/mm
γ	Angle of tangential force in 3D situation	rad

$l_{a,i}$	Screw eye location of applied force i	mm
$l_{s,i}$	Location of sensor i	mm
X_{crit}	Point where friction coefficients become critical for self-locking	mm
c_{plane}	In plane stiffness of leaf spring mechanism	N/mm
c_{fold}	Stiffness of one folded leaf spring in the direction of the fold	N/mm
c_z	Stiffness in z-direction (out of plane-direction) of leaf spring mechanism	N/mm
I	Area moment of inertia	mm^4
l	Length of leaf spring	mm
w	Width of leaf spring	mm
t	Thickness of leaf spring	mm
β	Maximum angle between plates friction test	$^\circ$

Table of contents

Acknowledgements -----	iii
Glossary -----	iv
Table of contents -----	vi
Abstract -----	1
1. Introduction -----	1
2. Planar kinematic coupling models -----	4
2.1 <i>Virtual play model</i> -----	4
2.1.1 Finding the virtual play-----	4
2.1.2 Friction model-----	4
2.1.3 Contact deformations-----	5
2.1.4 Virtual play of the chuck-----	5
2.2 <i>Alignment model</i> -----	6
2.3 <i>Numerical results</i> -----	7
2.3.1 Mathematical values virtual play model--	7
2.3.2 Influence of friction-----	7
2.2.3 Mathematical values initial positioning---	7
3. Design of the test set-up -----	8
3.1 <i>Design requirements</i> -----	8
3.2 <i>Final design</i> -----	8
4. The experiment -----	9
4.1 <i>Method</i> -----	9
4.2 <i>Experiment A: Validation of the test set-up</i> ---	10
4.2.1 Tightening effects-----	10
4.2.2 Determining stiffnesses-----	11
4.3 <i>Experiment B: Repeatability results</i> -----	11
5. Discussion -----	12
6. Conclusion -----	13
Literature -----	14

Appendices -----	17
<i>Appendix A: Ideal model</i> -----	17
<i>Appendix B: Non-linear model</i> -----	18
<i>Appendix C: Deformation model</i> -----	19
<i>Appendix D: Three-dimensional expansion</i> -----	21
<i>Appendix E: Dimensions material properties</i> -----	22
<i>Appendix F: Values virtual play model</i> -----	23
<i>Appendix G: Maximum friction coefficient for no self-locking</i> -----	24
<i>Appendix H: Values alignment model</i> -----	25
<i>Appendix I: Alignment model for maximum friction</i> -----	28
<i>Appendix J: Concept generation</i> -----	29
<i>Appendix K: Detailed design</i> -----	35
<i>Appendix L: Friction test</i> -----	44
<i>Appendix M: Technical drawing ball holder</i> -----	45
<i>Appendix N: Technical drawing contact plates</i> ---	46
<i>Appendix O: Optimising leaf flexure design</i> -----	47
<i>Appendix P: Checking displacements and stresses leaf spring design</i> -----	49
<i>Appendix Q: Calibration sheets capacitive sensors</i> -----	53
<i>Appendix R: Loadcell calibrations</i> -----	56
<i>Appendix S: Extra holes angled blocks</i> -----	57
<i>Appendix T: Bill of materials test set-up</i> -----	59
<i>Appendix U: Assembly plan test set-up</i> -----	61
<i>Appendix V: Determining offset value capacitive sensors</i> -----	69
<i>Appendix W: Sensor noise test set-up</i> -----	70
<i>Appendix X: Determining the flexure stiffness</i> -----	72
<i>Appendix Y: Standard deviations experiment B</i> ---	73

Abstract

Industry uses kinematic couplings to repeatedly align two parts together with high tolerances. Research in the failure of kinematic couplings does not focus on the conjunction of compliance and friction. In this thesis a two-dimensional model is developed to predict the virtual play based on both factors. A second model is introduced to model the effect of alignment sequences on the initial positioning of kinematic couplings. A test set-up is made to validate both models for two-dimensional kinematic couplings. The virtual play of the test set-up is in the same order as the model. Model calculations gave for a nesting force of $70N$ a virtual play of $s_{v,x} = 2.74\mu m$ and $s_{v,y} = 0.70\mu m$. The displacement variations of the experiments led to $s_{v,x} = 6.39\mu m$ and $s_{v,y} = 2.55\mu m$. Hysteresis showed up in the contact points due to slip, which led to calibration errors. Using a specific alignment sequence improved the displacement variations to $s_{v,x} = 0.14\mu m$ and $s_{v,y} = 0.49\mu m$. If uncertainties while testing will be controlled better, this improvement might be even more. The test set-up should also be useful within future research to validate expanded virtual play models. By expanding the presented research to the three-dimensional world, the repeatability of kinematic couplings could be improved.

1. Introduction

Manufacturing processes in precision industry require really tight tolerances. For positioning of lasers, as example, alignments are necessary within tens of micrometres [1]. Manipulators can be used to acquire this which add complexity, computation time and are quite expensive. They are not suitable when parts need to be (de)coupled often. Kinematic couplings are used to avoid these costs [2], [3].

A kinematic coupling is a connection of two parts making contact, which will be represented with one fixed world to which a moving part aligns. The moving part will be referred to as “chuck” from now on, and the fixed world as the “base”. Ball-surface contact is made at six points which restrain the six degrees of freedom. In the ideal, thus frictionless case the coupling is exactly constraint. To make sure the parts stay together, a so-called nesting force is applied on the moving part. Typically the nesting force is chosen such that contact forces are equal [4].

Figure 1 shows the two most well-known couplings: the Maxwell coupling and the Kelvin clamp. The Maxwell coupling, which is also called the three-vee coupling, has a symmetric design. This leads to more uniform contact stresses, thermal expansion about a central point and reduced manufacturing costs due to identical features. The Kelvin clamp has a natural pivot point for angular adjustments due to the tetrahedral socket [2].

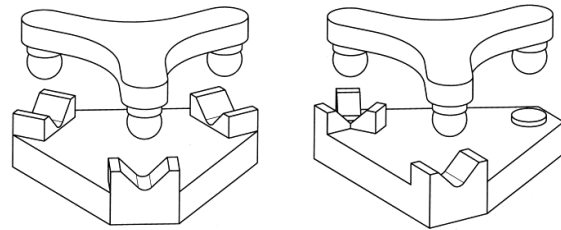


Figure 1: Maxwell coupling & Kelvin clamp [5]

In literature several different layouts have presented due to space constraints of applications. Three to six balls at the chuck or the base lead to six contact points.

Although in theory the kinematic couplings are precise, this does not always show in practical applications. Slocum [2] has an overview of many applications and design ideas. In his paper he states: “Controlling deformation and friction at the contact interface are keys to achieving a high level of repeatability.”

Compliances of materials cause the balls and surfaces to deform. The material acts like a spring, wherefore the final position shifts compared to the rigid case. If material properties and forces are not known, this final position becomes uncertain. Slocum [4] made a spreadsheet based on Hertzian contact deformations to make it easier for designers to see the effect of their design choices on how well their coupling is expected to work.

The friction forces are the additional forces acting orthogonal between the surfaces, hindering the sliding motion. As long as parts are not moving, the direction of the friction forces are unknown. The system is not exactly constraint anymore compared to the ideal frictionless case.

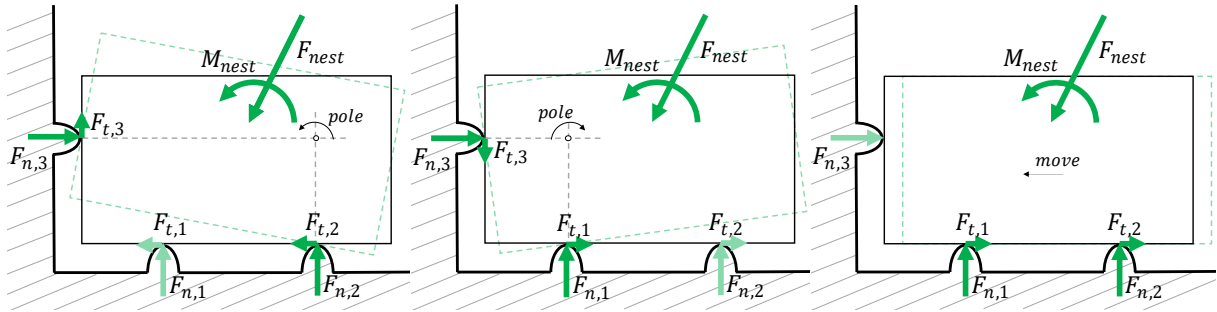


Figure 2: The three different alignment routes of a planar kinematic coupling with expected nesting forces

Weighert et al. [6] made a finite element model for the transition between sticking and sliding of contacts. However, no absolute reproducibility predictions could be made due to uncertainty of friction coefficients.

All uncertainties of a kinematic coupling together lead to a mounting error. This is the difference between the final position and expected position of the coupling. A coupling has a high precision if it aligns well at a chosen position. The error can happen due to both the interchangeability errors and the repeatability errors [7].

The interchangeability error will be seen as the accuracy error of a kinematic coupling. When this error is small it means the average positioning of different alignment combinations are close to each other. The chuck might be interchanged between different frames, while giving the same results.

The repeatability is the way the repositioning of one coupling yields the same result every time. If all alignments of one combination are close together, the repeatability error is small. Most ideal both the interchangeability and repeatability error are small, since the total mounting error is the sum of both.

A possible reason for interchangeability errors are the manufacturing tolerances. Hart et al. [7] introduced a calibration process to reduce the interchangeability error based on measurements of specific parts of the couplings. The error is reduced to the measurement error of the procedure.

Culpepper and Mangudi [8] tried to improve the precision accuracy in a more active way by adjusting the surfaces with piezo-electric actuators. Using closed-loop control, they shift the contacting points to specific positions. Differences for couplings show up due to manufacturing and assembling tolerances. The actuators prevent

frictional sliding from happening during alignment. The precision limit is reached by the electronic capability driving the actuators.

During alignment, the chuck does not come into contact with all points at the same time. One by one the balls touch the surfaces, until static equilibrium is found. Veugelers [9] states the final contact will determine the limiting friction coefficient. Therefore, there are 3 different alignment routes (Figure 2). These alignment routes will cause different ways of establishing equilibrium.

It might happen the initial positioning is not even determined by all contacts. A problem that might show up during alignment is self-locking. Friction forces need to be temporary overcome while aligning to make contact in all points. Self-locking occurs when not all 6 contacts engage during the alignment procedure. The coupling may not make contact at all points if it finds an equilibrium position due to the friction forces. This causes uncertainty in where the chuck is, since all degrees of freedom are constrained without all contacts meeting.

Hale [10] made a frictional model to calculate the limiting friction coefficients the contacts may have, to prevent friction from taking place. The orientation of the nesting force plays a role as well. Hale [11] adjusts angle of V-grooves to optimise this friction coefficient.

Hale and Slocum give additional guidelines for applying the nesting force, to prevent self-locking from taking place [5]. The models are based on the assumption the friction forces are expected to align opposite to the moving direction. Research of Patti and Vogels [12] shows this is not always the case. When the parts are not moving, the friction force causes unknown elastic

deformations which can cause different orientations of the friction force. Therefore, locking might occur even when the previous model does not predict it. This leads to the so-called worst-case theory. Using this model these different orientations are taken into account. The direction of the nesting force will be chosen better. Veugelers [9] and Neulen [13] designed a test set-up for their master theses to validate this theory.

After contact is made, the uncertainties will lead to repeatability problems. The extent to which a kinematic coupling aligns properly can be defined with the virtual play of the system. The virtual play gives a range of uncertainty in which the final position of the kinematic coupling will be. It is often showed with a hysteresis loop. "Hysteresis can be viewed as memory mechanism" [14, p.156]. When loading and unloading a structure, uncertainty factors cause the final position to be different with the same force. The virtual play is a measure of repeatability and does not look at the interchangeability of the final position.

There are possibilities to reduce the virtual play. Schouten et al. [15] designed a kinematic coupling with elastic hinges to become self-adjusting surfaces. This way the hysteresis due to disturbance forces or temperature deviations was reduced by 95%.

All previous mentioned research focuses on the way contact is made and how the two parts of a coupling align. Due to the research the field also expanded outside the kinematic couplings. Innovative ideas developed which led to the quasi-kinematic coupling among other things. These couplings are based on lines of contact instead of point contacts [16], [17]. The advantage of these lines of contact is they can handle higher loads than the point contacts.

Furthermore, a design made by Ziegert and Tymianski [18] uses air bearings to avoid the friction effects to increase the repeatability. Due to fluctuations in air pressure, this design did not lead to higher repeatability, although it could handle higher loads than standard kinematic couplings. As nice bonus, the design did not lead to degradation due to wear, although sliding couplings do.

Previous discussed models design their couplings either with friction as a basis for research or focus on the deformations and stiffnesses while neglecting friction entirely. Even when designing a coupling for a specific use situation friction is often excluded. An example of this is the research of De Benedictis and Ferraresi [19] who did a feasibility study for a robotized laser-cutting machine. A part of the uncertainty is not included in the model. Another research designing stress-free kinematic couplings based on temperature differences, also neglects friction, while it is likely it plays a role due to the deformations [20]. The link between friction and deformations has not been researched often.

One recent study conducted by Fan et al. [21] does focus on both deformations and friction. A model was developed for repeatability of a kinematic coupling based on both compliance and friction. The effect of friction is however used mainly to take a look at the wear of the surfaces. Due to higher friction, higher wear is predicted, which seems to improve the repeatability. This is contrasting previous research which mentions virtual play is smaller for lower friction, due to less virtual play [2]. It is good to note this research is not verified with experiments. How the friction itself influences the virtual play is not taken into account.

Although both deformation and friction have been researched, a complete analytic description for the virtual play seems to be missing. For this thesis a full equilibrium model of a chuck will be developed to predict the virtual play based on the friction and compliances of the system.

Next to the virtual play model an alignment model will be developed to investigate the influence of the alignment sequence. It is possible to adjust the order of contact when aligning a kinematic coupling, so it will be researched if the repeatability can be improved in this way. This is the aim of this thesis. A test set-up will be designed to validate the models and alignment sequence.

To keep the scope clear, the research will be persecuted on two-dimensional asymmetric kinematic couplings. Two-dimensional couplings are planar moving couplings. This means there are only three degrees of freedom. Three contacts are needed to fully restrain a chuck. The model is

chosen to be asymmetric to gain insights in the influence of different alignment sequences.

A mathematical model made to predict virtual play is introduced in chapter 2. Section 2.2 shows the model with the effect of the alignment sequence. Numerical values for both models are given at the end of chapter 2. The test set-up is introduced in chapter 3. The results of the experiments follow in chapter 4. Chapters 5 and 6 will lead to the discussion and conclusion of this research.

2. Planar kinematic coupling models

2.1 Virtual play model

2.1.1 Finding the virtual play

Virtual play for one contact can be found based on the hysteresis model of Soemers for friction and compliance [14, p.155] the virtual play is calculated as $s_v = 2 \frac{|W|}{c}$ (1).

where W is the friction force and c is the stiffness. Unfortunately, the hysteresis model cannot be applied for the total chuck. Seubers [3] already showed a possibility to remodel a kinematic coupling to make this possible. However, the tangential stiffnesses of the contacts are not taken into account in his model. The influence of separate contacts on the total virtual play cannot be retraced. A new approach will be presented in this chapter. In section 2.1.2 a friction model will be introduced to calculate the normal and tangential forces. Based on these values, displacements of each contact will be calculated using the Hertzian contact model as explained in section 2.1.3. Using these values the virtual play of the total chuck will be calculated as explained in section 2.1.4. The alignment model is explained in section 2.2. Values for a use situation are generated in section 2.3.

2.1.2 Friction model

When the chuck is nested, the contact forces are displayed as a combination of normal and tangential forces (Figure 3). A nesting force and moment are applied to align the chuck. The chuck will be assumed rigid for the sake of the model.

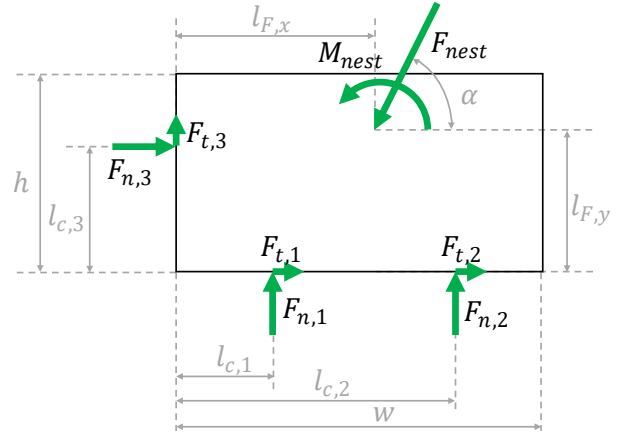


Figure 3: Normal and tangential forces for a nested chuck

This leads to the generalised equilibrium equations

$$\begin{aligned} \Sigma F_x &= F_{n,3} - \cos(\alpha)F_{nest} + F_{t,1} + F_{t,2} = 0 \\ \Sigma F_y &= F_{n,1} + F_{n,2} - \sin(\alpha)F_{nest} + F_{t,3} = 0 \quad (2). \\ \Sigma M &= l_{c,1} \cdot F_{n,1} + l_{c,2} \cdot F_{n,2} - l_{c,3} \cdot F_{n,3} + M_{nest} \\ &+ \cos(\alpha)F_{nest} \cdot l_{n,y} - \sin(\alpha)F_{nest} \cdot l_{n,x} = 0 \end{aligned}$$

in which F_{nest} and M_{nest} are the nesting force and moment, $F_{n,i}$ are the contact normal forces at contact $i \in \{1,2,3\}$, $F_{t,i}$ the corresponding tangential contact forces and $l_{c,i}$ the corresponding locations, α is the angle of the nesting force and $l_{F,x}$ and $l_{F,y}$ the nesting locations all as defined in Figure 3. The ideal case with normal forces only is given in Appendix A.

It is good to note the equilibrium equations are linearised due to the small displacements. Appendix B briefly touches upon expanding to a non-linear model.

The tangential forces are linked to the normal forces by $F_{t,i} \leq \mu_i \cdot F_{n,i} \forall i \in \{1,2,3\}$ (3).

Here μ_i shows the maximum friction coefficients of each contact which are based on material choices. For maximal tangential forces this becomes an equality relation.

Equation (2) is expanded with the maximum tangential forces to find the normal and tangential displacements. To simulate opposite directions of friction, the friction coefficients will also be taken maximum negative in (3). The virtual play will now be generated by calculating the different possible solutions based on the maximum friction coefficients. The friction in each contact will either be the maximum coefficient in the positive or negative direction. This leads to 8 different equilibrium positions.

2.1.3 Contact deformations

Using the forces found with the friction model, the displacements are calculated using the Hertzian contact model. This model describes the indentations based on forces working on the ball contact. It is important to notice the deformation of the contact points happens due to both deformations of the chuck and of the balls. As mentioned, the chuck will be assumed rigid for the sake of the model, but the possible indentations of the chuck will still be modelled in the balls at the base. The normal indentation of a spherical contact is given in Johnson [22, p.93]

$$\delta_{n,i} = \left(\frac{9}{16 \cdot r \cdot E^*} \right)^{\frac{1}{3}} \cdot F_{n,i}^{\frac{2}{3}} \quad (4)$$

with, r the ball radius and E^* the reduced modulus of elasticity. The reduced modulus of elasticity is based on both materials which make contact [23]

$$\frac{1}{E^*} = \frac{1-\nu_b^2}{E_b} + \frac{1-\nu_s^2}{E_s} \quad (5)$$

Here ν is the Poisson ratio of the ball and surface and E is the modulus of elasticity.

Equation (4) uses the secant stiffness $\frac{F_{n,i}}{\delta_{n,i}}$. The local stiffness is found by differentiation [24]

$$\frac{dF_{n,i}}{dX_{n,i}} = \frac{3}{2} \cdot \left(\frac{16 \cdot r \cdot E^* \cdot F_{n,i}}{9} \right)^{\frac{1}{3}} = \frac{3}{2} \cdot \frac{F_{n,i}}{\delta_{n,i}} \quad (6)$$

This equation shows the local and secant stiffnesses differ with a factor $\frac{3}{2}$. For the model the secant stiffness will be used, which deforms negatively for positive forces, due to the rigidity assumption of the chuck. In the tangential direction, the displacement is linear with the tangential force for no slip [22, p.217]

$$\delta_{t,i_{no_slip}} = \frac{F_{t,i}}{8a_i} \left(\frac{2-\nu_b}{G_b} + \frac{2-\nu_s}{G_s} \right) \quad (7)$$

where a_i is the contact radius and G is the shear modulus of the ball and surface.

However, when using the friction model partial slip will take place. This leads to [22, p.219]

$$\delta_{t,i_{slip}} = \frac{3\mu_i F_{n,i}}{16a_i} \left(\frac{2-\nu_1}{G_1} + \frac{2-\nu_2}{G_2} \right) \left[1 - \left(1 - \frac{F_{t,i}}{\mu_i F_{n,i}} \right)^{\frac{2}{3}} \right] \quad (8)$$

Since in our case $F_{t,i} = \mu_i F_{n,i}$ this differs with a factor $\frac{3}{2}$ with (7). The total displacement is still not linear, since this stiffness depends on the contact radius. The contact radius depends on the normal

$$\text{force as [22, p.93]} \quad a_i = \left(\frac{3 \cdot r \cdot F_{n,i}}{4E^*} \right)^{\frac{1}{3}} \quad (9)$$

The total tangential stiffness is given as

$$\delta_{t,i} = \frac{3}{2} \cdot F_{t,i} \left(\frac{E^*}{384 \cdot r \cdot F_{n,i}} \right)^{\frac{1}{3}} \left(\frac{2-\nu_b}{G_b} + \frac{2-\nu_s}{G_s} \right) \quad (10)$$

It is possible to calculate the displacements and forces purely based on these compliances, without taking the friction forces into account (Appendix C).

2.1.4 Virtual play of the chuck

After the alignment takes place, the final position of the chuck seems determined by 3 distinct types of motions: deformations of the contact points, rolling the chuck over the balls and the relative tangential locations of the contact points. Figure 4 splits up these motions. The relative contact happens both due to the uncertainty in the initial contact places and sliding from the chuck over the base when friction forces are overcome.

On the whole the virtual play will be expressed in the three degrees of freedom of the centre of the chuck; x , y and θ . Since the chuck is constraint at the contacts, the positions of all contacts will determine the position of the chuck. This results in six positions wherefore it may seem like overconstraints are introduced in the system. The slip of the tangential displacements releases these degrees of freedom and will also be calculated now. Figure 5 shows the displacements of the chuck itself are only based on the normal displacements of the contacts.

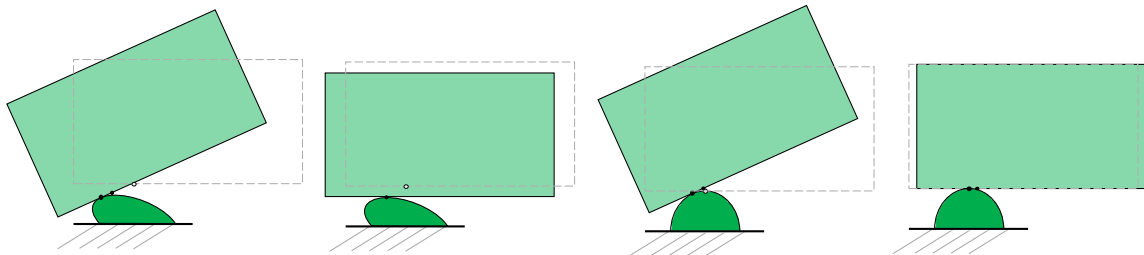


Figure 4: Final position of a contact point: total, based on deformations, based on rolling & based on relative tangential movements

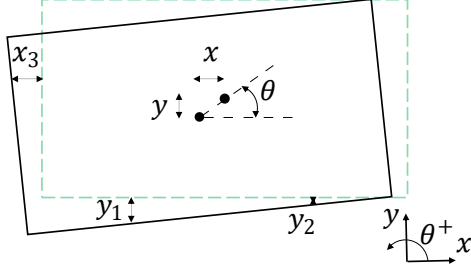


Figure 5: Virtual play chuck based on normal displacements contact points

The contacts are linked to the centre of the chuck by the separate motions

$$dX = dX_{deform} + dX_{rolling} + dX_{slip} =$$

$$\begin{bmatrix} \delta_{t,1} \\ \delta_{n,1} \\ \delta_{t,2} \\ \delta_{n,2} \\ \delta_{n,3} \\ \delta_{t,3} \end{bmatrix} = \begin{bmatrix} dX_0 \\ dX_0 \\ dX_0 \end{bmatrix} + \begin{bmatrix} dRX_1 \\ dRX_2 \\ dRX_3 \end{bmatrix} + \begin{bmatrix} dx_{slip,1} \\ dx_{slip,2} \\ 0 \\ 0 \\ 0 \\ dy_{slip,3} \end{bmatrix} \approx$$

$$\begin{bmatrix} dx + d\theta \frac{h}{2} + dx_{slip,1} \\ dy + d\theta \left(l_{c,1} - \frac{w}{2} \right) \\ dx + d\theta \frac{h}{2} + dx_{slip,2} \\ dy + d\theta \left(l_{c,2} - \frac{w}{2} \right) \\ dx + d\theta \left(\frac{h}{2} - l_{c,3} \right) \\ dy - d\theta \frac{w}{2} + dy_{slip,3} \end{bmatrix} \quad (11).$$

Here $X_0 = \begin{bmatrix} x \\ y \end{bmatrix}$ are the positions of the centre of the chuck, which are starting in the origin. R is the rotation matrix, h is the height of the chuck, w the width and $dx_{slip,i}$ and $dy_{slip,i}$ the slip of the points in respective directions. The initial position of the contacts are given as

$$X_{initial} = \begin{bmatrix} X_1 \\ X_2 \\ X_3 \end{bmatrix} = \begin{bmatrix} -\frac{w}{2} + l_{c,1} \\ -\frac{h}{2} \\ -\frac{w}{2} + l_{c,2} \\ -\frac{h}{2} \\ -\frac{w}{2} \\ -\frac{h}{2} + l_{c,3} \end{bmatrix} \quad (12).$$

where X_i is the x- and y-location of point i . The displacements are based on the assumption the deformations are small. The rotations are linearised around θ , which gives

$$dR = \begin{bmatrix} \cos(d\theta) - 1 & -\sin(d\theta) \\ \sin(d\theta) & \cos(d\theta) - 1 \end{bmatrix} \approx \begin{bmatrix} 0 & -d\theta \\ d\theta & 0 \end{bmatrix} \quad (13).$$

The tangential displacements are used to calculate the slip of the contact points. It is good to note the Hertzian contact model is used based on the assumption of partial slip, so the slip should not become too high. The expansion of these models to three-dimensional models is given in Appendix D.

2.2 Alignment model

As mentioned in the introduction the final point which makes contact leads to the limits of the models. To observe the influence of different alignment sequences, the three separate cases will be modelled. Equilibrium equations are still given by (2).

Since the last contact has the main influence on the displacements, it can be assumed the last contact will not slide on the contrary to the other two points. The tangential forces will be assumed maximal according to (3) in the first two points making contact, while the last point stays in the uncertain range. By modelling the final point which makes contact with deformations only (Figure 6) the slip will not show up in (11).

For example, when point 1 is the final contact point this leads to

$$\begin{aligned} F_{t,1} &\leq \mu_1 F_{n,1} \text{ with } dx_{slip,1} = 0 \\ F_{t,2} &= \mu_2 F_{n,2} \\ F_{t,3} &= \mu_3 F_{n,3} \end{aligned} \quad (14).$$

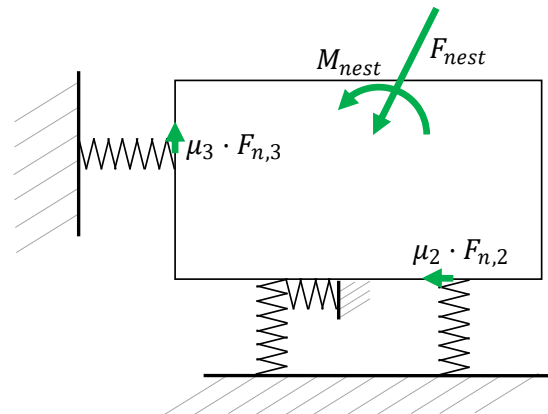


Figure 6: Alignment model with contact 1 as final meeting point

The system cannot be solved step by step like the virtual play model. A numerical solver will be used to find the final displacements. Equation (2)

and (4) are still used for equilibrium relations and normal displacements. Equation (7) needs to be used to calculate the tangential forces for point 1 while (10) needs to be used for points 2 and 3. By expressing everything with (14) in (11) the final position, the results are calculated. This time 4 possible friction positions are left per contact point.

It is possible the tangential forces calculated are actually leading to slip. This is the case when $\frac{|F_{t,i}|}{|F_{n,i}|} > \mu$ for the final contact point. By calculating the factor $\frac{F_{t,i}}{F_{n,i}}$ and comparing it with the friction coefficients it is determined when sliding takes place. In those cases the final contact point will be calculated based on the friction coefficient like the virtual play model. The direction of the friction will be chosen positive if the factor is positive and negative if the factor is negative.

2.3 Numerical results

2.3.1 Mathematical values virtual play model

The virtual play model is run for a nesting force of 70N and moment of 470Nmm. Dimensions and material properties are given in Appendix E. Figure 7 shows the results, with the corresponding values for each separate run in Appendix F. Rotations are not shown since they are small.

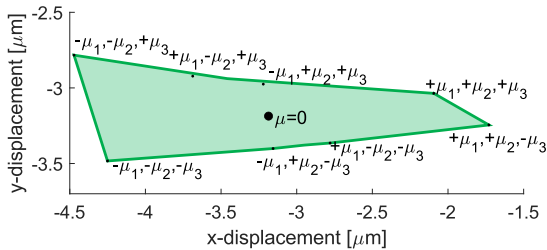


Figure 7: Displacements of the chuck centre for steel on aluminium contact

It can be observed in the figure point 3 has the main influence on the y-displacement, while point 1 and 2 together influence mainly the x-displacement. This seems logical with the way the model is set up. The total virtual play in x-direction is $s_{v,x} = 2.74\mu m$ and in y-direction $s_{v,y} = 0.70\mu m$. It is clear the virtual play in the x-direction is bigger than the y-direction. This is probably due to the fact mainly point 3 is limiting the chuck in x-direction and both point 1 and 2 limit displacements in y-direction.

2.3.2 Influence of friction

The virtual play is calculated for multiple friction coefficients to check the influence of friction. Figure 8 shows the plotted results.

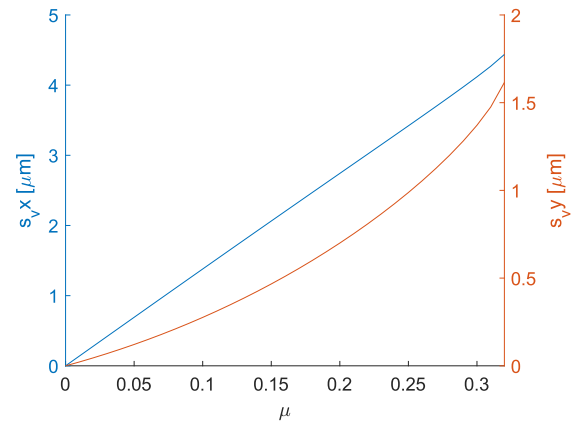


Figure 8: Maximum virtual play based on all friction directions for different friction coefficients

The figure shows the virtual play becomes larger for higher friction coefficients. In the x-direction this seems close to a proportional relationship, while this clearly is not the case in y-direction. This is probably due to the fact the normal stiffness is almost constant over the different friction coefficients, wherefore the x-direction mainly shows the influence of point 3 while the x-direction has both point 1 and 2. It is also clear the virtual play in x-direction is always bigger than in y-direction for the chosen dimensions.

For friction coefficients over $\mu = 0.32$ the model will not converge for all friction directions anymore, since the chuck will experience self-locking for certain positions (Appendix G). Therefore, the plot only shows values up to $\mu = 0.32$. To be able to test as much influence as possible, sliding coefficients of friction should also be maximum 0.32 (section 3.1).

2.2.3 Mathematical values initial positioning

Finally the initial displacements will be checked for the different alignment methods. The dimensions stay the same as for the virtual play model (Appendix E). Figure 9 shows the initial positioning. Specific values are given in Appendix H. Again rotations are not shown since they are small.

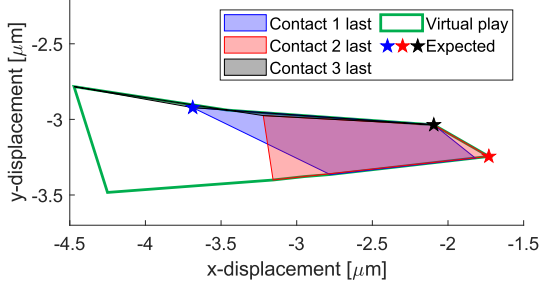


Figure 9: Displacements of the chuck centre depending on the different sequences of contact for $\mu = 0.2$ including the expected final locations

It is clear contact point 3 has a main deviation in x-direction. Points 1 and 2 also differ more in x- than y-direction. The uncertainty is smaller than the total virtual play, although the areas follow lots of the edges. Most of the final contact points would still slip and have been taken at their maximum friction. For higher friction coefficients, less points will slip, so the decrease in uncertainty would be even better (Appendix I).

3. Design of the test set-up

3.1 Design requirements

To be able to validate the model a test set-up will be build. Since the model resembles a two-dimensional coupling, it is important that the test set-up also resembles a two-dimensional world. Figure 10 shows the schematic overview of this test set-up, including the way the models fit into this.

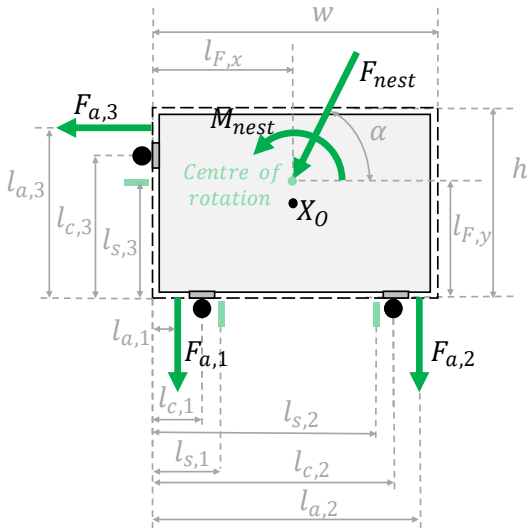


Figure 10: Schematic overview test set-up

This leads to the following requirements:

- [1] The chuck should be able to move restrictedly on a two-dimensional plane.

- [2] The set-up needs 3 points of contact to align the chuck within this controlled plane.
- [3] During the alignment of the chuck, the order of contact should be able to be controlled.
- [4] The nesting force acting on the chuck should be known.
- [5] The position of the chuck should be measured within hundreds of nanometres.
- [6] The sliding friction coefficients of the materials making contact should be in a range of $0 - 0.32$.
- [7] The test set-up should be able to conduct a minimum of 500 experiments.

These requirements are used for the concept generation (Appendix J).

3.2 Final design

Figure 11 shows the final design of the test set-up. The detailed development is explained in Appendices K till S. The bill of materials and assembly plan for this test set-up are given in Appendices T and U respectively.

An aluminium chuck of $154 \times 107 \text{mm}$ is restricted to a two-dimensional plane with a leaf spring mechanism in the middle of the chuck (I). The contact surfaces are interchangeable aluminium plates (II) of $25 \times 35 \times 2 \text{mm}$ which secured to the chuck with four bolts.

For low driving stiffness the leaf flexures are reinforced which gives an expected in-plane stiffness of 0.75N/mm with dimensions of $80 \times 35 \times 0.6 - 1.2 \text{mm}$. Requirement 1 for the test set-up is met.

The contact points are aligned to the two-dimensional plane by gluing steel balls (with $r = 5 \text{mm}$) to ball holders (III). The holders are connected to the bottom plate (IV). Requirement 2 is met. The sliding friction coefficient is determined as $\mu = 0.2$ (Appendix L). This is within the range of $0-0.32$ as stated in requirement 6.

The contact order is controlled with three separate force mechanisms (V), consisting out of linear stages connected with ropes and screw eyes to the chuck (VI). Loadcells (VII) are connected between the linear stage and ropes, with which the applied forces are measured, so requirement 3 and 4 are also met. Forces are applied such that the total nesting force leads to contacting forces of

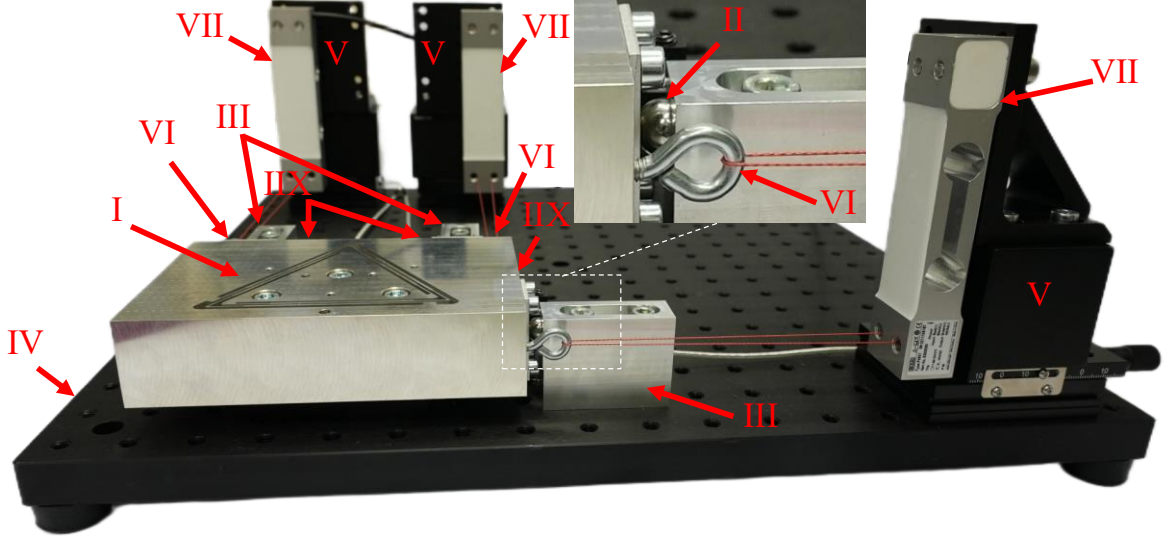


Figure 11: Final design test set-up

$F_{n,i} = 31.3N$. This leads to deformations of $3\mu m$ while the Von Mises stress is $577 - 594MPa$ for the balls and surfaces [24].

Requirement 5 stated the position of the chuck should be measured within hundreds of nanometres. This is done with capacitive sensors (IIX) which have a range of $500\mu m$.

The only requirement which is not met for certain till the experiments are carried out is requirement 7. It states a minimum of 500 experiments should be able to be conducted. Since the contact plates are interchangeable and the stresses of the leaf springs are not close to the yield stress, this is likely to be reachable.

4. The experiment

4.1 Method

Experiments are run to (A) validate the test set-up and (B) test the influence of different alignment sequences on the repeatability.

To validate the set-up, two experiments are executed. For experiment A1 multiple arbitrary but suitable sets forces are applied to the chuck to check the stability, noise and creep of the set-up. First, small forces are applied to reassure the chuck does not make contact with the base anywhere. This way stability, noise and creep are checked. After releasing, higher nesting forces are applied. These forces are used to check the influence of aforementioned effects on the determination of the final position while contact is made with the base. Results are shown in section 4.2.1

Experiment A2 should determine the contact stiffness for the test set-up. Contact is made at points 1 and 3 with relatively small forces after which $F_{a,2}$ is increased to find the corresponding displacement. The three sensor outputs are used to determine the displacements of the middle of the chuck as

$$\begin{bmatrix} dx \\ dy \\ d\theta \end{bmatrix} = \begin{bmatrix} 0 & 1 & \left(l_{s,1} - \frac{w}{2}\right) \\ 0 & 1 & \left(l_{s,2} - \frac{w}{2}\right) \\ 1 & 0 & \left(\frac{h}{2} - l_{s,3}\right) \end{bmatrix}^{-1} \left\{ \begin{bmatrix} y_{s,1} \\ y_{s,2} \\ x_{s,3} \end{bmatrix} + \epsilon \right\} \quad (15).$$

Here $y_{s,1}$, $y_{s,2}$ and $x_{s,3}$ are the measured distances between the sensors and the chuck. Before every test, when no forces are applied, the values are reset to 0 if necessary. The offset

$$\epsilon \text{ is determined to reassure } \begin{bmatrix} \delta_{n,1} \\ \delta_{n,2} \\ \delta_{n,3} \end{bmatrix} = 0 \text{ when}$$

contact is made (Appendix V).

The contact stiffness is determined based on $F_{a,2}$ and $\delta_{n,2}$. The difference between the applied force and actual contact force is not taken into account. The normal contact displacement is calculated based on (15) and (11). The contact stiffness results are given in section 4.2.2.

To test the influence of the alignment sequence on the repeatability again two experiments are executed. Different alignment sequences are tested for both experiments. The ropes are tightened sequentially to align the chuck in the

final position. The applied nesting forces are chosen to make the normal forces equal for the no-friction case (Appendix E). The displacements are converted to the middle of the chuck by (15).

The order of tests for both experiments differs. For experiment B1, every alignment sequence is repeated 5 times. For example sequence 123 means $F_{a,1}$ was applied till its final value for nesting was met, then $F_{a,2}$ was increased till its maximum and finally $F_{a,3}$. If the forces differ from their intended value when applying the final force, the same order is used for adjustments. After a sequence is repeated 5 times, the next sequence will be repeated 5 times till all sequences 123, 213, 132, 312, 231 and 321 are tested.

Experiment B2 is executed at a different day. This time only 3 different sequences are tested. First 123 is executed, then 312 and finally 231 after which the same order of three sequences is repeated till every sequence is repeated 5 times. The results are given in section 4.3.

4.2 Experiment A: Validation of the test set-up

4.2.1 Tightening effects

Figure 12 shows sequential tightening of $F_{a,1}$, $F_{a,2}$ and $F_{a,3}$. Small forces are applied which do not cause base contact.

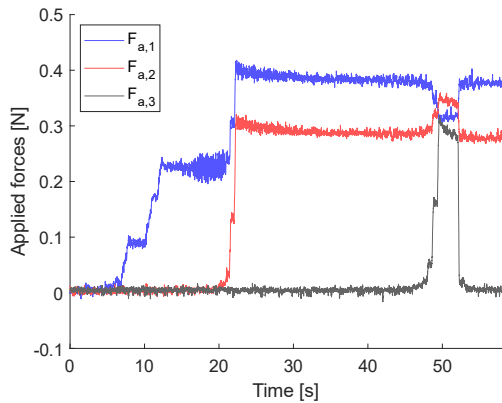


Figure 12: Tightening $F_{a,1}$, $F_{a,2}$ and $F_{a,3}$ sequentially

The figure shows there is crosstalk between different forces. When $F_{a,2}$ is actively increased ($t \approx 20$) $F_{a,1}$ increases as well. When $F_{a,3}$ is increased ($t \approx 50$) changes in both $F_{a,1}$ and $F_{a,2}$ are taking place. This can be explained by the

way the chuck is rotating around the middle of the triangle. When $F_{a,2}$ is increased while there is tension in ropes 1 or 3 this will lead to an increase in tension wherefore those forces are increased as well and vice versa. For the pair $F_{a,1}$ and $F_{a,3}$ an increase in either one leads to a decrease in the other force due to the release of rope tension.

The measured data is averaged to minimize the effects of noise. All force data is averaged over 50 measurements and all capacitive sensor data over 10 measurements. This was possible due to the noise being normally distributed (Appendix W).

Figure 13 shows sequential tightening of higher force to end up in the final nesting position.

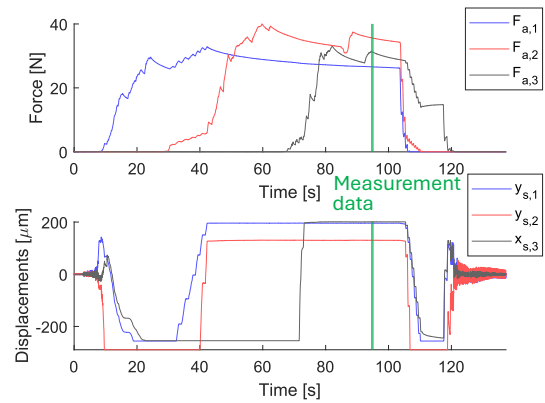


Figure 13: Forces and displacements alignment procedure, including location of measurement data

The figure shows peak forces decay over time. These peaks also show up in the displacements when contact is made (Figure 14).

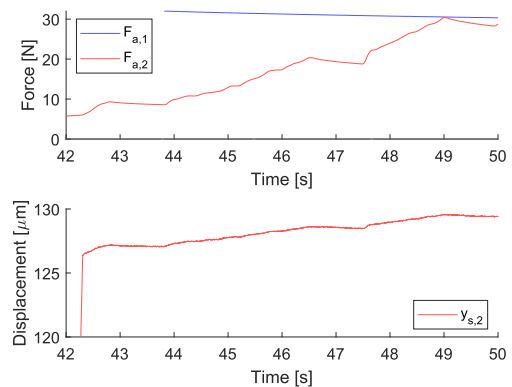


Figure 14: Zoom in forces and displacements alignment procedure of contact 2

After contact is made, the displacement of sensor 2 seem to follow the applied force. Both are not measured exactly at the contact. Creep in the wires is suspected to be the main contributor to the decay. It is not induced by the electronics since the output was not decaying during the calibration of the loadcells (Appendix R).

To deal with the decay we take the datapoint where all forces are closest to the ideal value (Figure 13) to calculate the final displacement with (15) for experiments B. If one of the forces is more than 1N off, the data will not be taken into account to make sure the distribution of forces does not influence the distribution of displacements too much.

4.2.2 Determining stiffnesses

Figure 15 shows the force-displacement plot of the contact stiffness test.

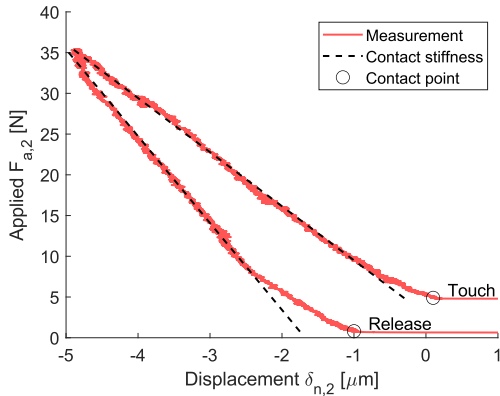


Figure 15: Determining contact stiffness of contact 2 after contact 1 and 3 are aligned

The figure shows the stiffness increases when contact is made. The total contact stiffness is in the range $6.6 - 10.7 N/\mu m$, which matches the expected $10.0 N/\mu m$ of the model (Appendix C). The flexure stiffness is determined as $0.85 \cdot 10^{-3} N/\mu m$ (Appendix X) and will be neglected.

Hysteresis is observed when releasing the contact. This leads to the possible range of contact stiffness and results in extra uncertainties. The hysteresis might be attributed to sliding at the contacts. The actual contact force cannot be determined and will be influenced by all forces. The force $F_{a,2}$ should have the main influence, since it is closest to the contact and larger than the other forces. The

measurement of sensor 2 does seem to follow this force (Figure 16).

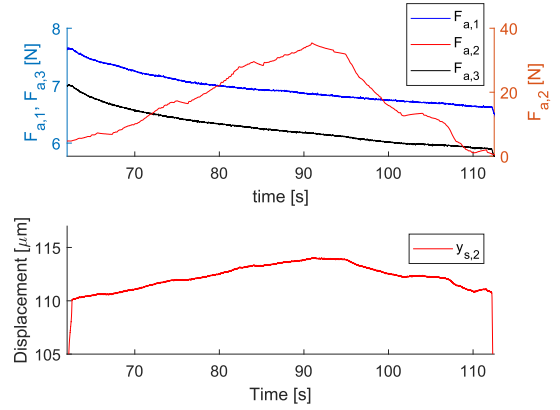


Figure 16: Forces and measured distance stiffness test

The figure shows $F_{a,1}$ and $F_{a,3}$ decay over time, which is unfavourable since all forces will have influence on the actual contact force. This is happening due to creep during the measurement. No crosstalk is showing up, since points do not move much after contact is made.

4.3 Experiment B: Repeatability results

Figures 17 and 18 show the final displacements after loading the chuck with different sequences of contact. For comparison with the theoretical model we included the shape of virtual play in the figures.

The figures show final positions are in the same order of expected virtual play as the model. The displacement variations for B1 is $s_{v,x} = 3.26 \mu m$ and $s_{v,y} = 1.76 \mu m$ and for B2 $s_{v,x} = 6.39 \mu m$ and $s_{v,y} = 2.55 \mu m$. The displacement of the test results does not fit entirely within the expected region. Calibration offsets and wear might play a role. During alignment small particles are left behind on the balls and surfaces, which are not cleaned in between.

The average x-displacements of the sequences where contact 1 was last is larger than the x-displacements when contact 2 or 3 were last. This matches the expectations of the alignment model.

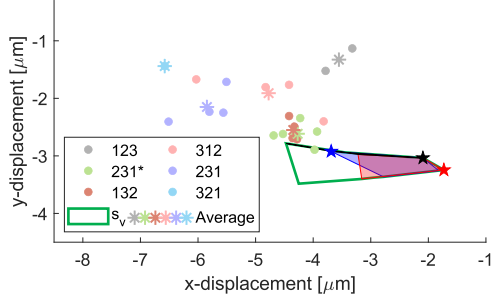


Figure 17: Experiment B1: Final (average) positions of the chuck for different alignment sequences

Sequence 231* was supposed to be 213, but during alignment contact 3 was touching the base before contact 1

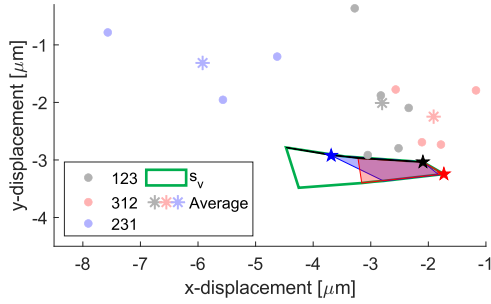


Figure 18: Experiment B2: Final (average) positions of the chuck for different alignment sequences

The standard deviations per sequence of the experiments and in total are calculated (Appendix Y). Table 1 shows the average and total standard deviations.

Table 1: Standard deviations of the experiment results

Spread	Value B1 [μm]	Value B2 [μm]
Average σ_x	0.42	0.82
Average σ_y	0.26	0.72
Total σ_x	0.94	1.80
Total σ_y	0.50	0.82

The table shows the spread of experiment B1 is seemingly smaller than of experiment B2, which means the repeatability is better. This might be contributed to the wear that occurs when contact is made.

In both cases using one alignment sequence leads to a better repeatability than taking all alignment sequences together. For experiment B1 this goes down to $\sigma_x = 0.06\mu\text{m}$ and $\sigma_y = 0.18\mu\text{m}$ with displacement variations of

$s_{v,x} = 0.14\mu\text{m}$ and $s_{v,y} = 0.40\mu\text{m}$ when choosing sequence 132. For experiment B2 this goes to $\sigma_x = 0.59\mu\text{m}$ and $\sigma_y = 0.54\mu\text{m}$ with $s_{v,x} = 1.39\mu\text{m}$ and $s_{v,y} = 0.96\mu\text{m}$ when choosing sequence 312.

5. Discussion

The test set-up lead to the same order of virtual play as the model. The values do not fit exactly within the expected region. Hysteresis showed up in making contact with one point, which was not accounted for in the model. This contributes to the result that one alignment sequence does still have uncertainty. Applied forces might differ up to $1N$ from their intended values, although this will lead to a maximum offset of $0.15\mu\text{m}$ with the determined stiffness.

The friction direction is not entirely certain, since forces also decrease while testing due to the influence they have on each other and the creep which shows up in the system. The location of the x-displacements does suggest the friction directions correspond to the expected directions of the alignment model. Even with the uncertainties, using one alignment sequence suggests improved repeatability. This is a new research direction to improve the alignment of kinematic couplings.

To minimize the spread in final position, we propose to redo the experiment in an isolated chamber to eliminate environmental disturbances even further. Although a box did not improve noise significantly (Appendix W), this has not been tested for a long time. It is likely that isolation does help improve influence of noise during the tests. It is important to look in more detail to the noise due to thermal effects when isolating the set-up.

The next step is expanding this research by executing more tests. Different materials should be used to further validate and improve the model. The oxidation layer of aluminium makes it unpredictable what material is making contact. Using a different surface material might bring the test results closer to the models. A tribology point of view could be integrated to better understand how the surface finish of test objects influences the friction. It could be

interesting to incorporate lubricated surfaces as well using the Stribeck effect.

When running more simulations for validations, it is useful to update the force applications with actuators to easily generate lots of results. The ropes should be changed as well to limit the effects of creep.

The worst case theory is currently used to stay within configurations where self-locking does not happen. This could be implemented even more by checking if the alignment sequence can prevent self-locking to occur. In the current case friction coefficients slightly larger than 0.32 might lock the chuck at contact points 1 and 3. If either of these points is making contact last, higher friction coefficients might be used.

Building on this research a three-dimensional model could be developed. Appendix D could be taken as a starting point for expanding the models. A new test set-up should be built to validate those models. Weighert et al. [25] provide a way to accurately test a three-dimensional model, so their research could be incorporated in this test set-up.

Using the three-dimensional model general guidelines for alignment procedures could be developed to implement the advantages for different kinematic couplings. It might be possible to have an influence on the alignment approach by using different materials within one chuck to force slip on specific contact points. This could be taken as a new topic of research.

In the introduction it was stated how the research field excludes certain design factors. The field of kinematic couplings itself is relatively small. It is debatable to what extent couplings which are partly based on manipulation and partly just on static contact points are still to be called kinematic couplings. A more closely look into partially active manipulation might improve the alignment procedures as well.

6. Conclusion

In this thesis an analytical model was presented to describe the virtual play of a two-dimensional kinematic coupling based on friction and compliance. An alignment model was developed to investigate the influence of an alignment sequence. The models are validated with a test set-up.

In the current situation a nesting force of 70N lead to a virtual play in the model of $s_{v,x} = 2.74\mu m$ and $s_{v,y} = 0.70\mu m$. The displacement variations of the experiments let to $s_{v,x} = 6.39\mu m$ and $s_{v,y} = 2.55\mu m$. The results did not match the expected displacements entirely. Hysteresis showed up in the contact points due to slip. This lead to stiffness variations, causing calibration errors, wherefor using one alignment sequence still had uncertainty.

Using a specific alignment sequence did reduce the variations. When repeating contact sequence 132 and the variations could go down to $s_{v,x} = 0.14\mu m$ and $s_{v,y} = 0.40\mu m$. If uncertainties while testing will be controlled better, this improvement might be even more.

The test set-up should also be useful within future research to validate expanded virtual play models. By expanding the presented research to the three-dimensional world, the repeatability of kinematic couplings could be improved.

Literature

- [1] Gao, Y., Cui, Y., Li, H., Gong, L., Lin, Q., Liu, D., & Lin, Z. (2018). Alignment system for SGII-Up laser facility. *Optics & Laser Technology*, 100, 87-96.
- [2] Slocum, A.H. (2010). Kinematic couplings: A review of design principles and applications. *International journal of machine tools and manufacture*, 50(4), 310-327.
- [3] Seubers, H.A. (2020). *Micro kinematic coupling using deep reactive-ion etched surfaces in silicon photonic integrated circuits*, (Master's thesis). University of Twente.
- [4] Slocum, A.H. (1992). Design of three-groove kinematic couplings. *Precision Engineering*, 14(2), 67-76.
- [5] Hale, L.C., & Slocum, A.H. (2001). Optimal design techniques for kinematic couplings. *Precision Engineering*, 25(2), 114-127.
- [6] Weigert, F., Wolf, M., & Theska, R. (2022). *Model-based determination of the reproducibility of kinematic couplings*, Proceedings of the 22nd International Conference of the European Society for Precision Engineering and Nanotechnology, 87-90.
- [7] Hart, A.J., Slocum, A.H., & Willoughby, P. (2004). Kinematic coupling interchangeability. *Precision Engineering*, 28(1), 1-15.
- [8] Mangudi, K.V., & Culpepper, M.L. (2004). *Active compliant fixtures for nanomanufacturing*. Annual meeting of ASPE.
- [9] Veugelers, M. (2019). *The effect of deformations on the self-alignment of kinematic couplings*, (Master's thesis). University of Twente & VDL Enabling Technologies Group.
- [10] Hale, L.C. (1998). *Friction-Based Design of Kinematic Couplings*, American Society for Precision Engineering 13th Annual Meeting St. Louis, Missouri.
- [11] Hale, L.C. (2020). Testing the limiting coefficient of friction with an adjustable 3-V kinematic coupling. *Precision Engineering*, 64, 200-209.
- [12] Patti, F., & Vogels, J.M. (2019). Self-alignment of kinematic couplings: Effects of deformations. *Precision Engineering*, 60, 348-354.
- [13] Neulen, D.J. (2020). *Design of a Test Setup to Simulate the Effects of Deformations within Kinematic Couplings*, (Master's thesis). University of Twente & VDL Enabling Technologies Group.
- [14] Soemers, H. (2017). *Design Principles for precision mechanisms*. Enschede, the Netherlands: T-Pointprint.
- [15] Schouten, C.H., Rosielle, P.C.J.N., & Schellekens, P.H.J. (1997). Design of a kinematic coupling for precision applications. *Precision Engineering*, 20(1), 46-52.
- [16] Culpepper, M. L. (2000). *Design and application of compliant quasi-kinematic couplings*, (Doctoral dissertation). Massachusetts Institute of Technology.
- [17] Culpepper, M.L. (2004). Design of quasi-kinematic couplings. *Precision Engineering*, 28(3), 338-357.
- [18] Ziegert, J., & Tymianski, V. (2007). Air bearing kinematic couplings. *Precision engineering*, 31(2), 73-82.
- [19] De Benedictis, C., & Ferraresi, C. (2023). Precise positioning in a robotized laser-cutting machine allowed by a three-V-shaped-groove kinematic coupling: a feasibility study. *Robotica*, 41(9), 2703-2712.
- [20] Ye, Y., Chen, L., Yang, L., Dong, J., Xu, S., & Wang, S. (2020). Precision of kinematic coupling mechanism for optical instruments. *Optik*, 202, 163592.
- [21] Fan, Z., Yang, K., Yuan, B., Mu, X., Yin, K., Sun, Q., & Sun, W. (2024). Analysis and Optimization of Repetitive Positioning Precision for Kinematic Couplings of Opto-Mechanical Components Considering Uncertainty. *Precision Engineering*.
- [22] Johnson, K.L. (1985). *Contact Mechanics*, Cambridge University Press.

- [23] Greenwood, J. (1985). Analysis of Elliptical Hertzian Contacts. *Tribology International* 30(1997), 235-237.
- [24] Hertzwin (2023).
- [25] Weigert, F., Hebenstreit, R., Füßl, R., & Theska, R. (2021). Experimental setup for the investigation of reproducibility of novel tool changing systems in nanofabrication machines. *Nanomanufacturing and Metrology*, 4(3), 181-189.
- [26] Ansys Granta Edupack (2021) R1
- [27] Su, Hai-Jun & Shi, Hongliang & Yu, Jingjun. (2011). *Figure 10 – (a) a compliant platform*, [Image]. Proceedings of the ASME Design Engineering Technical Conference. 6. 10.1115/DETC2011-48013.
- [28] STAS (2024). *STAS aircraft cable suspension set with external M10 cable grip and ceiling mount*, [Image]. <https://www.picturehangingsystems.com/stas-suspension-set-external-m10-cable-grip> [Accessed 28 April 2025].
- [29] Al-Jodah, A., Shirinzadeh, B., Ghafarian, M., Das, T. K., & Pinskiar, J. (2021). Design, modeling, and control of a large range 3-DOF micropositioning stage. *Mechanism and Machine Theory*, 156, 104159.
- [30] Oavco (2025). *OAVR080R*, [Image]. <https://www.oavco.com/ko/oavr080r> [Accessed 28 April 2025].
- [31] Power Transmission Engineering (2025). *Moving coil*, [Image]. <https://www.powertransmission.com/what-is-a-voice-coil-actuator> [Accessed 28 April 2025].
- [32] Physik Instrumente (2025). *Piezo Actuator Products Overview*, [Image]. <https://www.pi-usa.us/en/products/piezo-actuators-stacks-benders-tubes/piezo-actuator-overview> [Accessed 28 April 2025].
- [33] Hydraulic Actuator Manufacturers Suppliers (n.d.). *Linear actuators*, [Image]. <https://hydrauliccylindermanufacturers.net/hydraulic-actuators/> [Accessed 28 April 2025].
- [34] Slocum, A.H., Bow, N.H., Braunstein, D., & Somerville, M. (1996). *US Patent 5,915,678*. [Image].
- [35] Chengdu Jingbang Technology Co (2025). [Image]. Ltd <https://dutch.alibaba.com/product-detail/8Mm-Ball-Screw-Spindle-8Ft-700Mm-1600184583483.html> [Accessed 28 April 2025].
- [36] MPositioning (2025). *XY Linear Stage, MPositioning T125XY-50R Precision Manual XY Translation Stage 50 mm Travel in 2-Axis 125 x 125 mm Platform Table*, [Image]. <https://www.ubuy.co.nl/en/product/3MOA3XFQW-xy-linear-stage-mpositioning-t125xy-50r-precision-manual-xy-translation-stage-50-mm-travel-in-2-axis-125-x-125-mm-platform-table?ref=hm-google-redirect> [Accessed 28 April 2025].
- [37] Omegon (2025). *Capture CCD-camera (zwart/wit) 618*, [Image]. <https://www.omegon.eu/nl/astro-camera-s/omegon-capture-ccd-camera-zwart-wit-618/p,44985> [Accessed 28 April 2025].
- [38] Eilersen (2025). *Compression Load Cell DMC (DMC-Ex) 125*, [Image]. <https://eilersen.com/digital-load-cells/product/compression-load-cell-dmc-ex-125> [Accessed 28 April 2025].
- [39] Distrelec Schweiz AG. (2025). *O200.SP-GWIJ.72NV - Optical Sensor Push-Pull 180mm 250us 30VDC 50mA IP67 O200*, [Image]. <https://www.distrelec.nl/en/optical-sensor-push-pull-180mm-250us-30vdc-50ma-ip67-o200-baumer-electric-o200-sp-gw1j-72nv/p/30158278> [Accessed 28 April 2025].
- [40] Locon (2025). *Capacitive analog*, [Image]. <https://www.locon.net/capacitive/analog/> [Accessed 28 April 2025].
- [41] Kappelhof, J. P., & Nijenhuis, J. R. (2003). Statically determined structures: tension between classical and modern design--an engineering approach. *Optomechanics*, 5176, 114-125. SPIE.

[42] Janssen Precision Engineering (2023). *Leaf spring/flexure: Reinforced Construction Design & Examples*. <https://www.jpe-innovations.com/precision-point/leaf-spring-flexure-reinforced/>

[43] Iron Boar Labs Ltd. (2020). *6082-T6 Aluminum*. <https://www.makeitfrom.com/material-properties/6082-T6-Aluminum> [Accessed 31 March 2025].

[44] Studman, C.J., & Field, J.E. (1973). A simple method for measuring friction for spheres and cylinders. *Wear*, 24, 243-246.

Appendices

Appendix A: Ideal model

Figure 19 shows in the ideal case, no friction is present.

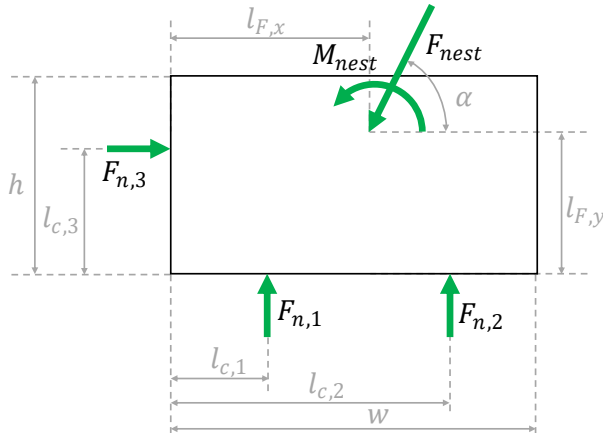


Figure 19: Ideal frictionless nesting situation

This leads to the equilibrium equations

$$\Sigma F_x = F_{n,3} - \cos(\alpha)F_{nest} = 0$$

$$\Sigma F_y = F_{n,1} + F_{n,2} - \sin(\alpha)F_{nest} = 0$$

(16).

$$\Sigma M = l_{c,1} \cdot F_{n,1} + l_{c,2} \cdot F_{n,2} - l_{c,3} \cdot F_{n,3} + \cos(\alpha)F_{nest} \cdot l_{F,y} - \sin(\alpha)F_{nest} \cdot l_{F,x} + M_{nest} = 0$$

The forces are calculated for the dimensions of the test set-up (Appendix E). The corresponding displacements and slip are calculated with (4) and (11). This leads to Table 2.

Table 2: Results ideal model

Parameter	Unit	Value
$F_{n,1}$	N	31.3092
$F_{n,2}$	N	31.3007
$F_{n,3}$	N	31.3050
dy_1	μm	-3.1867
dy_2	μm	-3.1861
dx_3	μm	-3.1864
dx	μm	-3.1863
dy	μm	-3.1864
θ	nrad	5.7777
$dx_{slip,1}$	μm	3.1859
$dx_{slip,2}$	μm	3.1859
$dy_{slip,3}$	μm	3.1869

Appendix B: Non-linear model

When the model is not linearised, the equilibrium equations expand

$$\begin{aligned}\Sigma F_x &= F_{n,3} - \cos(\alpha)F_{nest} + F_{t,1} + F_{t,2} = 0 \\ \Sigma F_y &= F_{n,1} + F_{n,2} - \sin(\alpha)F_{nest} + F_{t,3} = 0\end{aligned}\tag{17}.$$

$$\Sigma M = (l_{c,1} + dx_1)F_{n,1} + (l_{c,2} + dx_2)F_{n,2} - (l_{c,3} + dy_3)F_{n,3} + \cos(\alpha) F_{nest} \left(l_{F,y} + dy + d\theta \left(l_{F,x} - \frac{w}{2} \right) \right) - \sin(\alpha) F_{nest} \left(l_{F,x} + dx + d\theta \left(\frac{h}{2} - l_{F,y} \right) \right) + M_{nest} - dy_1 \cdot F_{t,1} - dy_2 \cdot F_{t,2} + dx_3 \cdot F_{t,3} = 0$$

Figure 3 is still leading for the dimensions. The virtual play should numerically be updated according to the virtual play found with the linear model. Afterwards, the procedure should be rerun till satisfactory results are obtained.

Appendix C: Deformation model

C.1 Mathematical equations

When only taken into account the deformations which play a role, the chuck can be modelled in a nest of springs. Although the virtual play will not show up in this model, it is nice to use the deformations to make assumptions about the forces which are playing a role.

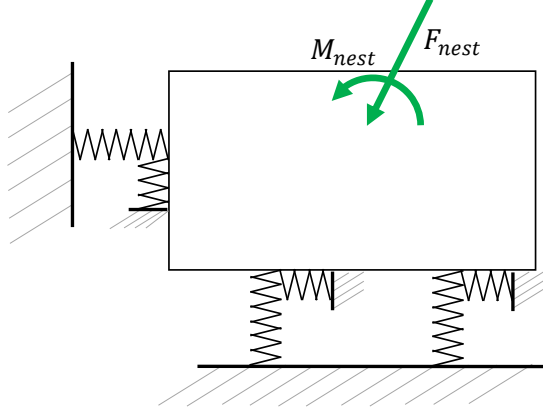


Figure 20: Deformation model as a nest of springs

The deformations show the compliance of the model in the contacts with spring constants. To describe these deformations and find these spring constants the Hertzian contact model will be used. The normal forces of (2) will be calculated with

$$F_{ni} = -dX_{n,i} \cdot k_{n,i} \quad \forall i \in \{1,2,3\} \quad (18).$$

Here $X_n = [y_1 \ y_2 \ x_3]$ and $k_{n,i}$ is calculated with the secant stiffness of (4) as

$$k_{n,i} = \left(\frac{16 \cdot r \cdot E^* \cdot F_{n,i}}{9} \right)^{1/3} \quad (19).$$

The stiffness of the ball contacts is assumed linear around a certain contact force. The ideal model of Appendix A shows an estimation of the reaction forces. A numerical solver will be used to update the stiffness to model this non-linear behaviour and reduce computational time.

The tangential forces in this model are given by

$$F_{ti} = -dX_{t,i} \cdot k_{t,i} \quad \forall i \in \{1,2,3\} \quad (20).$$

where $X_t = [x_1 \ x_2 \ y_3]$. The stiffness $k_{t,i}$ is calculated with (7) as

$$k_{t,i} = \left(\frac{384 \cdot r \cdot F_{n,i}}{E^*} \right)^{1/3} \left(\frac{2-\nu_b}{G_b} + \frac{2-\nu_s}{G_s} \right)^{-1} \quad (21).$$

which is based on the Hertzian contact model without slip, in contrast to the virtual play model. The tangential stiffnesses of the ball contacts will also be updated using a numerical solver.

The system will be solved in a different way than before, since the tangential and normal forces are currently not linked. This is done by expressing all displacements in the centre of the chuck with (11). This time all slip should be taken as 0. Displacements due to the original contact of the chuck are not taken into account, since these will only matter if the chuck will display significant rotations.

C.2 Numerical values

The model is simulated with Matlab to find the displacement of a rectangular chuck. The dimensions of the chuck are given in Appendix E.

It is found the normal forces all have a value of $F_{n,i} \approx 33.3N$ in the ideal case (Appendix A). Calculating the corresponding secant stiffness for steel balls on a steel surface with (19) leads to $k_n = 10.0 \cdot 10^3 N/mm$. This stiffness will be used in the deformation model. The original tangential stiffness is calculated with (21) which gives $k_t = 12.2 \cdot 10^3 N/mm$.

The model will keep rerunning to update the stiffnesses until all stiffnesses have an accuracy within $0.1 \cdot 10^3 N/mm$. The deformation model leads to Figure 21 with Table 3 showing displacements. The displacements are upscaled with a factor 1000 for clear visualisation.

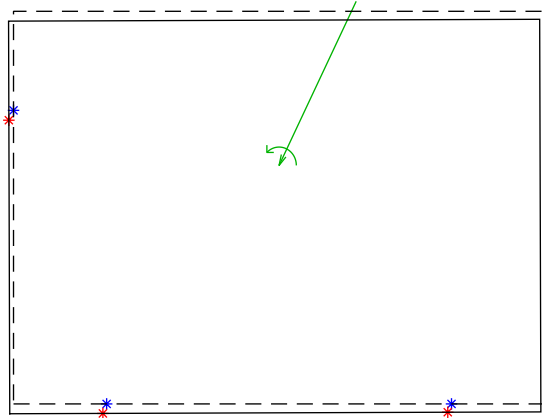


Figure 21: Movements deformation model with a displacement scaling factor 1000

Table 3: Displacements deformation model

Displacement	Unit	Value
dx_1	μm	-1.0886
dy_1	μm	-2.5920
dx_2	μm	-1.0886
dy_2	μm	-2.2670
dx_3	μm	-1.3486
dy_3	μm	-2.6797
dx	μm	-1.2624
dy	μm	-2.4295
$d\theta$	μrad	3.2499

In Table 4 the forces and final stiffness coefficients are added for the sake of completeness.

Table 4: Results deformation model

Parameter	Unit	Value
$F_{n,1}$	N	22.6514
$F_{n,2}$	N	18.9144
$F_{n,3}$	N	8.7197
$F_{t,1}$	N	11.5542
$F_{t,2}$	N	11.0311
$F_{t,3}$	N	21.0441
$k_{n,1}$	$N/\mu m$	8.7391
$k_{n,2}$	$N/\mu m$	8.3435
$k_{n,3}$	$N/\mu m$	6.4659
$k_{t,1}$	$N/\mu m$	10.6141
$k_{t,2}$	$N/\mu m$	10.1336
$k_{t,3}$	$N/\mu m$	7.8532

It is good to note the assumption of no slip does not apply depending on the maximum allowed friction coefficients, so this model cannot be used for all cases.

Appendix D: Three-dimensional expansion

In the three-dimensional world the equilibrium equations will expand. There will be 6 equilibrium equations and 6 contact points. Contacting points and forces should become three dimensional vectors

$$X_i = [x_i \ y_i \ z_i] \ \forall i \in \{1,2,3,4,5,6\}$$

$$\vec{F}_{n,i} = [F_{x,i} \ F_{y,i} \ F_{z,i}] \ \forall i \in \{1,2,3,4,5,6\} \quad (22).$$

$$\vec{F}_{t,i} = [F_{x,i} \ F_{y,i} \ F_{z,i}] \ \forall i \in \{1,2,3,4,5,6\}$$

Tangential forces are perpendicular to the normal forces which leads to

$$\vec{F}_{n,i} \cdot \vec{F}_{t,i} = 0 \ \forall i \in \{1,2,3,4,5,6\} \quad (23).$$

The nesting force and moment are also three-dimensional

$$\vec{F}_{nest} = [F_x \ F_y \ F_z]$$

$$\vec{M}_{nest} = [M_x \ M_y \ M_z] \quad (24).$$

$$X_{nest} = [x_{nest} \ y_{nest} \ z_{nest}]$$

The equilibrium equations become

$$\Sigma F = \vec{F}_{n,i} + \vec{F}_{t,i} + \vec{F}_{nest} = 0 \ \forall i \in \{1,2,3,4,5,6\} \quad (25).$$

$$\Sigma M = X_i \times (\vec{F}_{n,i} + \vec{F}_{t,i}) + X_{nest} \times \vec{F}_{nest} + \vec{M}_{nest} = 0 \ \forall i \in \{1,2,3,4,5,6\}$$

In the friction model, the friction forces will also lead to the same values as before

$$|F_{t,i}| = \mu_i \cdot |F_{n,i}| \ \forall i \in \{1,2,3,4,5,6\} \quad (26).$$

However, to acquire the virtual play, they will not be maximum in just 2 directions, but each force can be spanned over the entire tangential circle at the contact point. Figure 22 shows the circle where γ represents the angle of the tangential force in the plane normal to the contact. To span the entire circle $0 \leq \gamma < 2\pi$.

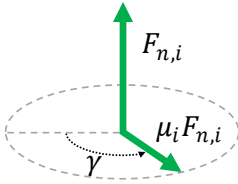


Figure 22: Friction force spanning around normal force

The deformations should still be calculated model using the Hertzian contact model in the same way as for the two-dimensional model. The model for calculating the virtual play should be updated accordingly to the three-dimensional geometry.

Appendix E: Dimensions material properties

E.1 Model properties

The dimensions of the chuck are given in Table 5. The values for M_{nest} and α are chosen in such a way all reaction forces are approximately equal in the ideal frictionless case. The material properties of the contacts are given in Table 6.

Table 5: Dimensions model calculations

Dimension	Unit	Value
$l_{c,1}$	mm	27
$l_{c,2}$	mm	127
$l_{c,3}$	mm	80
$l_{F,x}$	mm	77
$l_{F,y}$	mm	65
h	mm	107
w	mm	154
α	rad	$\tan^{-1}(2)$
F_{nest}	N	70
M_{nest}	Nmm	470

Table 6: Properties ball contact [26]

Property	Unit	Value
E_{steel}	GPa	200
ν_{steel}	—	0.29
$E_{aluminium}$	GPa	71
$\nu_{aluminium}$	—	0.33
r	mm	5
μ	—	0.2

E.2 Values test set-up

Additionally to the model, some other dimensions are playing a role for the test set-up. Table 7 shows the additional values. The forces are chosen in such a way they match the nesting forces of the model (Table 5). This way, the set-up can be used for verification of the model.

Table 7: Dimensions model calculations corresponding Figure 10

Dimension	Unit	Value
$l_{a,1}$	mm	9.5
$l_{a,2}$	mm	144.5
$l_{a,3}$	mm	97.5
$F_{a,1}$	N	27.3
$F_{a,2}$	N	35.4
$F_{a,3}$	N	31.3
$l_{s,1}$	mm	50
$l_{s,2}$	mm	109
$l_{s,3}$	mm	60

Appendix F: Values virtual play model

The mathematical values for the displacements based on different friction coefficients are given in Table 8.

Table 8: Results virtual play model

Parameter	Unit	Values			
μ_1	–	0.2	0.2	0.2	0.2
μ_2	–	0.2	0.2	–0.2	–0.2
μ_3	–	0.2	–0.2	0.2	–0.2
$F_{n,1}$	N	35.7310	46.4921	20.0739	40.6817
$F_{n,2}$	N	22.9658	19.7299	35.6519	27.6687
$F_{n,3}$	N	19.5656	18.0605	34.4205	28.7024
$F_{t,1}$	N	7.1462	9.2984	4.0148	8.1363
$F_{t,2}$	N	4.5932	3.9460	–7.1304	–5.5337
$F_{t,3}$	N	3.9131	–3.6121	6.8841	–5.7405
dx_1	μm	–0.8596	–1.0245	–0.5853	–0.9373
dy_1	μm	–3.4801	–4.1477	–2.3694	–3.7945
dx_2	μm	–0.6402	–0.5786	0.8583	0.7249
dy_2	μm	–2.5919	–2.3423	–3.4749	–2.9346
dx_3	μm	–2.3293	–2.2082	–3.3945	–3.0073
dy_3	μm	–0.5753	0.5454	–0.8385	0.7428
dx	μm	–2.0939	–1.7298	–3.6874	–2.7794
dy	μm	–3.0360	–3.2450	–2.9222	–3.3646
$d\theta$	μrad	8.8821	18.054	–11.055	8.5992
$dx_{slip,1}$	μm	0.7591	–0.2606	3.6936	1.3821
$dx_{slip,2}$	μm	0.9785	0.1853	5.1372	3.0442
$dy_{slip,3}$	μm	3.1446	5.1807	1.2325	4.7695
μ_1	–	–0.2	–0.2	–0.2	–0.2
μ_2	–	0.2	0.2	–0.2	–0.2
μ_3	–	0.2	–0.2	0.2	–0.2
$F_{n,1}$	N	24.8276	38.4232	11.9363	31.4266
$F_{n,2}$	N	31.8002	30.7544	42.2454	40.3139
$F_{n,3}$	N	29.9104	32.8387	42.1413	45.6531
$F_{t,1}$	N	–4.9655	–7.6846	–2.3873	–6.2853
$F_{t,2}$	N	6.3600	6.1509	–8.4491	–8.0628
$F_{t,3}$	N	5.9821	–6.5677	8.4283	–9.1306
dx_1	μm	0.6744	0.9023	0.4139	0.7891
dy_1	μm	–2.7301	–3.6528	–1.6755	–3.1947
dx_2	μm	–0.7953	–0.7778	0.9611	0.9316
dy_2	μm	–3.2199	–3.1489	–3.8912	–3.7716
dx_3	μm	–3.0911	–3.2897	–3.8848	–4.0977
dy_3	μm	–0.7635	0.8126	–0.9596	1.0122
dx	μm	–3.2209	–3.1561	–4.4719	–4.2506
dy	μm	–2.9750	–3.4009	–2.7833	–3.4831
$d\theta$	μrad	–4.8980	5.0383	–22.157	–5.7697
$dx_{slip,1}$	μm	4.1573	3.7888	6.0712	5.3484
$dx_{slip,2}$	μm	2.6876	2.1088	6.6184	5.4909
$dy_{slip,3}$	μm	1.8344	4.6014	0.1177	4.0510

Appendix G: Maximum friction coefficient for no self-locking

A graphical method based on friction cones will be used to determine the limiting friction coefficient for no self-locking with the worst-case theory [9]. The friction cones are shown in Figure 23.

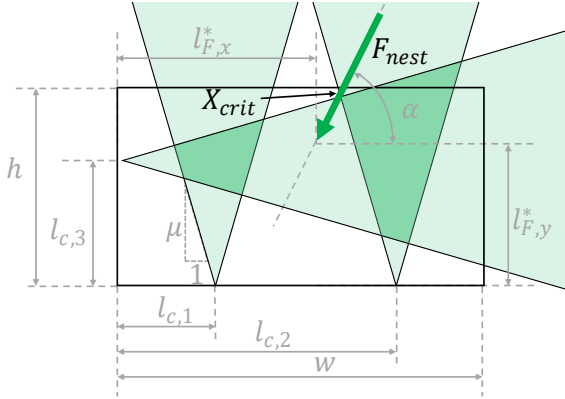


Figure 23: Limiting friction coefficient for self-locking of contact 2 and 3

When the line of action of the nesting force goes through two overlapping friction cones, the chuck might experience self-locking. The nesting moment is used in this model to shift the location of the applied nesting force as

$$l_{F,x}^* = l_{F,x} - \sin(\alpha) \frac{M_{nest}}{F_{nest}} \quad (27).$$

$$l_{F,y}^* = l_{F,y} + \cos(\alpha) \frac{M_{nest}}{F_{nest}}$$

The friction coefficient is limited, if the nesting force goes through the point where the edges of two friction cones cross. For the used dimensions (Appendix E), this is limited by point 2 and 3. The edge

$$\text{of point 2 is given by } \overrightarrow{X_{fric,2}} = \begin{pmatrix} l_{c,2} \\ 0 \end{pmatrix} + \lambda_{fric,2} \begin{pmatrix} -\mu \\ 1 \end{pmatrix} \quad (28).$$

$$\text{and point 3 by } \overrightarrow{X_{fric,3}} = \begin{pmatrix} 0 \\ l_{c,3} \end{pmatrix} + \lambda_{fric,3} \begin{pmatrix} 1 \\ \mu \end{pmatrix} \quad (29).$$

$$\text{The line of action of the nesting force is given by } \overrightarrow{X_{nest}} = \begin{pmatrix} l_{F,x}^* \\ l_{F,y}^* \end{pmatrix} + \lambda_{nest} \begin{pmatrix} \cos(\alpha) \\ \sin(\alpha) \end{pmatrix} \quad (30).$$

Combining (28), (29) and (30) as $X_{crit} = \overrightarrow{X_{fric,2}} = \overrightarrow{X_{fric,3}} = \overrightarrow{X_{nest}}$ leads to the friction coefficient of this model as $\mu_{max} = 0.32$. Different geometry might lead to different points determining the limiting position.

Appendix H: Values alignment model

Table 9 shows the values for different alignment sequences based on the model where the final point making contact should not be slipping.

Table 9: Results alignment model based on deformation final contact

Parameter	Unit	Point 1 deforming			
μ_2	–	0.2	0.2	–0.2	–0.2
μ_3	–	0.2	–0.2	0.2	–0.2
$F_{n,1}$	N	38.1651	45.9063	34.3730	43.8471
$F_{n,2}$	N	20.9935	20.5302	24.0661	23.3437
$F_{n,3}$	N	17.2562	19.1334	20.8541	22.9048
$F_{t,1}$	N	9.8501	8.0655	15.2641	13.0689
$F_{t,2}$	N	4.1987	4.1060	–4.8132	–4.6687
$F_{t,3}$	N	3.4512	–3.8267	4.1708	–4.5810
dx_1	μm	–1.1619	–0.8941	–1.8594	–1.4702
dy_1	μm	–3.6450	–4.1204	–3.3903	–3.9940
dx_2	μm	–0.6009	–0.5908	0.6607	0.6451
dy_2	μm	–2.4328	–2.3920	–2.6750	–2.6118
dx_3	μm	–2.1316	–2.2768	–2.4316	–2.5759
dy_3	μm	–0.5265	0.5624	–0.6006	0.6363
dx	μm	–1.8104	–1.8187	–2.2421	–2.2097
dy	μm	–3.0389	–3.2562	–3.0326	–3.3029
$d\theta$	μrad	12.122	17.284	7.1531	13.822
$dx_{slip,2}$	μm	0.5609	0.3032	2.5201	2.1153
$dy_{slip,3}$	μm	3.4458	5.1494	2.9828	5.0034
μ_1	–	0.2581	0.1757	0.4441	0.2981
		Point 2 deforming			
μ_1	–	0.2	0.2	–0.2	–0.2
μ_3	–	0.2	–0.2	0.2	–0.2
$F_{n,1}$	N	38.9850	46.7791	32.9272	42.3398
$F_{n,2}$	N	20.3292	19.3378	25.2376	25.4032
$F_{n,3}$	N	16.4783	17.5349	22.2258	25.6655
$F_{t,1}$	N	7.7970	9.3558	–6.5854	–8.4680
$F_{t,2}$	N	7.0296	4.4142	15.6646	14.1074
$F_{t,3}$	N	3.2957	–3.5070	4.4452	–5.1331
dx_1	μm	–0.9128	–1.0305	0.8130	0.9618
dy_1	μm	–3.6956	–4.1721	–3.2912	–3.8938
dx_2	μm	–1.0173	–0.6479	–2.1187	–1.9048
dy_2	μm	–2.3822	–2.2980	–2.7639	–2.7773
dx_3	μm	–2.0681	–2.1471	–2.5406	–2.7981
dy_3	μm	–0.5108	0.5303	–0.6275	0.6911
dx	μm	–1.7200	–1.6505	–2.4008	–2.5022
dy	μm	–3.0389	–3.2350	–3.0276	–3.3355
$d\theta$	μrad	13.135	18.740	5.2732	11.165
$dx_{slip,1}$	μm	0.1045	–0.3827	2.9317	2.8666
$dy_{slip,3}$	μm	3.5395	5.2084	2.8061	4.8864
μ_2	–	0.3458	0.2283	0.6207	0.5553

		Point 3 deforming			
μ_1	–	0.2	0.2	–0.2	–0.2
μ_2	–	0.2	–0.2	0.2	–0.2
$F_{n,1}$	N	19.4051	13.4635	16.4894	11.4963
$F_{n,2}$	N	27.8749	38.2127	32.4416	42.2890
$F_{n,3}$	N	21.8489	36.2548	28.1145	42.0620
$F_{t,1}$	N	3.8810	2.6927	–3.2979	–2.2993
$F_{t,2}$	N	5.5750	–7.6425	6.4883	–8.4578
$F_{t,3}$	N	15.3298	10.9338	13.6789	8.8246
dx_1	μm	–0.5767	–0.4460	0.5184	0.4000
dy_1	μm	–2.3350	–1.8055	–2.0985	–1.6193
dx_2	μm	–0.7273	0.8996	–0.8057	0.9620
dy_2	μm	–2.9444	–3.6422	–3.2619	–3.8948
dx_3	μm	–2.5047	–3.5160	–2.9697	–3.8781
dy_3	μm	–2.1704	–1.3096	–1.7844	–1.0049
dx	μm	–2.6662	–4.0028	–3.2779	–4.4811
dy	μm	–2.6397	–2.7238	–2.6802	–2.7570
$d\theta$	μrad	–6.0941	–18.367	–11.633	–22.755
$dx_{slip,1}$	μm	2.4155	4.5394	4.4187	6.0985
$dx_{slip,2}$	μm	2.2650	5.8850	3.0946	6.6606
μ_3	–	0.7016	0.3016	0.4865	0.2098

It is clear from the table the only tangential force which stays within the limit of the friction is the situation where point 1 is the final point making contact, $\mu_2 = 0.2$ and $\mu_3 = -0.2$. The other points should be calculated based on the maximum friction in appropriate direction. The final values for the alignment model are given in Table 10.

Table 10: Results alignment model

Parameter	Unit	Point 1 deforming			
μ_1	–	0.2	0.1757	0.2	0.2
μ_2	–	0.2	0.2	–0.2	–0.2
μ_3	–	0.2	–0.2	0.2	–0.2
$F_{n,1}$	N	35.7310	45.9063	20.0739	40.6817
$F_{n,2}$	N	22.9658	20.5302	35.6519	27.6687
$F_{n,3}$	N	19.5656	19.1334	34.4205	28.7024
$F_{t,1}$	N	7.1462	8.0655	4.0148	8.1363
$F_{t,2}$	N	4.5932	4.1060	–7.1304	–5.5337
$F_{t,3}$	N	3.9131	–3.8267	6.8841	–5.7405
dx_1	μm	–0.8596	–0.8941	–0.5853	–0.9373
dy_1	μm	–3.4801	–4.1204	–2.3694	–3.7945
dx_2	μm	–0.6402	–0.5908	0.8583	0.7249
dy_2	μm	–2.5919	–2.3920	–3.4749	–2.9346
dx_3	μm	–2.3293	–2.2768	–3.3945	–3.0073
dy_3	μm	–0.5753	0.5624	–0.8385	0.7428
dx	μm	–2.0939	–1.8187	–3.6874	–2.7794
dy	μm	–3.0360	–3.2562	–2.9222	–3.3646
$d\theta$	μrad	8.8821	17.284	–11.055	8.5992
$dx_{slip,1}$	μm	0.7591	0	3.6936	1.3821
$dx_{slip,2}$	μm	0.9785	0.3032	5.1372	3.0442
$dy_{slip,3}$	μm	3.1446	5.1494	1.2325	4.7695
		Point 2 deforming			

μ_1	–	0.2	0.2	–0.2	–0.2
μ_2	–	0.2	0.2	0.2	0.2
μ_3	–	0.2	–0.2	0.2	–0.2
$F_{n,1}$	N	35.7310	46.4921	24.8276	38.4232
$F_{n,2}$	N	22.9658	19.7299	31.8002	30.7544
$F_{n,3}$	N	19.5656	18.0605	29.9104	32.8387
$F_{t,1}$	N	7.1462	9.2984	–4.9655	–7.6846
$F_{t,2}$	N	4.5932	3.9460	6.3600	6.1509
$F_{t,3}$	N	3.9131	–3.6121	5.9821	–6.5677
dx_1	μm	–0.8596	–1.0245	0.6744	0.9023
dy_1	μm	–3.4801	–4.1477	–2.7301	–3.6528
dx_2	μm	–0.6402	–0.5786	–0.7953	–0.7778
dy_2	μm	–2.5919	–2.3423	–3.2199	–3.1489
dx_3	μm	–2.3293	–2.2082	–3.0911	–3.2897
dy_3	μm	–0.5753	0.5454	–0.7635	0.8126
dx	μm	–2.0939	–1.7298	–3.2209	–3.1561
dy	μm	–3.0360	–3.2450	–2.9750	–3.4009
$d\theta$	μrad	8.8821	18.054	–4.8980	5.0383
$dx_{slip,1}$	μm	0.7591	–0.2606	4.1573	3.7888
$dx_{slip,2}$	μm	0.9785	0.1853	2.6876	2.1088
$dy_{slip,3}$	μm	3.1446	5.1807	1.8344	4.6014
Point 3 deforming					
μ_1	–	0.2	0.2	–0.2	–0.2
μ_2	–	0.2	–0.2	0.2	–0.2
μ_3	–	0.2	0.2	0.2	0.2
$F_{n,1}$	N	35.7310	20.0739	24.8276	11.9363
$F_{n,2}$	N	22.9658	35.6519	31.8002	42.2454
$F_{n,3}$	N	19.5656	34.4205	29.9104	42.1413
$F_{t,1}$	N	7.1462	4.0148	–4.9655	–2.3873
$F_{t,2}$	N	4.5932	–7.1304	6.3600	–8.4491
$F_{t,3}$	N	3.9131	6.8841	5.9821	8.4283
dx_1	μm	–0.8596	–0.5853	0.6744	0.4139
dy_1	μm	–3.4801	–2.3694	–2.7301	–1.6755
dx_2	μm	–0.6402	0.8583	–0.7953	0.9611
dy_2	μm	–2.5919	–3.4749	–3.2199	–3.8912
dx_3	μm	–2.3293	–3.3945	–3.0911	–3.8848
dy_3	μm	–0.5753	–0.8385	–0.7635	–0.9596
dx	μm	–2.0939	–3.6874	–3.2209	–4.4719
dy	μm	–3.0360	–2.9222	–2.9750	–2.7833
$d\theta$	μrad	8.8821	–11.055	–4.8980	–22.157
$dx_{slip,1}$	μm	0.7591	3.6936	4.1573	6.0712
$dx_{slip,2}$	μm	0.9785	5.1372	2.6876	6.6184
$dy_{slip,3}$	–	3.1446	1.2325	1.8344	0.1177

Appendix I: Alignment model for maximum friction

The initial displacements are calculated for the maximum friction coefficient $\mu = 0.32$. The dimensions stay the same as for $\mu = 0.2$. Figure 24 shows the initial positioning. Rotations are not shown since they are small.

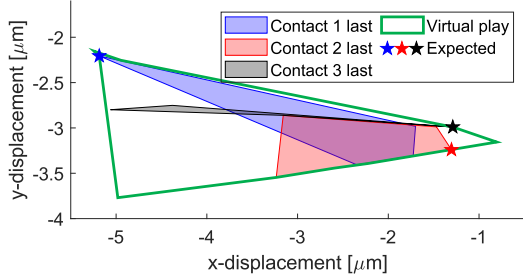


Figure 24: Displacements of the chuck centre depending on the different sequences of contact for $\mu = 0.32$ including the expected final locations

It is clear still contact point 3 has main deviation in x-direction and points 1 and 2 more in x- than y-direction. The uncertainty is smaller than the total virtual play, and the areas follow the edges less than Figure 9. Almost half of the final calculated contact points would still slip and have been taken at their maximum friction. The friction coefficient based on the displacements only are shown in Table 11.

Table 11: Friction coefficients alignment model based on deformation final contact

Parameter	Unit	Point 1 deforming			
μ_2	—	0.32	0.32	-0.32	-0.32
μ_3	—	0.32	-0.32	0.32	-0.32
μ_1	—	0.2391	0.1261	0.5887	0.3011
		Point 2 deforming			
μ_1	—	0.32	0.32	-0.32	-0.32
μ_3	—	0.32	-0.32	0.32	-0.32
μ_2	—	0.2453	0.0287	0.6887	0.6025
		Point 3 deforming			
μ_1	—	0.32	0.32	-0.32	-0.32
μ_2	—	0.32	-0.32	0.32	-0.32
μ_3	—	0.9891	0.2286	0.5236	0.1196

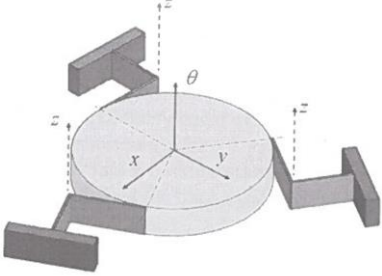
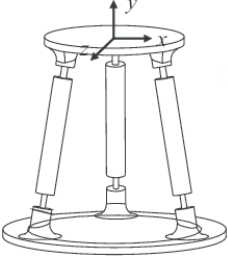
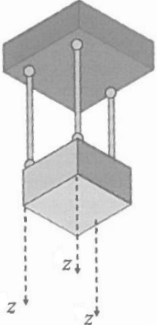
Appendix J: Concept generation

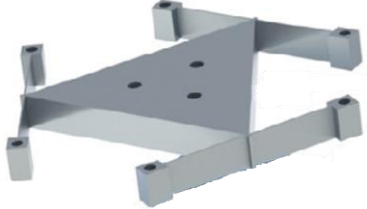
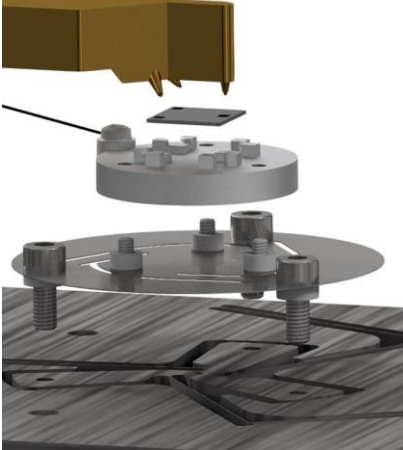
Three main functions of the test set-up will be investigated separately to find viable solutions: restricting a two-dimensional plane, the nesting force and measuring virtual play.

J.1 Restricting a two-dimensional plane

As stated by the first requirement in section 3.1, the chuck should move on a two-dimensional plane. To make sure this happens, it is necessary to restrict three degrees of freedom. Since gravity plays a role in our three-dimensional world, it is easy if the plane is entirely horizontal, to reassure gravity does not influence the two-dimensional plane. In this way, this force does not have influence in the moving direction. Having the test set-up under a different angle is only useful when gravity is used as nesting force. The drawback of this is stated in Table 13. To restrict a two-dimensional plane we will only look at horizontal plane restrictions. To not influence the chuck much and keep the hysteresis low, no active manipulation stages are considered. Table 12 shows possible solutions.

Table 12: Possible two-dimensional mechanisms

Solution	Advantages	Disadvantages
 <p>Folded leaf spring mechanism [14, p.138]</p>	<ul style="list-style-type: none"> - Can handle both tension and compression loads, wherefore forces can go higher than in wire flexures. - No shortening effect. - Equal translational stiffnesses for all in-plane directions. - Set-up be made compact. - (Almost) no hysteresis is induced when attaching. 	<ul style="list-style-type: none"> - Elastic centrum in the middle of leaf springs. - Sagging when moving in plane.
 <p>Supporting struts [27]</p>	<ul style="list-style-type: none"> - Resistant against temperature differences due to little material. - Equal translational stiffnesses for all in-plane directions. 	<ul style="list-style-type: none"> - Substantial risk of buckling. - Test set-up becomes high. - Clamping is difficult and friction within hinges introduces hysteresis. - Sagging when moving in plane.
 <p>Hanging struts [14, p.54]</p>	<ul style="list-style-type: none"> - Resistant against temperature differences due to little material. - Equal translational stiffnesses for all in-plane directions. 	<ul style="list-style-type: none"> - Elongation of the bars due to self-weight differs when moving. - Big test set-up required to attach the struts to a sturdy rigid world. - Clamping is difficult and friction within hinges introduces hysteresis. - Shortening effects when moving in plane.

 <p>Hanging ropes [28]</p>	<ul style="list-style-type: none"> - Resistant against temperature differences due to little material. - Equal translational stiffnesses for all in-plane directions. - Easy to attach wherefore (almost) no hysteresis is induced. 	<ul style="list-style-type: none"> - Might become unstable since cables only apply force when under tension. - Big test set-up required to attach the ropes to a sturdy rigid world.
 <p>Leaf spring platform [29]</p>	<ul style="list-style-type: none"> - Made before. - Can handle both tension and compression loads, wherefore forces can go higher than in wire flexures. - (Almost) no hysteresis is induced when attaching. 	<ul style="list-style-type: none"> - Elastic centrum in the middle of leaf springs. - Shortening effects when moving in plane. - Broad test set-up required.
 <p>Restricting plane due to folded leaf springs with a tip-tilt mechanism [3]</p>	<ul style="list-style-type: none"> - Made before. 	<ul style="list-style-type: none"> - Sliding over surface causes unwanted hysteresis due to in-plane friction.
 <p>Air bearings [30]</p>	<ul style="list-style-type: none"> - No hysteresis. 	<ul style="list-style-type: none"> - Expensive.

In the end the folded leaf spring mechanism is chosen for the final test set-up. It is less expensive than the air bearings and will not induce hysteresis. Furthermore, it will deform the least unevenly in out of plane directions. The floating neutral position will become the elastic centre and should become the application point of the nesting force if possible. The detailed design of this mechanism is explained in section K.3.

J.2 Nesting force

Since the way of making a two-dimensional mechanism is known, it is important the alignment of the chuck is carefully done. The force application method becomes the second important design choice. Since the order of contacts must be controlled, but the total force should stay the same for every test, this will be hard to realise with just one nesting force. It is possible to use different orientations for the chuck, but controlling these carefully is not favourable. Multiple forces have to be used to change the contact order. This way, the final alignment will happen under the same circumstances. For all tests, the final nesting forces should have the same magnitude and orientation, to be able to compare them fairly. Self-locking should be prevented as explained in the worst-case theory in chapter 1 [12]. Figure 25 shows a schematic representation about how a single force should be aligned. Table 13 shows possible solutions to apply the forces.

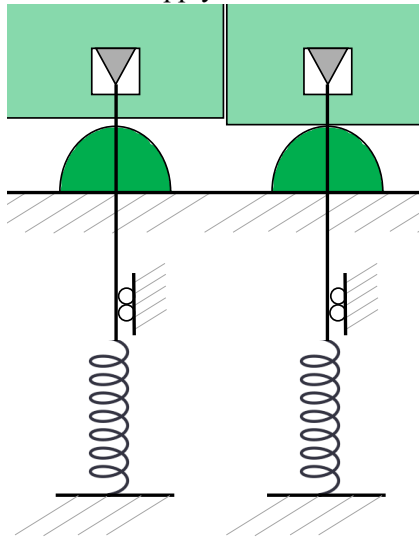
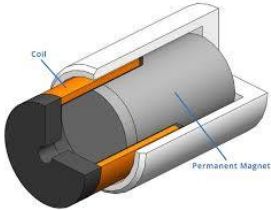
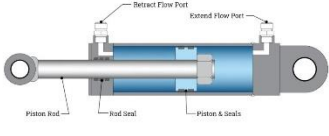
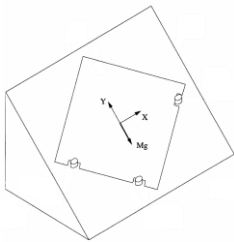
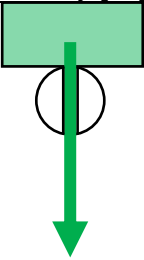
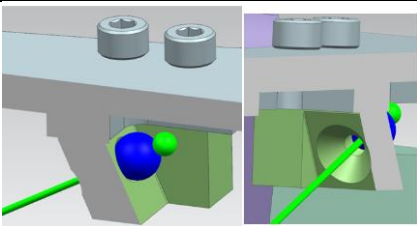
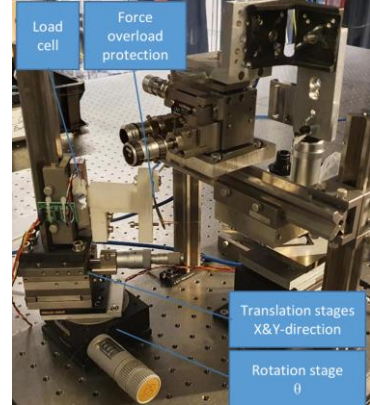


Figure 25: Schematic representation of alignment with the force application

Table 13: Possible force application methods

Solution	Advantages	Disadvantages
 <p>Voice coil actuator [31]</p>	<ul style="list-style-type: none"> - Low hysteresis. - Simple construction. 	<ul style="list-style-type: none"> - Hard to adjust while testing. - Mainly good for pushing, which happens far away from the contacts and is therefore less accurate to steer the chuck.
 <p>Piezoelectric actuator [32]</p>	<ul style="list-style-type: none"> - High resolution. 	<ul style="list-style-type: none"> - Hard to adjust while testing. - Mainly good for pushing, which happens far away from the contacts and is therefore less accurate to steer the chuck.
 <p>Hydraulic actuator [33]</p>	<ul style="list-style-type: none"> - Good for high forces. 	<ul style="list-style-type: none"> - Hard to adjust while testing. - Mainly good for pushing, which happens far away from the contacts and is therefore less accurate to steer the chuck.

		<ul style="list-style-type: none"> - Mainly working precise by use of an additional sensor. - Pressurising fluid can cause hysteresis.
 <p>Gravity [34]</p>	<ul style="list-style-type: none"> - Cheap. - Constant force. 	<ul style="list-style-type: none"> - Cannot be switched of, so counterforce is needed to make the chuck go to its neutral position. - Changes orientation when using different alignment routes.
 <p>Wires through balls</p>	<ul style="list-style-type: none"> - Force is applied at the contact point. 	<ul style="list-style-type: none"> - Contact surface discretized.
 <p>Wires with weights [13]</p>	<ul style="list-style-type: none"> - Researched before. 	<ul style="list-style-type: none"> - Possible hysteresis due to extra induced friction of pulleys. - Cannot be automated for repetitions.
 <p>Screw spindle [35]</p>	<ul style="list-style-type: none"> - Clear orientation of the forces. 	<ul style="list-style-type: none"> - Mainly good for pushing, which happens far away from the contacts and is therefore less accurate to steer the chuck. - Cannot be automated for repetitions.
 <p>Planar stage [36]</p>	<ul style="list-style-type: none"> - Only one stage needed instead of 3 separate forces. 	<ul style="list-style-type: none"> - No rotations and therefore not all alignment routes possible. - Cannot be automated for repetitions.

	<ul style="list-style-type: none"> - Made before. 	<ul style="list-style-type: none"> - Cannot be automated for repetitions.
<p>Wires with translational stage [3]</p>		

Based on all possible solutions it is chosen to use the wires with translational stages in the final test set-up. This is a method which is implemented before and is simple to implement for small test quantities. It is easy to make small adjustments during the testing. Just like the test set-up of Seubers [3] a loadcell will be implemented in the mechanism to make sure the applied force is known. This is necessary for requirement 4, as explained in section 3.1.

Since the test set-up resembles a two-dimensional world, it is possible to apply the force at the contact locations by working in three dimensions. However, to not obtain any unwanted rotational effects due to the three-dimensional application, it is chosen to apply everything in the plane. The forces will thus be applied due to ropes tied to the chuck in the same plane as the contacts. A detailed explanation of this mechanism is given in section K.5.

J.3 Measuring virtual play

The final important function is the measurement of the virtual play. The location of the chuck should be known after alignment, to observe how this differs for different tests. To verify the model, the virtual play should be measured in the same way as the model is build up. This means the displacements of the chuck should be measured on all three contact points as explained in section 3.1. There are multiple sensors possible to measure displacements, which are stated in Table 14.

Table 14: Possible measuring devices

Solution	Advantages	Disadvantages
 <p>Camera [37]</p>	<ul style="list-style-type: none"> - Actual contact points can be visualised. - Displacement of the middle of the chuck can be shown as well. - Does not require contact. 	<ul style="list-style-type: none"> - Filming requires a high resolution to obtain a good accuracy and is thus expensive. - Showing the entire chip won't give a high enough resolution, so only subparts can be compared. Taking photos would be better, but this may cause disturbances after settling which is an effect that should be neglected.
 <p>Compression loadcell [38]</p>	<ul style="list-style-type: none"> - Relatively cheap. 	<ul style="list-style-type: none"> - Measurement requires contact which causes reaction forces and might limit the movement of the chuck.

		- Not possible to measure at the exact location of the contact.
 <p>Optical sensor [39]</p>	- Does not require contact.	- Material dependent, so needs to be calibrated well for different materials.
 <p>Capacitive sensor [40]</p>	<ul style="list-style-type: none"> - Does not require contact. - High accuracy. - Available within university of Twente. 	<ul style="list-style-type: none"> - Expensive. - Not possible to measure at the exact location of the contact.

Looking at the advantages and disadvantages the capacitive sensor is the most suitable candidate. The University of Twente has capacitive sensors available, wherefore the high costs are not an issue.

Since the capacitive sensors cannot be placed directly at the contacts there are multiple locations possible. Just like the force locations, the capacitive sensors will also be placed in plane to prevent influence of small accidental out of plane rotations. If the sensors are placed as far away from each other as possible, the total virtual play from the chuck is captured best. Contact point indentations will be calculated by triangulation.

The contact points itself will be most reliable if they are far away from each other. This is because the sequence of contact can be better controlled in that way. If the contacts would be close together, this would lead to more rotating of the chuck due to small displacement variations. At the same time, the forces in each point cannot really be controlled well for the contacts separately and then the contact sequence will become more unreliable. Both the contact points and the sensor locations will be chosen close to the edges of the chuck and will be next to each other. The specifications of the sensors are given in section K.4.

Appendix K: Detailed design

K.1 Material choice

The higher the virtual play, the easier it is to measure. To verify the model, it is important the contacts itself will have as big as possible displacements. The Hertzian contact model showed the normal displacements rely on both the forces and material properties. The stress in the contacts increases based on the forces as well. To find the maximum force and corresponding contact stiffness for different material properties, these are plotted for different radii in Figure 26.

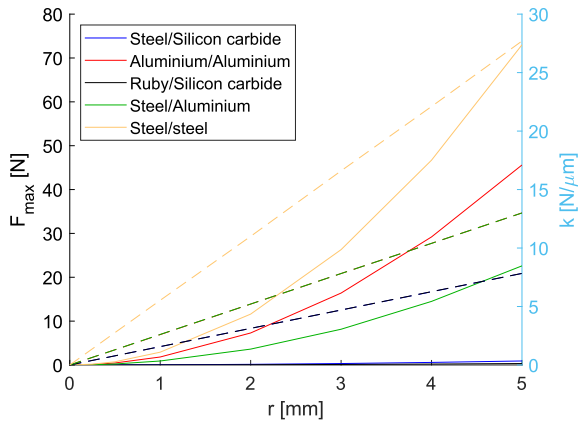


Figure 26: Force (solid line) and stiffness (dashed line) vs ball radius

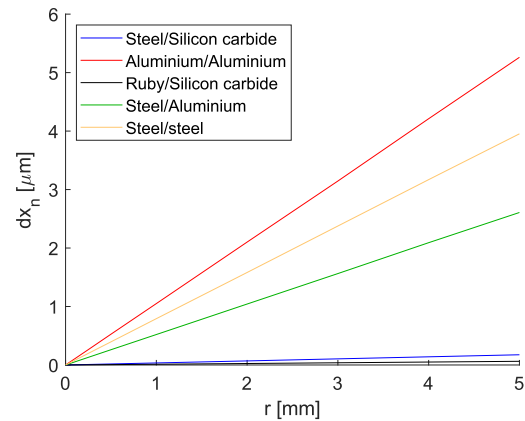


Figure 27: Normal indentation based on Hertzian contact model for maximum force which keeps the Von Mises stress below the Yield strength

The forces are found based on the stresses of the Hertzian contact model using Hertzwin [24]. The materials are chosen based on previous used testing materials [3], [13] and common available materials. Material properties are stated in Table 15.

Table 15: Material properties

Material	Young's modulus [GPa]	Poisson ratio [-]	Yield strength [MPa]
Steel	180	0.29	1100
Aluminium	71	0.33	500
Ruby	440	0.30	2100
Silicon carbide	395	0.17	340

To find these limiting displacements both the yield strength of the balls and the contact surfaces are taken into account. After calculating both, the lowest, and therefore most critical value, is used. For the chosen combinations, these critical values showed up in the surfaces, although for when the same materials make contact the stresses are equal.

Using the found forces, the indentations of the contacts are plotted (Figure 27). The quadratic relationship between the force and the radius cancels out with the inverse relationship of the stiffness for the displacements. The figure shows despite the fact steel is able to handle the highest force, aluminium still causes the largest displacement. Despite the high yield strength of steel, the Young's modulus is also much higher than aluminium which causes this difference. One should remark the force and stiffness might not just be divided to obtain the previous shown displacement, since the plot shows the local stiffness, not secant and they differ with a factor of 1.5 as explained in section 2.1.3.

Although aluminium on aluminium is seemingly the best option, using the same materials on contact points is unwise according to Matthijn de Rooij, professor in the field of tribology at the University of Twente. When making contact with the same metals on each other, this might lead to metal binding if small damages take place. Steel balls with a radius of 5mm are chosen for the test set-up. The contact surfaces will be made from aluminium.

Since the contacts itself will be made from aluminium, it is chosen to also produce the other parts from aluminium. This way parts which make contact will react in the same way to small disturbances, like temperature fluctuations, which might cause small shrinkages and expansions in the material. Therefore, internal stresses due to these variations will be minimised. The entire test set-up will be mounted to a bottom plate, to align everything properly. By making this of aluminium as well, these influences are consistently applied everywhere.

K.2 Contact design

K.2.1 Ball holder design

Since the balls will be on the base, a ball holder should be designed to hold them. In previous thesis assignments Seubers [3] designed cylindrical pockets to which balls could be glued and Neulen [13] designed conical holes. For this test set-up, balls shall be glued in pockets as well. Roy Kooijman, supporting staff of the precision engineering faculty, recommended using a 2-component glue to fixate the balls. Seubers evaluated two different glues and chose Araldite epoxy and Neulen proposed two different glues, one of which was Araldite 2030. It is chosen to use an Araldite 2-component epoxy for this set-up as well. For the holes it is chosen to use the dimensions of manufacturing tools. This gives a cylindrical cone with an angle of 118°. Figure 28 shows the cylindrical part added to the cone to make sure the balls are placed more inside the holes. The radius of the ball at the front of the holder is 0.067mm smaller than the total radius of the cylinder, which leaves space to glue the balls into the holders.

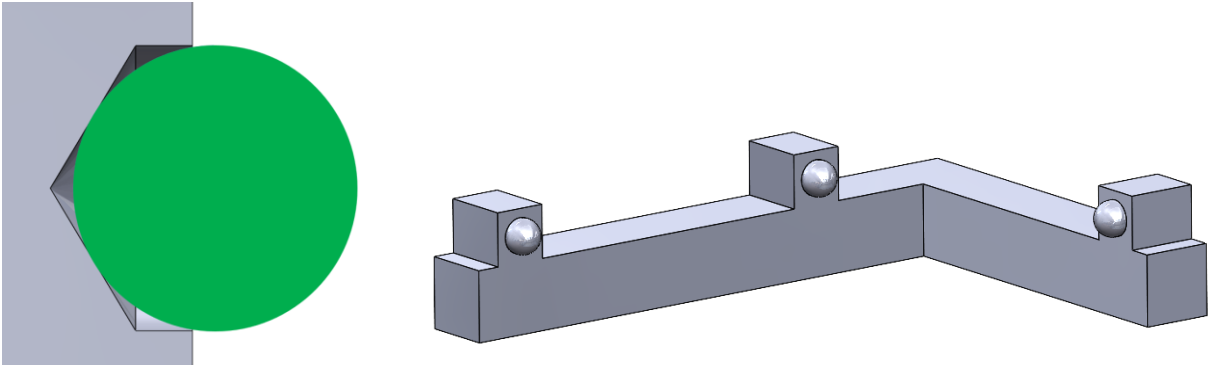


Figure 28: Cross section ball holder Figure 29: Initial design ball holder

Figure 29 shows the original idea for this set-up where the entire ball holder was made out of one part. By connecting all balls, possible unwanted displacements will be absorbed equally. Due to the space needed for forces and sensors, the shape could become complex wherefore manufacturing costs would increase. Since the entire test set-up will be mounted to a bottom plate, it was chosen to make separate holders for all three balls. To mount them well on the bottom part and decrease unwanted rotational effects, at least 2 bolts are used to attach the holders to the bottom plate. However, keeping the design symmetrical was not as straightforward as it first appeared (Figure 30).

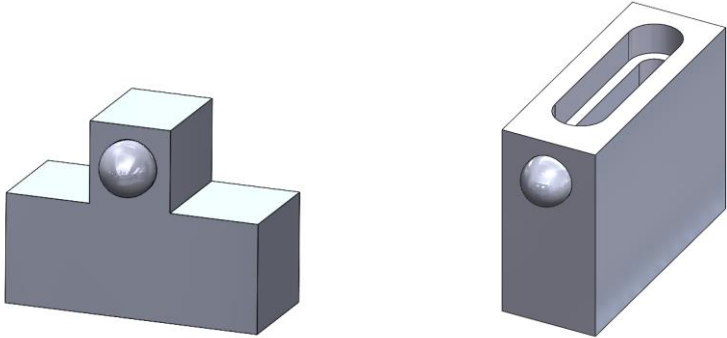


Figure 30: Improved design ball holder Figure 31: Final design ball holder

Using space for mounting at the sides of the ball, took again space of the sensor holder, which should then be far away from the contacts. These unwanted results led to multiple redesigns. In the end it is chosen to align these bolts with the holes in the bottom plate to the back (Figure 31). Next to decreasing the manufacturing costs, this also made sure there is more material behind the contacts, wherefore unwanted deformation will be absorbed far in the material. A technical drawing of the ball holder is given in Appendix M.

K.2.2 Contact surface

The balls will make contact with the surface planes, which might cause wear. To make sure the experiment can easily be repeated, even if things go wrong, it is chosen to make the surface from separate plates, which will be connected to the chuck. This way the plates can be changed if wear starts playing a role. Furthermore, different materials can be tested as well with the same test set-up. Figure 32 shows the plates are connected to the chuck with 4 bolts. A technical drawing of the plates is given in Appendix N.

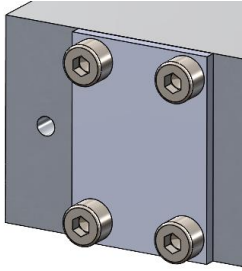


Figure 32: Surface plate connected to chuck

K.3 Leaf spring mechanism

K.3.1 Optimising dimensions

The dimensions of the leaf springs should be such the nesting force only needs a neglectable small part to move the chuck in plane. In that way the stiffness of the leaf springs can be neglected when comparing the applied forces with the model to check the virtual play. It is important the stiffness in the z-direction is orders of magnitude higher than in the compliant directions.

Since the forces will be maximal 45N, the in-plane stiffness should be at least an order lower. Introducing a millimetre of travel distance, which is more than will actually be used, this gives a maximum compliant stiffness of 4.5N/mm.

For the in-plane direction the stiffness of a leaf spring mechanism is given by [14, p.138]

$$c_{plane} = \frac{45 \cdot E \cdot I}{2l^3} = \frac{15 \cdot E \cdot wt^3}{8l^3} \quad (31).$$

Here I is the area moment of inertia and l , w and t are the length, width and thickness of the leaf spring. In the direction of the fold, the stiffness of one leaf spring is given as [14, p.120]

$$c_{fold} = \left\{ \frac{2l^3}{3EI} + \frac{6}{5} \cdot \frac{2l}{G \cdot A} \right\}^{-1} \quad (32).$$

This means for 3 parallel leaf springs a total stiffness will be obtained as

$$c_z = 3 \cdot c_{fold} = 3 \cdot \left\{ \frac{8l^3}{Ew^3t} + \frac{6}{5} \cdot \frac{4l(1+\nu)}{E \cdot wt} \right\}^{-1} \quad (33).$$

An initial dimensioning gives for values of Table 16 the stiffnesses as $c_{table} = 1.33N/mm$ and $c_z = 103N/mm$.

Table 16: Initial values leaf spring mechanism

Property	Unit	Value
$E_{aluminium}$	GPa	71
$\nu_{aluminium}$	–	0.33
l	mm	50
t	mm	0.5
w	mm	10

There are several ways to attach leaf springs to mechanisms [41]. If the flexures would be applied to the outside of the chuck, while keeping the design symmetrical, the mechanism would either become really big or the leaf springs would be in the way of the force applications and ball contacts. In the worst case both scenarios take place. The first concept made for the leaf spring mechanism was based on a previous thesis design [3]. The chuck would be on top of the leaf spring mechanism. Figure 33 shows there was a plate in between to attach the leaf springs to the chuck. However, this leaves a lot of unnecessary material at the chuck. Since a small length of 50mm already led to reasonable results for the stiffnesses, the dimensions could be made smaller, so the chuck could become immediately on top. Figure 35 shows the leaf spring mechanism was redesigned to become more compact as well. The angle of the leaf springs does not matter much as long as it does not become close to 0° [14, p.120].

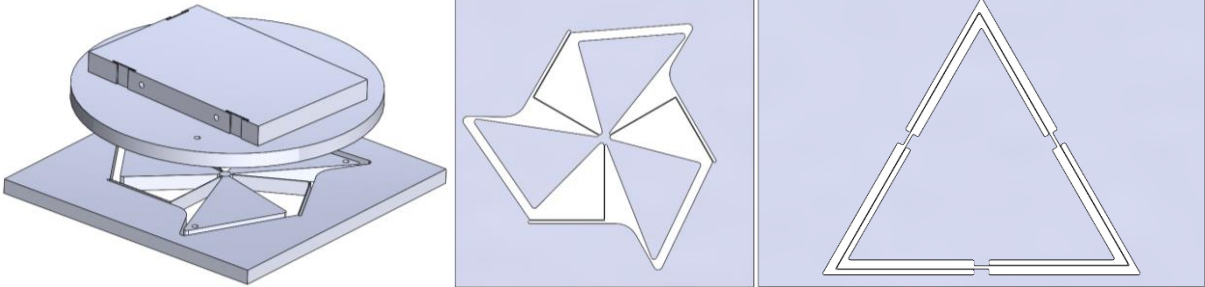


Figure 33: Initial design chuck with leaf springs Figure 34: Initial design leaf springs Figure 35: Compact design leaf springs

While originally multiple assembling methods were taken into account, this is not the case going forward. It will not be favourable to manufacture the leaf springs separately to the rest of the stage using this design. The compact dimension make it quite hard to assemble everything. Changing the design for easier assembling, while keeping it compact is not possible or would increase the manufacturing costs a lot. Making the entire stage out of one part by means of wire EDM causes better alignment and will be the preferred solution.

The system is modelled within Spacar to validate the stiffnesses. The flexures are modelled with 3 rectangular beam elements per leaf spring. The middle is connected with rigid elements without any mass. A point mass of 1kg is applied to compensate for the chuck at the centre of the triangle. Figure 36 shows a displacement of 1mm in the x-direction is modelled at the centre point. The needed force corresponds to the stiffness in the compliant direction. This gives $c_x = 1.23N/mm$ with a maximum Von Mises stress at the leaf springs of 49.9MPa.

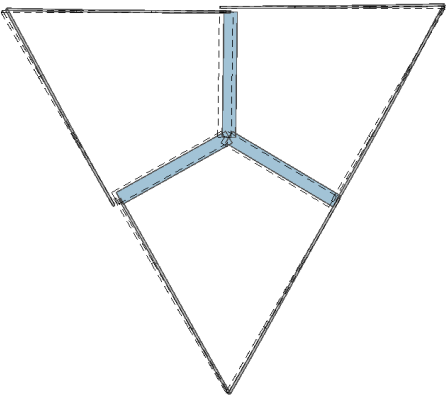


Figure 36: Deformation leaf springs Spacar for a x-displacement of 1mm

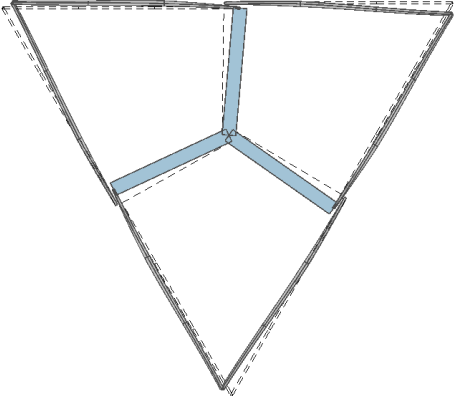


Figure 37: Rotations for displacement z-direction Spacar

Running the same model for a displacement in the y-direction, gives the same stiffness with a maximum Von Mises stress 51.6MPa. The stiffness is comparable to the calculations made before. The stresses are far below the yield stress and will not be taken into account further while designing. In the z-direction

the needed force appears way lower than calculated before as it becomes $c_z = 67.7 \text{ N/mm}$. However, this is not a neat displacement, but also slight rotation of the leaf springs, which explains the difference (Figure 37). The maximum Von Mises stress now becomes 198 MPa , which is already closer to the yield stress.

Next to comparing the stiffness, it is also important to look at the sagging in the z-direction when displacing in the x-direction (Figure 38). The force increases gradually to move the chuck in x-direction, while the z-displacement shows a quadratic relationship for the sagging. The sagging is $1.19 \mu\text{m}$ and becomes $1.21 \mu\text{m}$ when displacing in y-direction. This is not even an order lower than the indentation of the contacts as found in Appendix F. Redesigning needs to be done to optimize the dimensions of the leaf springs. A brief look into 4 leaf spring mechanisms was taken. However, they do not seem to perform as much better as the equations do suggest, while it does lead to one overconstraint. This idea was therefore rejected.

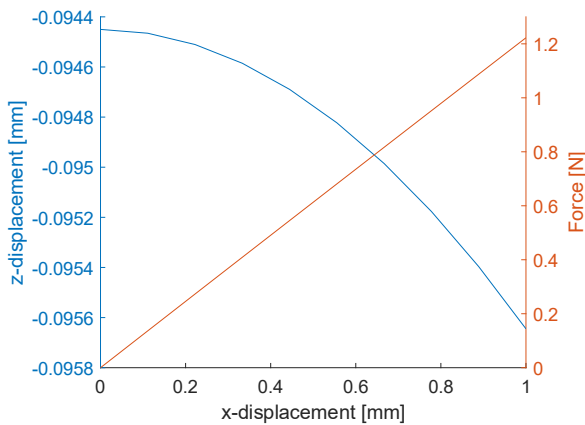


Figure 38: Z-displacement and force for x-displacement of 1mm

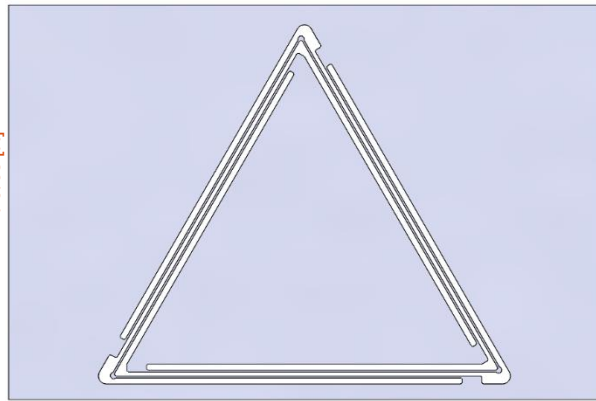


Figure 39: Leaf spring mechanism with maximal flexure length

Lots of design iterations are calculated with Spacar, to find the optimal dimensions (Appendix O). It is chosen to give both the chuck and the entire leaf spring mechanism the same dimensions. For this compact design this means a blade of a leaf spring should have a maximum length of 90 mm (Figure 39). Since the ratio between the stiffness is mainly based on $\frac{w^2}{t^2}$ the lengths of the leaf springs should not impact the ratio. The shorter the leaf springs are made, the thinner the flexures can be made while keeping a high enough support stiffness. The ratio will become better, so a shorter leaf spring is expected to perform comparatively better. Although this is ratio-wise the case, the absolute values will not become as good as the longer leaf springs, due to the increased shearing effect. Data was generated for leaf springs with lengths between 50 mm and 90 mm in increments of 10 mm .

For the width, dimensions between 30 mm and 50 mm are used in increments of 5 mm . The smaller the width, the worse off the ratio is, so below the 30 mm leaf springs did not perform well. Making the leaf springs wider, would not only increase stiffness ratio, but also increase manufacturing time and costs, wherefore this was undesirable.

While optimising the dimensions, reinforcement of leaf springs was also taken into account. According to the design guidelines for reinforcement ratios [42] a general length of the reinforced part takes between $\frac{1}{10}$ and $\frac{1}{3}$ of the total length. Since a typical value is $\frac{1}{6}$, this dimension was used in the optimisation. The typical thickness ratio is between $\frac{1}{10}$ and $\frac{1}{2}$. Taken this ratio at the typical value, which is in this case $\frac{1}{5}$ would decrease the maximum possible length of a leaf spring, wherefore this is undesirable. Therefore, the small factor of $\frac{1}{2}$ was assessed as well as a slightly bigger possibility of $\frac{2}{5}$. This way the maximum length for reinforced leaf springs was taken as 80 instead of 90 mm . For the same reason, the maximum thickness which was taken into account is 0.7 mm . Although smaller

thicknesses are favourable in terms of stiffness ratios, Andre Eppingbroek, supporting staff of the Techno Centre for Education and Research, indicated thicknesses below 0.5mm would be hard to produce. In the end, only thicknesses of $0.5, 0.6$ and 0.7mm were used to generate data, with and without reinforcements. The generated data was sorted based on the force it takes to reach the desired displacement of 1mm in the x-direction, while taking a maximal sagging of $0.2\mu\text{m}$. Table 17 shows the final chosen dimensions.

Table 17: Final dimensions leaf spring mechanism

Thickness	Thickness reinforced	Width	Length	Stiffness x-direction	Stiffness z-direction	Sagging
0.6mm	1.2mm	35mm	80mm	2.9713N/mm	1546.3N/mm	$0.1988\mu\text{m}$

K.3.2 Validating the final design

After finalising these dimensions, it became clear the leaf spring mechanism could now also be used as the chuck. Since the dimensions stay within the same limits, this makes sure the leaf springs are equally loaded. This way no unwanted rotations will be added to the sagging effects, wherefore the system will perform better. Figure 40 and 41 show the final design.

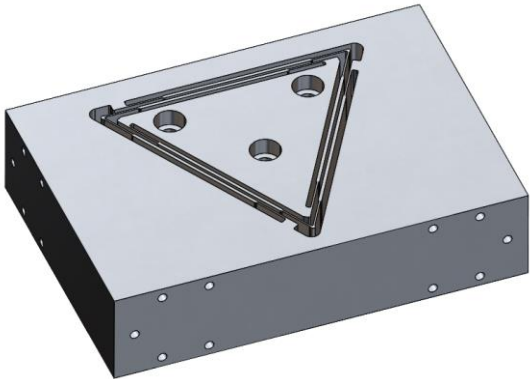


Figure 40: Final design chuck

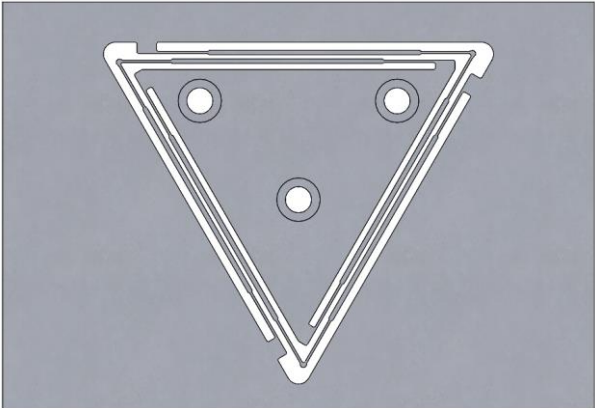


Figure 41: Final design leaf springs

To make sure the design indeed performs as desired, the behaviour is also checked within SolidWorks. Simulations were carried out to find the minimal forces at every point, to move the corresponding contact 1mm . Carrying out one displacement only needed forces with a maximum of 2.2N (Appendix P). Moving all points at the same time at least a millimetre requires higher forces. Still only a maximum of 3.5N was needed, so this is within the range of the asked 4.5N/mm . For these displacements the leaf springs still do not make contact anywhere (Figure 42). Therefore it is clear the space there is big enough as well. While testing it is important to keep in mind there is not a big gap left, so no higher displacements should be tested.

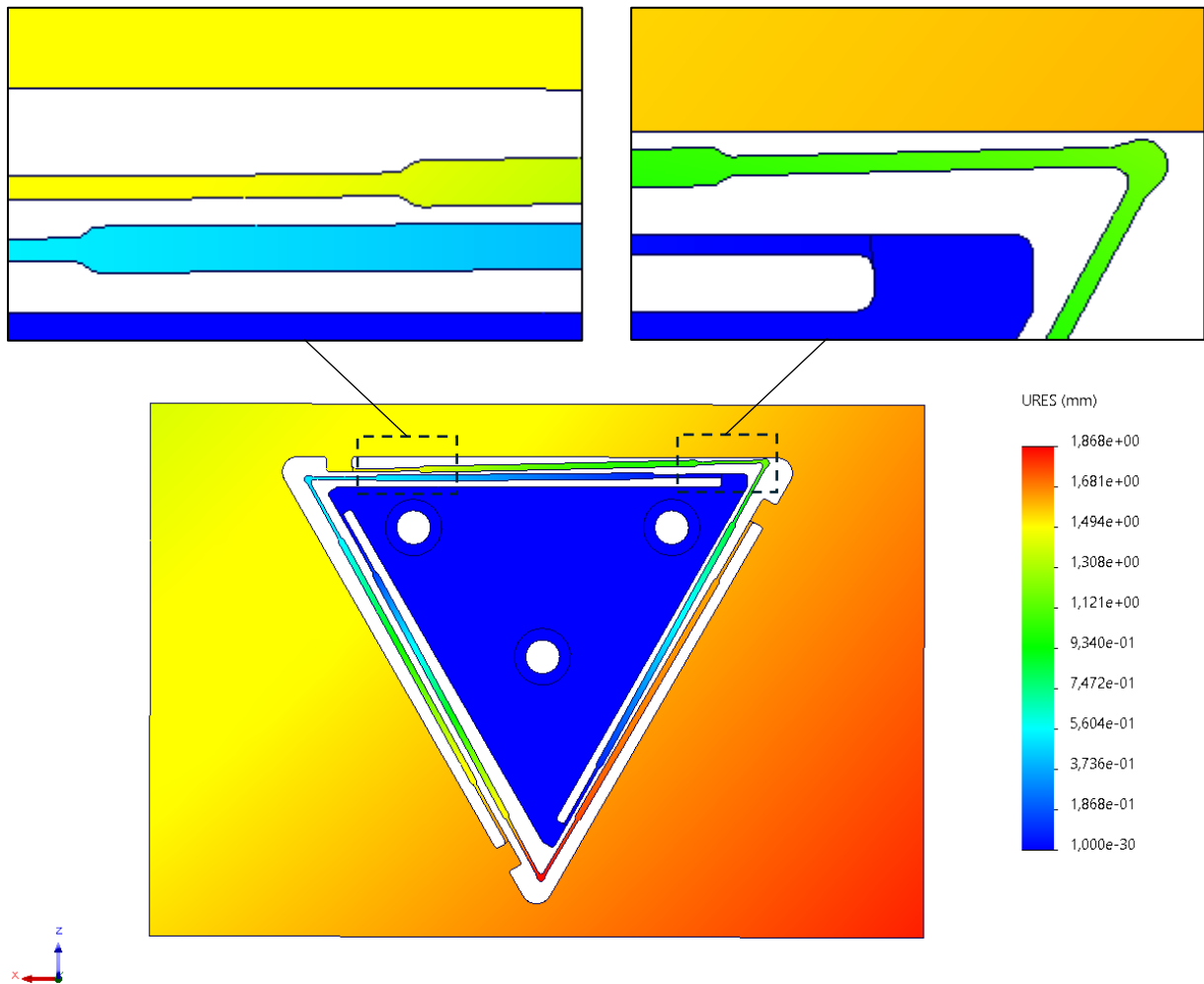


Figure 42: Total displacements of the chuck for $F_{a,1} = 1.0N$, $F_{a,2} = 2.8N$ and $F_{a,3} = 3.5N$. A gap is visible between the leaf springs and the chuck.

The part will be made of aluminium 6082 which has a yield strength of $270MPa$ [43]. The Von Mises stress also stays well within the limit of the material for these displacements (Figure 43). The figure shows the maximum stress takes place at the thin part of the leaf flexures which is as expected.

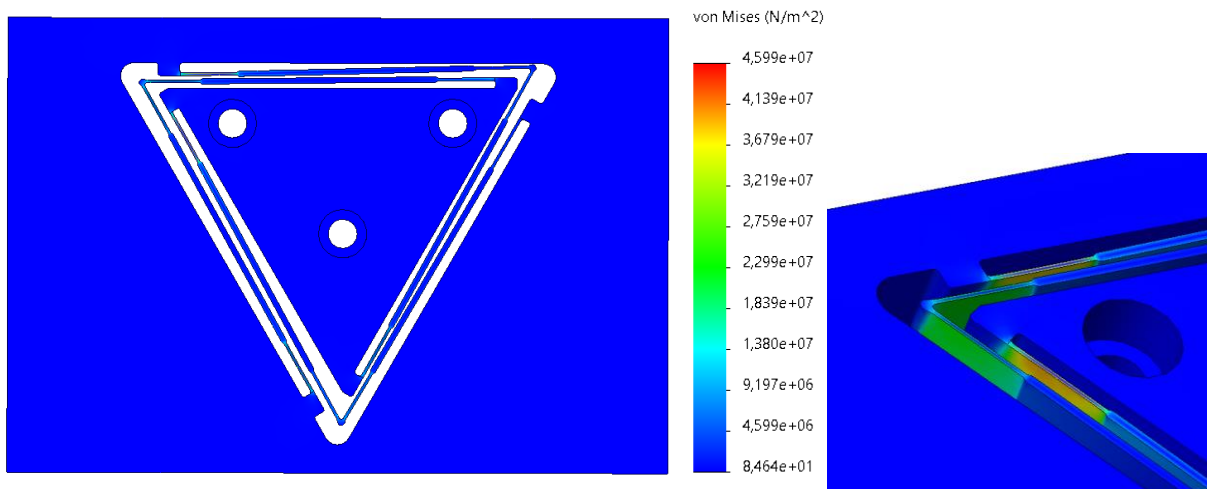


Figure 43: Von Mises stress of the chuck for $F_{a,1} = 1.0N$, $F_{a,2} = 2.8N$ and $F_{a,3} = 3.5N$. Highest Von Mises stress appears at thin parts flexures

K.4 Capacitive sensors

There are several capacitive sensors available at the University of Twente. Table 18 gives their different ranges. It is preferable to use sensors with a range as big as possible, to keep the chuck in sight of the sensors at all times. Since three sensors are needed and there are only two of the sensors with the biggest range available, they are not a possibility. It is chosen to use the sensors with the range of $500\mu\text{m}$.

Table 18: Data capacitive sensors available at University of Twente

Sensor	Broad range [μm]	Small range [μm]	Amount
C8-3.2	1250	50	2
C6-D	500	50	8

The sensors will be connected to a driver with model CPL290. The calibration sheets of the used sensors are given in Appendix Q. The data will be read out in Matlab with a Speedgoat including a IO191 I/O module.

The sensors should be repositioned often, to precisely measure really small displacements. Furthermore, they should be carefully clamped, while not damaging the sensor itself. The original idea was to integrate the sensor holders in the ball holders as well. This would make the holders asymmetric, due to the space needed at the other side of the balls for the force application. When applying a force at the balls when making contact, it would be possible for the holder to slightly rotate due to this asymmetry. It is chosen to apply both the sensor holder and ball holder separately to the bottom plate. This reduces these influences, wherefore these rotations do not need to be taken into account anymore.

When looking for buyable parts to clamp the sensors, a construction was found using a screw with a soft tip, wherefore the sensors will not be damaged. The holder can be mounted on the bottom plate at any distance (Figure 44).

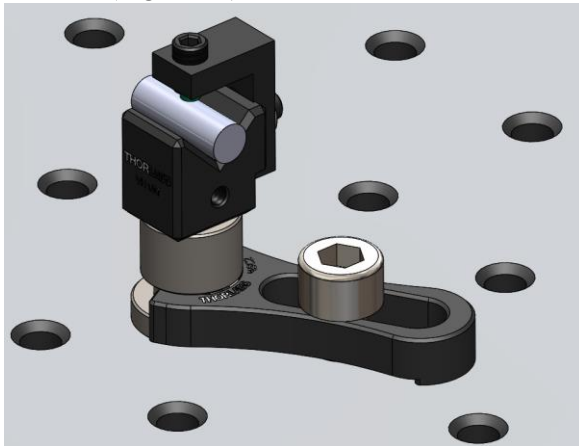


Figure 44: Clamping of sensor holder

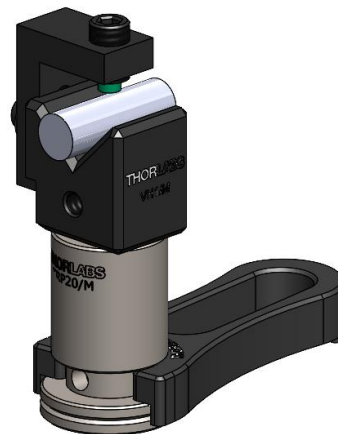


Figure 45: Final sensor holder

The downside of this construction is the height of the sensor is minimal 26mm which is more than half of the chuck. Using this application point would cause a slightly asymmetrical load on the leaf spring mechanism. This is unwanted and should be prevented. One way to fix this, is by measuring out of plane. Since this is also not favourable, it is chosen to increase the entire chuck, including force applications and contact points. To keep more standardised buyable parts, the sensor location height increased even further (Figure 45).



Figure 46: Sensors halfway chuck

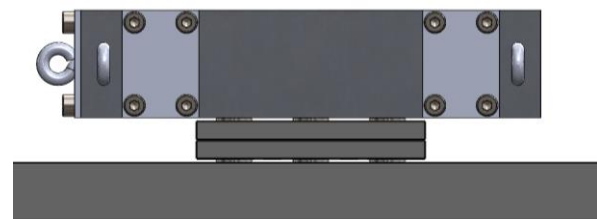


Figure 47: Heightened chuck

K.5 Force application

As mentioned in Appendix J the nesting force will be applied with wires at three separate points at the chuck. This would be combined with translational stages to apply forces at the chuck. A linear stage is found which can handle loads of $10kg$. The stages have a total range of $25mm$ and apply $1mm$ per rotation. By putting a mechanism on top of the linear stages, loadcells are attached to measure the forces applied to the chuck. This way, the loadcells are applied in vertical direction wherefore the gravity does not influence them. The loadcells are also taken such that their maximum measurable load is $10kg$. The signal of the loadcells was amplified with Honeywell DV-10 In-Line Amplifiers. The data will also be read out with a Speedgoat, just like the capacitive sensors. The calibration method for the loadcells is given in Appendix R.

Figure 48 shows the total mechanism which will be used to apply the forces. The lower holes of the loadcells are now exactly halfway the chuck and the forces are applied horizontal when the ropes go through them. The standardized angled blocks need one extra hole to be able to attach the loadcells. Appendix S shows the technical drawings for these adjustments. Figure 49 shows the mechanism screwed on the bottom plate with the ropes attached.

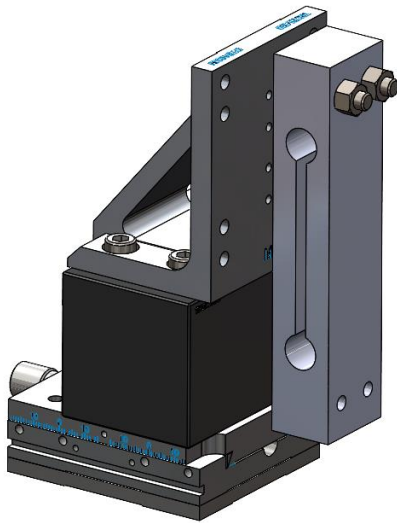


Figure 48: Force application

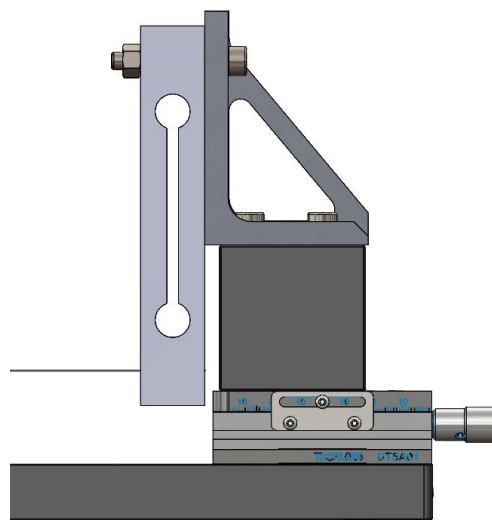


Figure 49: Final assembled force application

The rope is made of dyneema due to its high tensile strength. This way, the loadcell will be the most compliant part of the force mechanism. Initially it was discussed to apply a spring in between the loadcell and the chuck to control the compliance. In the end it was chosen not to add this, to first observe if the system would be valid this way.

The ropes will be attached to the chuck with screw eyes. They could be attached either on the inside or outside of the ball contact points. Initially they were chosen at the inside, to give as much space as possible for the capacitive sensors to measure the virtual play. However in the end they were chosen at the outside, to not release tension due to rotating effects when the ropes are tightened one-by-one.

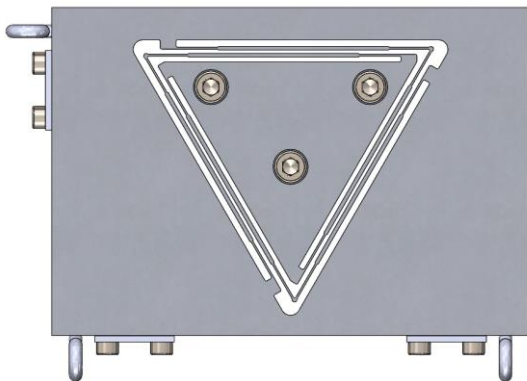


Figure 50: Top view assembled chuck without ropes

Appendix L: Friction test

It is possible to determine the friction coefficient between the ball and a plate, based on a ball and two plates [44]. One of the metal plates is clamped at the table, with the ball on top. Figure 51 shows a second plate placed on the ball, which it is hinging at the clamp.



Figure 51: Friction test set-up steel ball on aluminium plate

The ball is firstly pushed closely to the hinge and slowly moved outwards till it stops moving due to the friction between the ball and the plate. The largest angle for which the set-up does not slip can be used to determine the friction coefficient. The experiment is repeated 15 times to find the biggest angle β the plates make. Table 19 states the results.

Table 19: Angles friction test rounded to whole angles

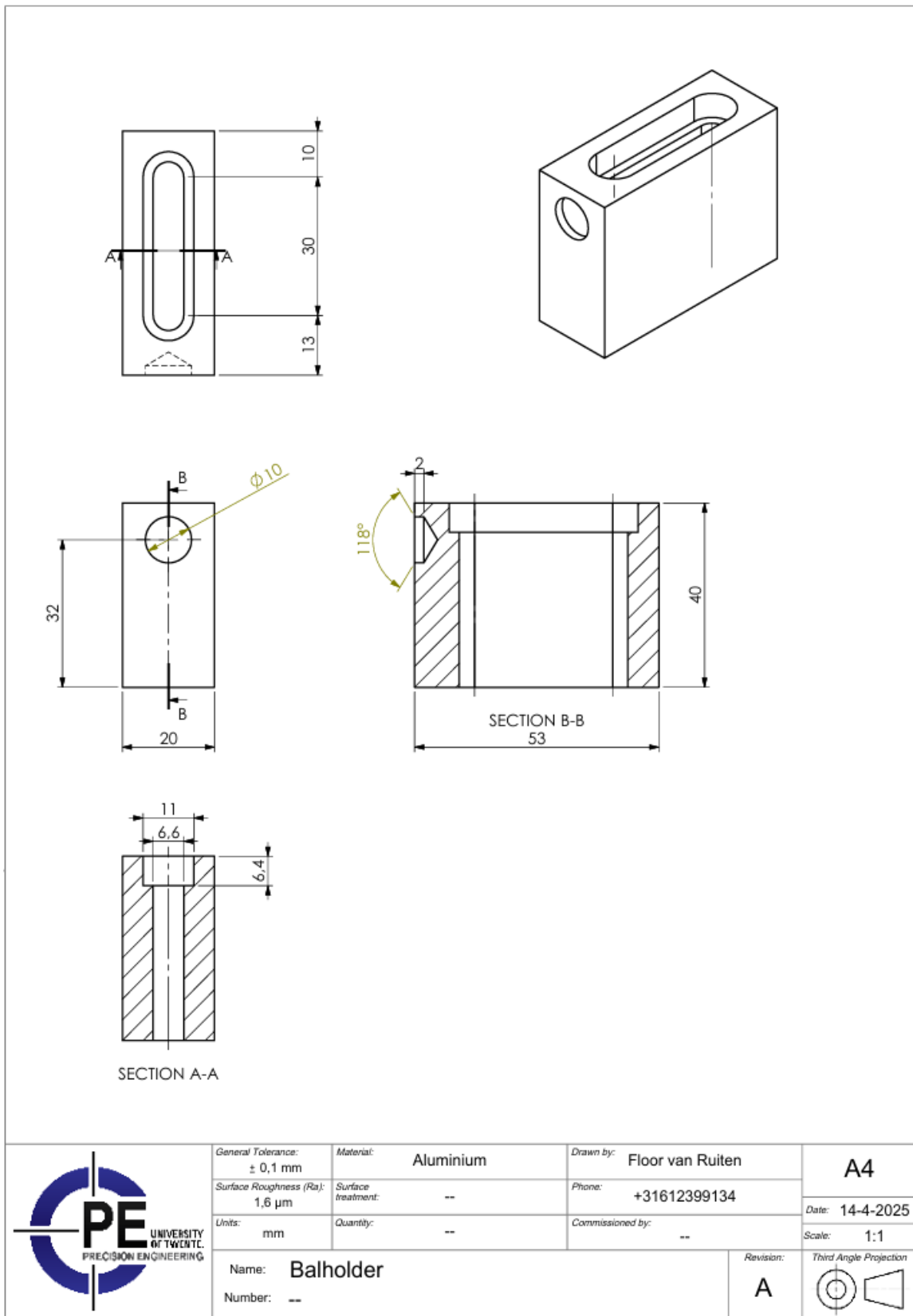
Angle β [°]	Amount
19	1
20	2
21	6
22	4
23	2

The photos which lead to 23° are checked in more detail to determine the maximum angle as $23 \pm 0.1^\circ$. Small uncertainties in the angle are possible due to a distorted perspective of the camera. This way the angle could look bigger than it is. The friction coefficient is calculated using

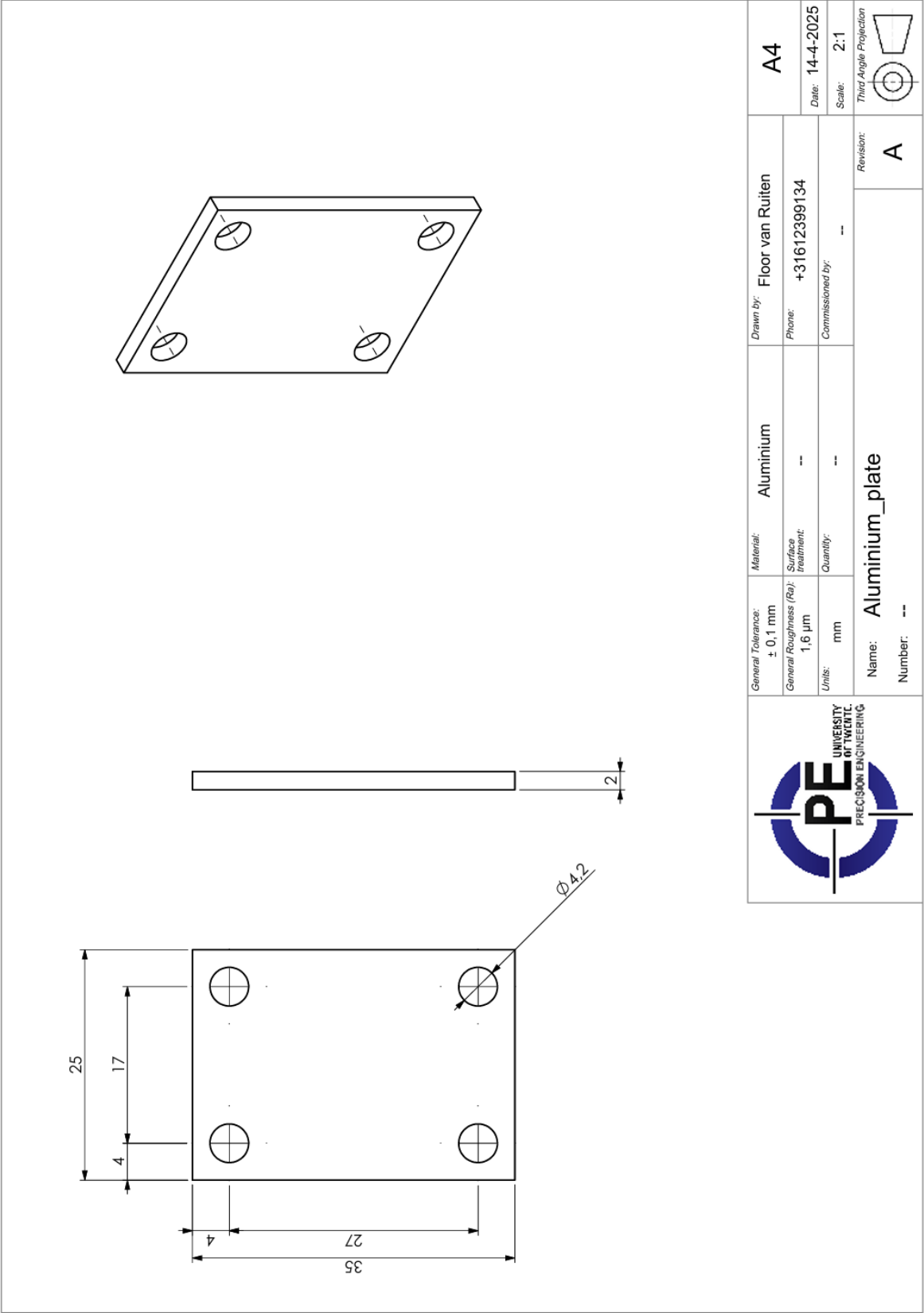
$$\mu = \frac{\sin(\beta)}{1 + \cos(\beta)} \quad (34).$$

The friction coefficient is between 0.203 and 0.204 and is therefore rounded to $\mu = 0.20$.

Appendix M: Technical drawing ball holder



Appendix N: Technical drawing contact plates



		General Tolerance: $\pm 0,1$ mm General Roughness (Ra): 1,6 μm Units: mm	Material: Aluminium Surface treatment: -- Quantity: --	Drawn by: Floor van Ruiten Phone: +31612399134 Commissioned by: --	A4 Date: 14-4-2025 Scale: 2:1 
Name: Aluminium_plate Number: --		Revision: A		Third Angle Projection	

Appendix O: Optimising leaf flexure design

Multiple dimensions are tested in Spacar to find the best performance of the leaf spring mechanism.

Table 20: Dimensions to generate leaf spring data

Thickness leaf spring [mm]	Reinforcement factors [-]	Width [mm]	Length [mm]
0.5, 0.6, 0.7	1	30, 35, 40, 45, 50	50, 60, 70, 80, 90
0.5, 0.6, 0.7	2, 2.5	30, 35, 40, 45, 50	50, 60, 70, 80

Generated data was divided in sagging below and above $0.2\mu m$. Afterwards it was sorted based on the force it takes to reach the desired displacement of 1mm in the x-direction. The results are given in Table 21 which are ranked from best to worst performance. Forces higher than $4.5N$ are not in the table since they are out of the possible range.

Table 21: Performance data generated by Spacar for several dimensions

Thickness [mm]	Thickness reinforced [mm]	Width [mm]	Length [mm]	Maximum force [N]	Minimal z displacement [μm]	Sagging [μm]
0.6	1.20	35	80	2.9713	-6.0875	-0.1988
0.6	1.50	35	80	3.1242	-5.6078	-0.1829
0.6	1.20	40	80	3.3963	-4.2462	-0.1742
0.6	1.50	40	80	3.5710	-3.9114	-0.1605
0.6	1.20	45	80	3.8212	-3.1152	-0.1552
0.5	1.25	50	70	3.8517	-1.8602	-0.1917
0.6	1.50	30	70	3.9934	-5.8943	-0.1844
0.6	1.50	45	80	4.0178	-2.8692	-0.1430
0.7	1.40	30	80	4.0453	-8.0067	-0.1465
0.7	0.70	50	80	4.1422	-2.8768	-0.1820
0.6	1.20	50	80	4.2461	-2.3789	-0.1400
0.7	1.75	30	80	4.2533	-7.3806	-0.1348
0.6	1.20	35	70	4.4318	-4.2197	-0.1723
0.6	1.50	50	80	4.4645	-2.1908	-0.1291
0.5	0.50	30	90	0.6276	-21.8437	-0.9323
0.5	0.50	35	90	0.7350	-14.1815	-0.7976
0.5	0.50	40	90	0.8421	-9.8271	-0.6974
0.5	0.50	30	80	0.8981	-15.6483	-0.8272
0.5	0.50	45	90	0.9490	-7.1607	-0.6199
0.5	0.50	35	80	1.0503	-10.2255	-0.7082
0.5	0.50	50	90	1.0557	-5.4304	-0.5581
0.6	0.60	30	90	1.0950	-18.2355	-0.5389
0.5	0.50	40	80	1.2022	-7.1357	-0.6195
0.6	0.60	35	90	1.2791	-11.8445	-0.4617
0.5	0.50	30	70	1.3448	-10.7879	-0.7209
0.5	0.50	45	80	1.3539	-5.2382	-0.5508
0.6	0.60	40	90	1.4630	-8.2112	-0.4041
0.5	1.00	30	80	1.4710	-11.1515	-0.3985
0.5	0.50	50	80	1.5055	-4.0029	-0.4960
0.5	1.25	30	80	1.5471	-10.2663	-0.3663
0.6	0.60	30	80	1.5612	-13.0605	-0.4788

0.5	0.50	35	70	1.5712	-7.1132	-0.6175
0.6	0.60	45	90	1.6468	-5.9856	-0.3595
0.5	1.00	35	80	1.7173	-7.2808	-0.3419
0.7	0.70	30	90	1.7438	-15.6572	-0.3402
0.5	0.50	40	70	1.7972	-5.0116	-0.5403
0.5	1.25	35	80	1.8060	-6.7021	-0.3144
0.6	0.60	35	80	1.8228	-8.5382	-0.4104
0.6	0.60	50	90	1.8306	-4.5410	-0.3239
0.5	1.00	40	80	1.9636	-5.0754	-0.2995
0.5	0.50	45	70	2.0231	-3.7155	-0.4804
0.7	0.70	35	90	2.0354	-10.1748	-0.2917
0.5	1.25	40	80	2.0648	-4.6713	-0.2756
0.6	0.60	40	80	2.0843	-5.9605	-0.3593
0.5	1.00	30	70	2.1959	-7.6685	-0.3456
0.5	1.00	45	80	2.2097	-3.7213	-0.2667
0.5	0.50	50	70	2.2489	-2.8679	-0.4326
0.5	1.25	30	70	2.3090	-7.0532	-0.3173
0.5	1.25	45	80	2.3236	-3.4243	-0.2455
0.7	0.70	40	90	2.3270	-7.0567	-0.2554
0.6	0.60	30	70	2.3318	-9.0019	-0.4177
0.6	0.60	45	80	2.3456	-4.3771	-0.3196
0.5	1.00	50	80	2.4558	-2.8402	-0.2405
0.7	0.70	30	80	2.4834	-11.2115	-0.3023
0.6	1.20	30	80	2.5462	-9.3175	-0.2315
0.5	1.00	35	70	2.5629	-5.0491	-0.2966
0.5	1.25	50	80	2.5822	-2.6129	-0.2215
0.6	0.60	50	80	2.6069	-3.3460	-0.2879
0.7	0.70	45	90	2.6184	-5.1462	-0.2273
0.6	1.50	30	80	2.6773	-8.5834	-0.2130
0.5	1.25	35	70	2.6948	-4.6425	-0.2723
0.6	0.60	35	70	2.7218	-5.9379	-0.3580
0.7	0.70	35	80	2.8982	-7.3326	-0.2592
0.7	0.70	50	90	2.9098	-3.9057	-0.2049
0.5	1.00	40	70	2.9298	-3.5515	-0.2598
0.5	1.25	40	70	3.0805	-3.2644	-0.2387
0.6	0.60	40	70	3.1115	-4.1849	-0.3134
0.5	1.00	45	70	3.2967	-2.6285	-0.2313
0.7	0.70	40	80	3.3130	-5.1209	-0.2270
0.5	1.25	45	70	3.4662	-2.4151	-0.2126
0.6	0.60	45	70	3.5012	-3.1036	-0.2788
0.5	1.00	50	70	3.6634	-2.0254	-0.2085
0.7	0.70	30	70	3.7066	-7.7257	-0.2637
0.7	0.70	45	80	3.7276	-3.7619	-0.2020
0.6	1.20	30	70	3.7982	-6.4049	-0.2008
0.6	0.60	50	70	3.8908	-2.3964	-0.2511
0.7	0.70	35	70	4.3251	-5.0981	-0.2261

Appendix P: Checking displacements and stresses leaf spring design

Simulations are performed in SolidWorks to check if the leaf spring mechanism performs as expected. An material of the aluminium 6xxx-series is used which resembles the material to-be used closely. Table 22 shows the material properties.

Table 22: Properties of aluminium 6061 generated by SolidWorks and aluminium 6082 retrieved from Iron Boar Labs Ltd. [43]

Aluminium	Modulus of Elasticity [GPa]	Poisson's ratio [-]	Shear modulus [GPa]	Mass density [g/cm^3]	Tensile strength [MPa]	Yield strength [MPa]
6061	69	0.33	26	2.7	124	55
6082	69	0.33	26	2.7	330	270

A static analysis is performed in SolidWorks to simulate the deformations of the chuck based on the applied forces. The bottom of the holes in the middle of the triangle are fixated to model the bolts (Figure 52).

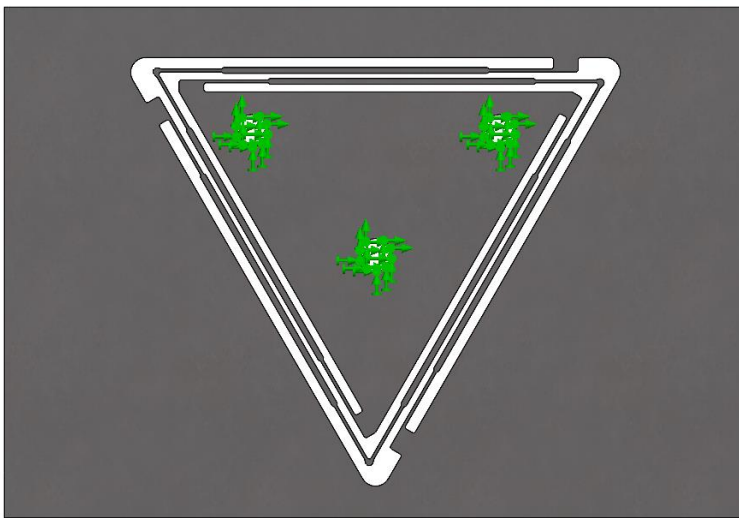


Figure 52: Fixated points chuck

The forces will be applied with ropes, which will be attached to the chuck with screw eyes. The forces for the simulations are applied at the locations of the screw eyes (Figure 53).

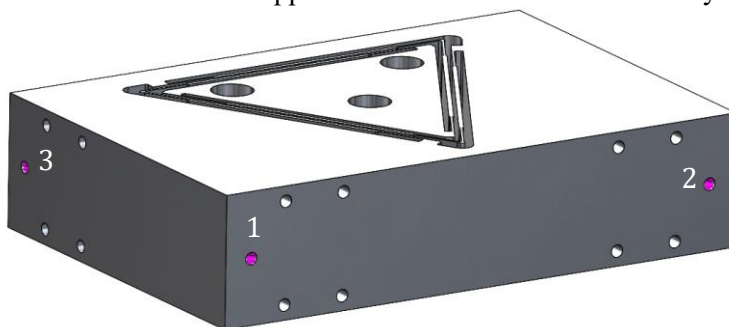


Figure 53: Force locations chuck, labelled the same way as in the model

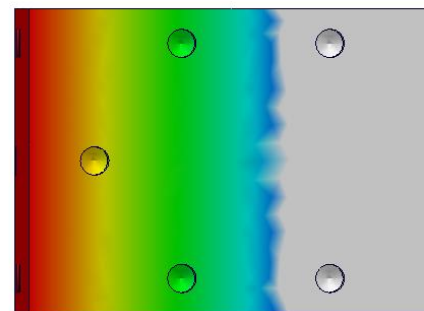


Figure 54: Vertical displacements of the chuck at the side for $F_{a,1} = 0.75N$

The forces required to displace the contact points of the chuck by 1mm are found by means of trial and error. The contact points are taken halfway the holes the contact plates (Figure 54). For point 1 and 2 the displacement of 1mm is taken in the y-direction of the model which corresponds with the negative z-direction of Solidworks. For point 3 this displacement is taken in the x-direction. The displacements are shown in Figure 55 till 57.

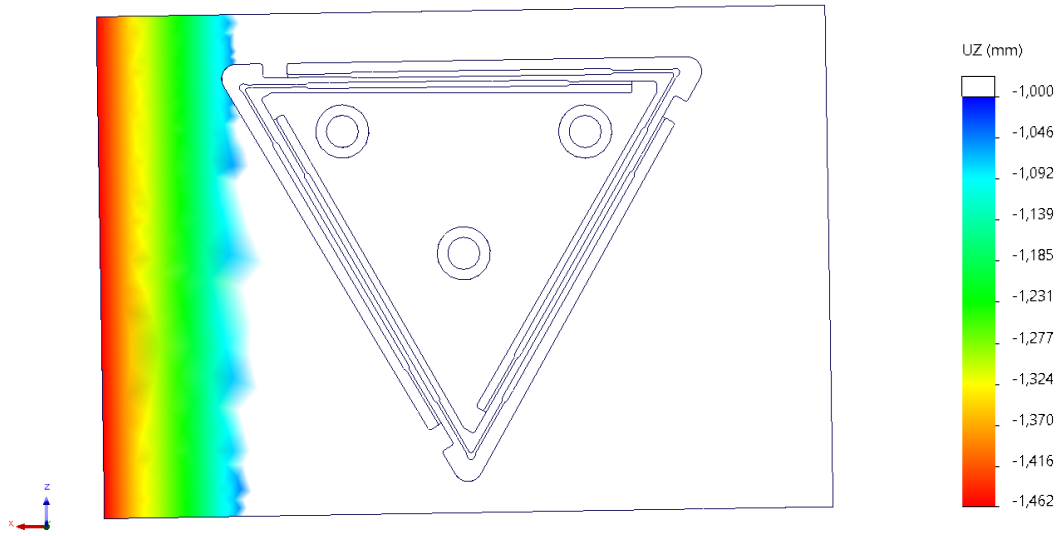


Figure 55: Vertical displacements of the chuck for $F_{a,1} = 0.75N$

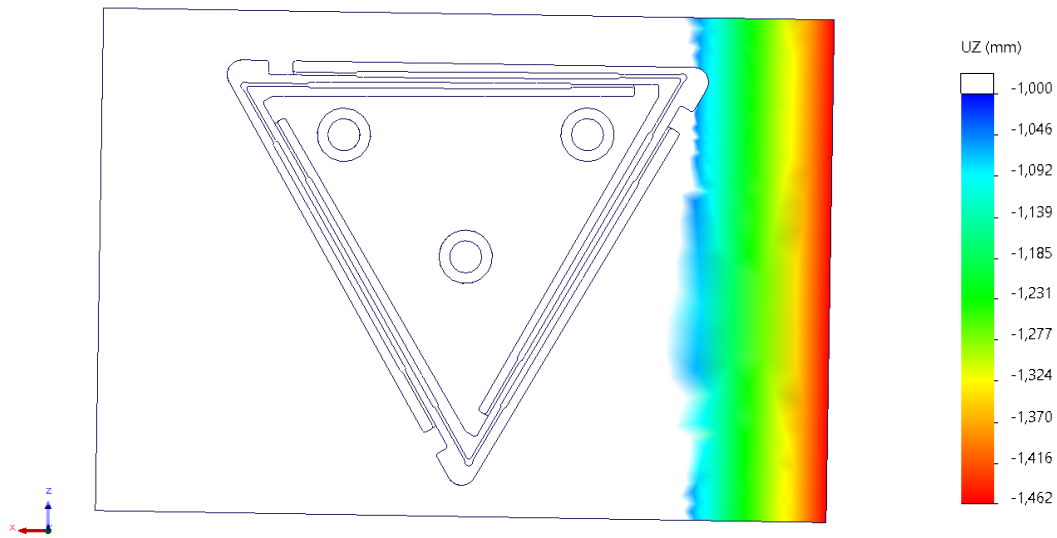


Figure 56: Vertical displacements of the chuck for $F_{a,2} = 0.75N$

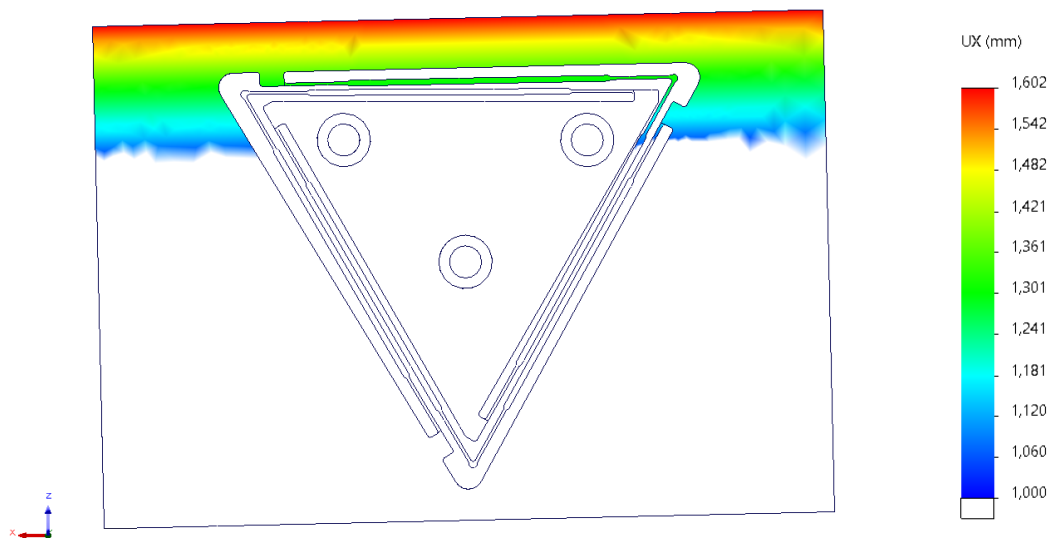


Figure 57: Horizontal displacements of the chuck for $F_{a,3} = 2.2N$

Putting all those maximum forces together, does make point 1 and 3 move 1mm, but not point 2 due to the rotations. More trial and error shows all displacements are at least 1mm for forces of $F_{a,1} = 1.0N$, $F_{a,2} = 2.8N$ and $F_{a,3} = 3.5N$. The displacements are shown in Figures 58 till 60.

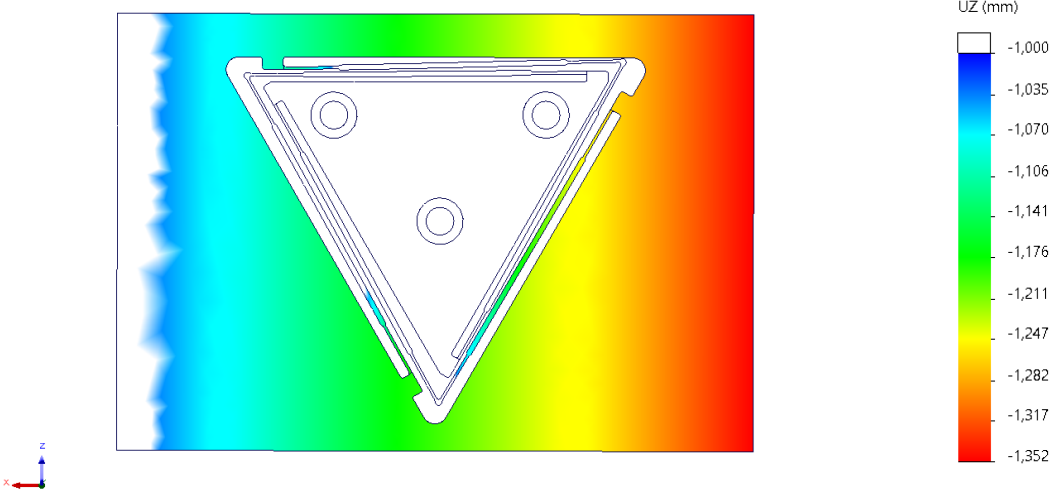


Figure 58: Vertical displacements of the chuck for $F_{a,1} = 1.0N$, $F_{a,2} = 2.8N$ and $F_{a,3} = 3.5N$

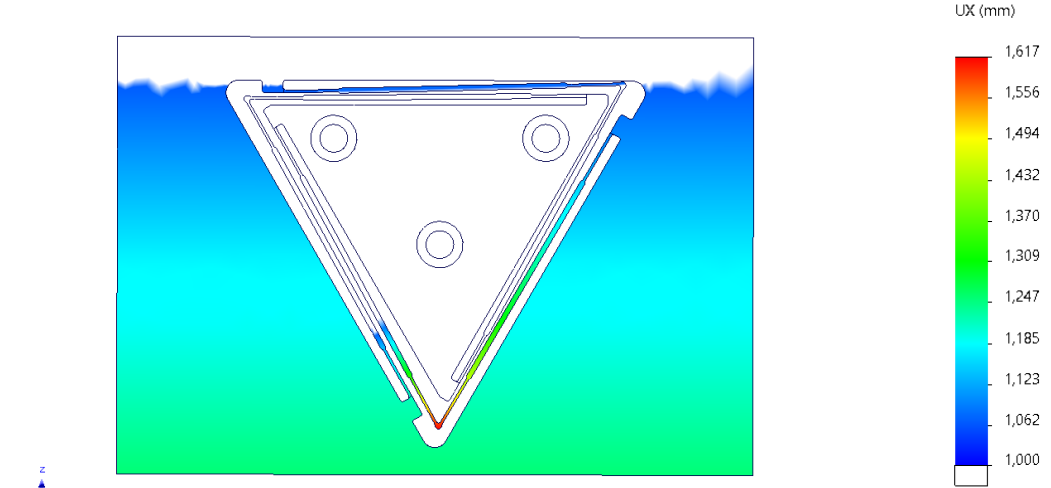


Figure 59: Horizontal displacements of the chuck for $F_{a,1} = 1.0N$, $F_{a,2} = 2.8N$ and $F_{a,3} = 3.5N$

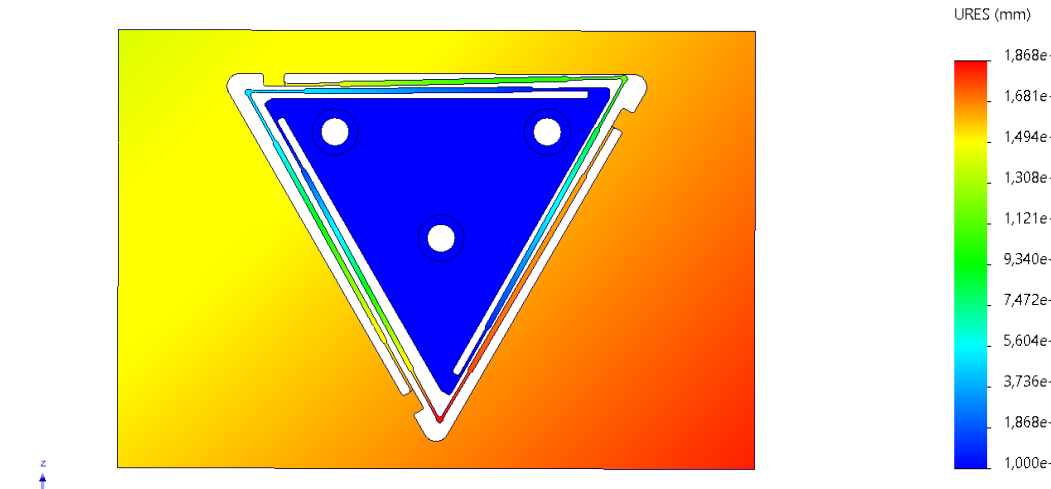


Figure 60: Total displacements of the chuck for $F_{a,1} = 1.0N$, $F_{a,2} = 2.8N$ and $F_{a,3} = 3.5N$

Figure 61 shows the Von Mises stresses for this final case. The yield strength of aluminium 6082, which will be used for manufacturing, is 270MPa (Table 22). It is clear the Von Mises stress stays well within the limit of the material for these displacements. The leaf spring mechanism should not fail for the test set-up.

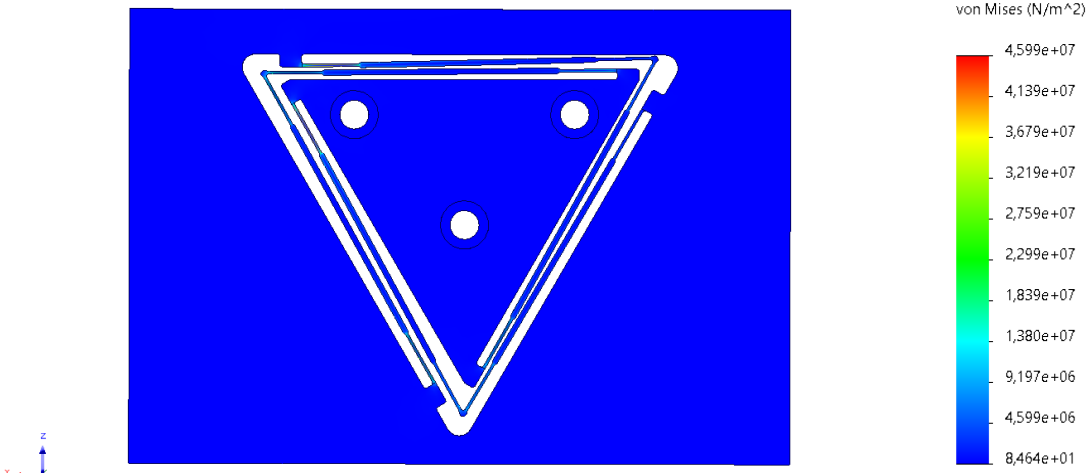


Figure 61: Von Mises stress of the chuck for $F_{a,1} = 1.0\text{N}$, $F_{a,2} = 2.8\text{N}$ and $F_{a,3} = 3.5\text{N}$

Appendix Q: Calibration sheets capacitive sensors

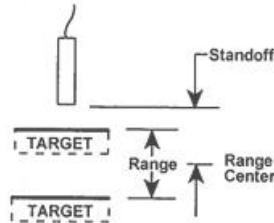


Calibration Report for IBS

Order ID: 54117
 Customer ID: 1066
 Calibration Date: 6/3/2009
 Calibration Due Date: 6/3/2010
 Calibration Number: 13005
 Calibration Type=Single-Ended

CALIBRATION REPORT

System Components
 Probe Model: C6-D
 Probe Serial: 090097-04
 Driver Model: CPL290
 Driver Serial: 080904-10
 Channel: 8
 Sensitivity Switch: LO



See definition of terms on the back of this sheet

Calibration Parameters
 Range: 500 μm
 Standoff (range center) 350 μm
 Output Voltage: 10 to -10 VDC
 Output Sensitivity: 0.040 $\text{V}/\mu\text{m}$
 Target: 100 - flat target
 Bandwidth (-3dB): 15000 Hz

Peak to Peak Resolution: 69.08 nm (Spec: 180 nm) Linearity Error: 0.03%
 RMS Resolution: 7.99 nm (Spec: 18 nm) Error Band: 0.03% (Spec: $\pm 1\%$)
 Bandwidth: (-3dB): 14000 Hz * denotes out of spec condition

Gap to Target μm	Gap to Standoff μm	Output Volts	Output converted to μm	Error μm
100.00	-250.00	9.995	-249.865	0.135
131.25	-218.75	8.747	-218.682	0.069
162.50	-187.50	7.498	-187.462	0.036
193.75	-156.25	6.248	-156.202	0.046
225.00	-125.00	4.997	-124.915	0.085
256.25	-93.75	3.748	-93.691	0.059
287.50	-62.50	2.499	-62.464	0.034
318.75	-31.25	1.249	-31.219	0.028
350.00	0.0	0.000	0.000	0.000
381.25	31.25	-1.248	31.204	-0.046
412.50	62.50	-2.500	62.504	0.002
443.75	93.75	-3.753	93.835	0.084
475.00	125.00	-5.001	125.017	0.014
506.25	156.25	-6.243	156.084	-0.168
537.50	187.50	-7.500	187.493	-0.009
568.75	218.75	-8.756	218.890	0.140
600.00	250.01	-10.001	250.025	0.020

Combined uncertainty of calibration: 12.7 nm plus 12.9 $\mu\text{m}/\text{m}$ of range
 Environmental Conditions: Temperature: 24.5 $^{\circ}\text{C}$ Pressure: 766.7 mmHg Humidity: 15.3% RH
 Environmental Conditions Measurement IDs: Thermometer ID: 1 Barometer ID: 3 Hydrometer ID: 2
 Calibration Equipment IDs: DSA Module: 0 Mechanical Calibrator ID: 1
 Calibration Procedure ID: T016-0340 Calibration Spec ID: 5415

This certificate conforms to ISO 10012 Section 7.1.4
 All Lion Precision calibrations are NIST traceable.
 Detailed traceability information available upon request.

Bipolar Calibration Report rev02
 Lion Precision 563 Shoreview Park Road Shoreview, MN 55128 USA
 Phone: (651) 484-6544 • Fax: (651) 484-6824 • support@lionprecision.com • www.lionprecision.com

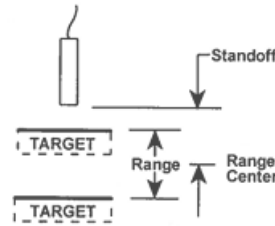
Technician: Alex Pongmany

Calibration Report for IBS

Order ID: 54117
 Customer ID: 1066
 Calibration Date: 6/3/2009
 Calibration Due Date: 6/3/2010
 Calibration Number: 12999
 Calibration Type=Single-Ended

CALIBRATION REPORT

System Components
 Probe Model: C6-D
 Probe Serial: 090391-02
 Driver Model: CPL290
 Driver Serial: 081706-06
 Channel: 6
 Sensitivity Switch: LO



See definition of terms on the back of this sheet

Calibration Parameters
 Range: 500 μm
 Standoff (range center) 350 μm
 Output Voltage: 10 to -10 VDC
 Output Sensitivity: 0.040 V/ μm
 Target: 100 - flat target
 Bandwidth (-3dB): 15000 Hz

Peak to Peak Resolution: 68.74 nm (Spec: 180 nm) Linearity Error: 0.03%
 RMS Resolution: 7.94 nm (Spec: 18 nm) Error Band: 0.04% (Spec: $\pm 1\%$)
 Bandwidth: (-3dB): 14000 Hz * denotes out of spec condition

Gap to Target	Gap to Standoff	Output	Output converted to	Error
μm	μm	Volts	μm	μm
100.00	-250.00	9.997	-249.925	0.074
131.25	-218.75	8.752	-218.800	-0.047
162.50	-187.50	7.503	-187.566	-0.064
193.75	-156.25	6.251	-156.281	-0.032
225.00	-125.00	4.998	-124.959	0.040
256.25	-93.75	3.749	-93.725	0.025
287.50	-62.50	2.501	-62.529	-0.029
318.75	-31.25	1.251	-31.273	-0.019
350.00	0.0	0.000	0.000	0.000
381.25	31.25	-1.250	31.250	0.000
412.50	62.50	-2.501	62.530	0.029
443.75	93.75	-3.754	93.853	0.102
475.00	124.99	-5.002	125.044	0.049
506.25	156.25	-6.246	156.160	-0.087
537.50	187.50	-7.502	187.549	0.049
568.75	218.75	-8.757	218.933	0.184
600.00	250.00	-10.000	250.006	0.005

Combined uncertainty of calibration: 12.7 nm plus 12.9 $\mu\text{m}/\text{m}$ of range
 Environmental Conditions: Temperature: 24.4 $^{\circ}\text{C}$ Pressure: 767.5 mmHg Humidity: 18.4% RH
 Environmental Conditions Measurement IDs: Thermometer ID: 1 Barometer ID: 3 Hydrometer ID: 2
 Calibration Equipment IDs: DSA Module: 0 Mechanical Calibrator ID: 1
 Calibration Procedure ID: T016-0340 Calibration Spec ID: 5415

This certificate conforms to ISO 10012 Section 7.1.4
 All Lion Precision calibrations are NIST traceable.
 Detailed traceability information available upon request.

Bipolar Calibration Report rev02
 Lion Precision 563 Shoreview Park Road Shoreview, MN 55126 USA
 Phone: (651) 484-6544 • Fax: (651) 484-6824 • support@lionprecision.com • www.lionprecision.com

Technician: Alex Pongmany

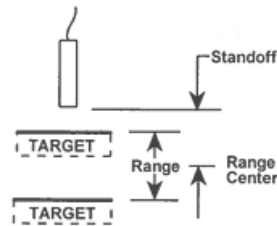
Calibration Report for IBS

Order ID: 54117
 Customer ID: 1066
 Calibration Date: 6/3/2009
 Calibration Due Date: 6/3/2010
 Calibration Number: 13002
 Calibration Type=Single-Ended

CALIBRATION REPORT

System Components

Probe Model: C6-D
 Probe Serial: 090391-03
 Driver Model: CPL290
 Driver Serial: 081706-07
 Channel: 7
 Sensitivity Switch: LO



See definition of terms on the back of this sheet

Calibration Parameters

Range: 500 μm
 Standoff (range center) 350 μm
 Output Voltage: 10 to -10 VDC
 Output Sensitivity: 0.040 V/ μm
 Target: 100 - flat target
 Bandwidth (-3dB): 15000 Hz

Peak to Peak Resolution: 72.74 nm (Spec: 180 nm) Linearity Error: 0.04%
 RMS Resolution: 8.40 nm (Spec: 18 nm) Error Band: 0.04% (Spec: $\pm 1\%$)
 Bandwidth: (-3dB): 14000 Hz * denotes out of spec condition

Gap to Target	Gap to Standoff	Output	Output converted to	Error
μm	μm	Volts	μm	μm
100.00	-250.00	9.999	-249.981	0.020
131.25	-218.75	8.751	-218.779	-0.026
162.50	-187.50	7.501	-187.533	-0.034
193.75	-156.25	6.250	-156.244	0.008
225.00	-125.00	4.999	-124.976	0.023
256.25	-93.75	3.751	-93.768	-0.017
287.50	-62.50	2.501	-62.533	-0.035
318.75	-31.25	1.251	-31.267	-0.017
350.00	0.0	0.000	0.000	0.000
381.25	31.25	-1.249	31.227	-0.023
412.50	62.50	-2.501	62.513	0.014
443.75	93.75	-3.753	93.819	0.068
475.00	125.00	-5.000	124.989	-0.012
506.25	156.25	-6.244	156.088	-0.162
537.50	187.50	-7.501	187.535	0.035
568.75	218.75	-8.757	218.931	0.183
600.00	250.00	-10.001	250.024	0.022

Combined uncertainty of calibration: 12.7 nm plus 12.9 $\mu\text{m}/\text{m}$ of range
 Environmental Conditions: Temperature: 24.7 °C Pressure: 767.1 mmHg Humidity: 16% RH
 Environmental Conditions Measurement IDs: Thermometer ID: 1 Barometer ID: 3 Hydrometer ID: 2
 Calibration Equipment IDs: DSA Module: 0 Mechanical Calibrator ID: 1
 Calibration Procedure ID: T016-0340 Calibration Spec ID: 5415

This certificate conforms to ISO 10012 Section 7.1.4
 All Lion Precision calibrations are NIST traceable.
 Detailed traceability information available upon request.

Bipolar Calibration Report rev02
 Lion Precision 563 Shoreview Park Road Shoreview, MN 55126 USA
 Phone: (651) 484-6544 • Fax: (651) 484-6824 • support@lionprecision.com • www.lionprecision.com

Technician: Alex Pongmany

Appendix R: Loadcell calibrations

The loadcells are one-by-one horizontally clamped to the desk after which several masses are placed on top of them (Table 23). The voltage values are read out in Simulink Realtime with the Speedgoat and converted to mass values. To do this, the difference between placing no mass on the loadcell and placing the maximum mass of 5000g on the loadcell are used. After calibration the sensors all masses are tested again for validation (Figure 62).

Table 23: Applied masses for calibration load cells

Mass [g]	Amount
100	1
200	2
300	1
500	1
1000	2
2000	1
5000	1

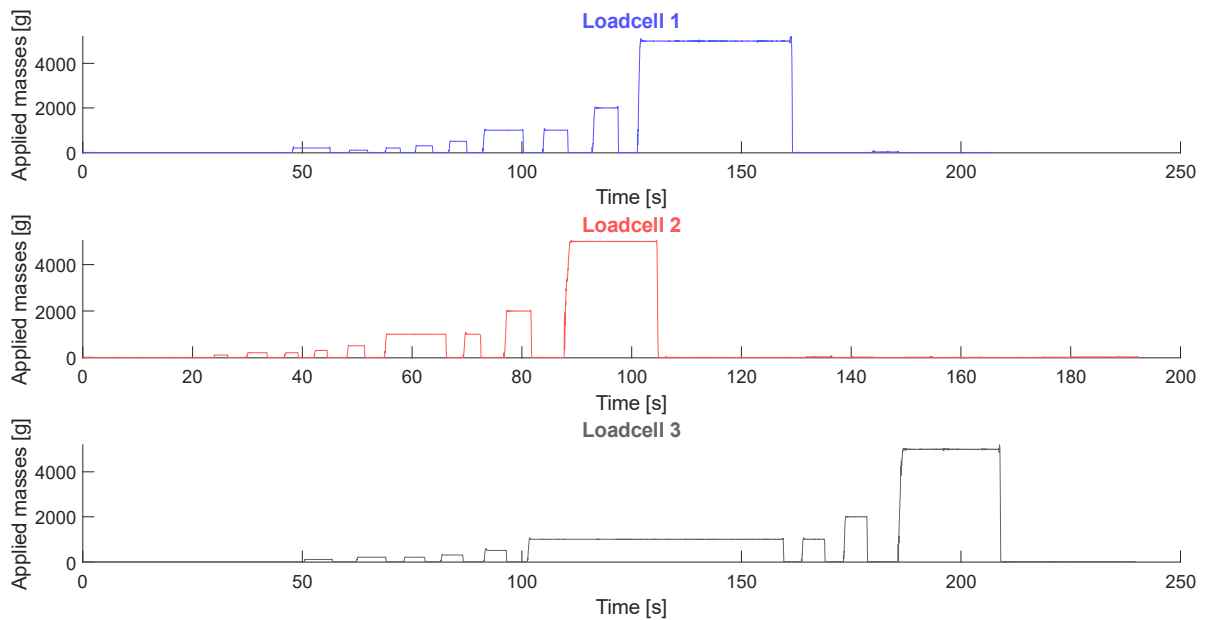
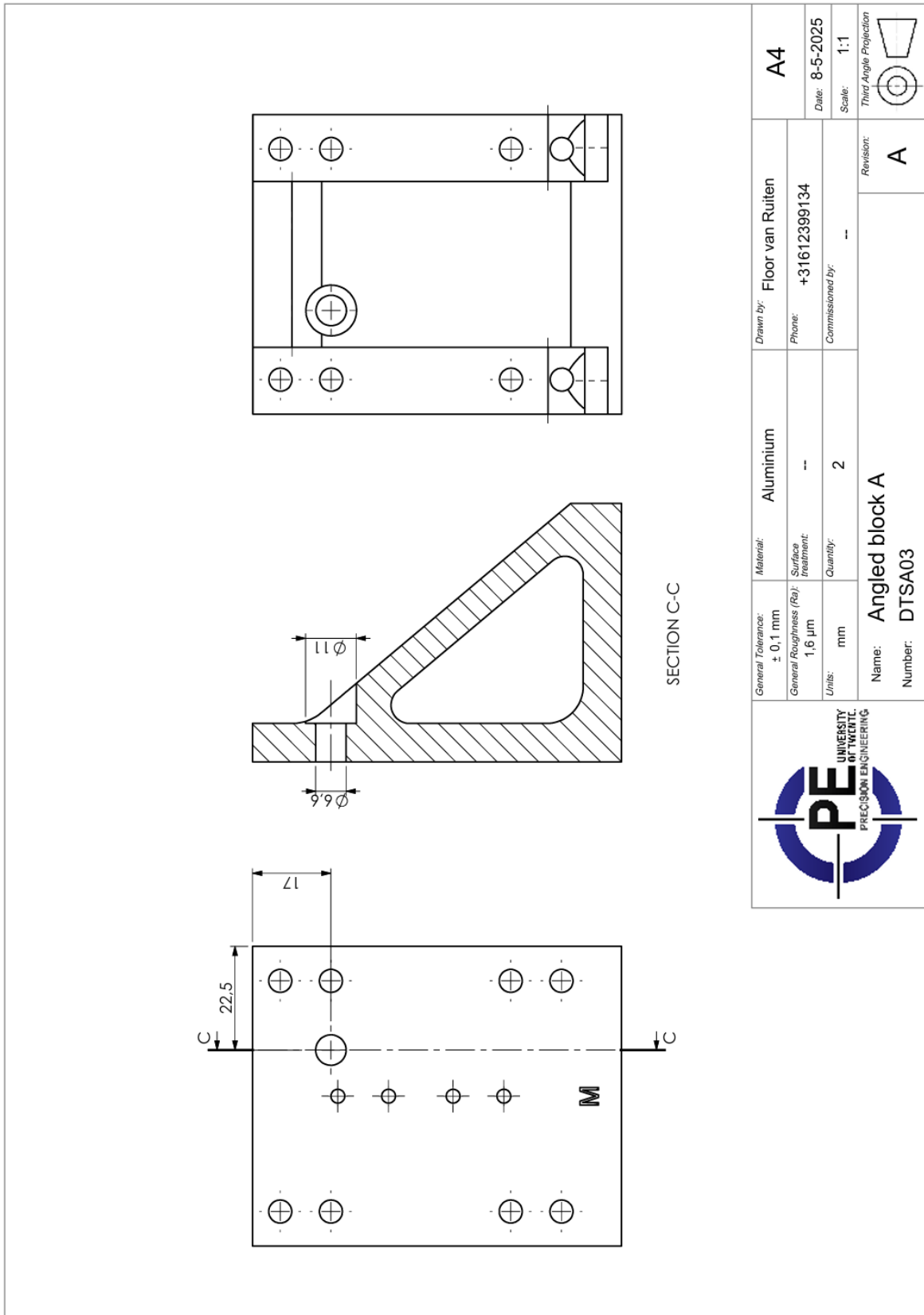


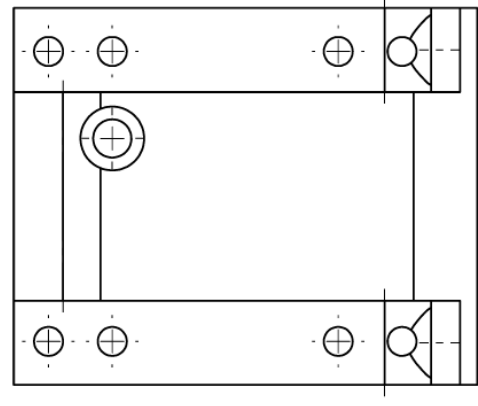
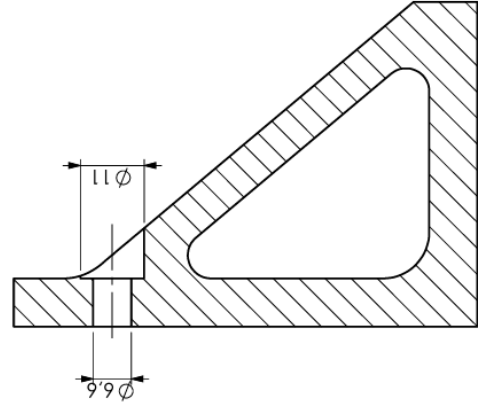
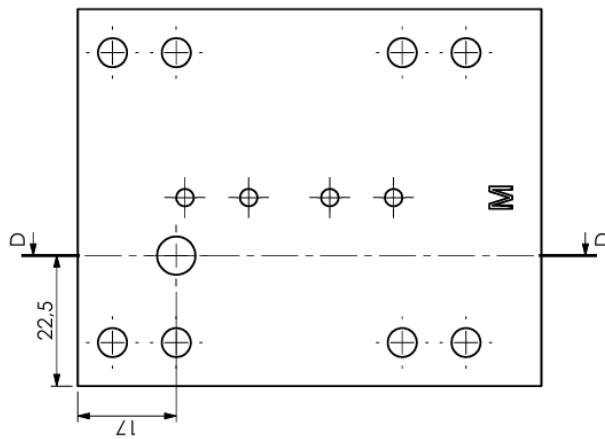
Figure 62: Applied masses to validate loadcell calibrations

The masses are converted into forces with the gravitational constant. When placing the loadcells vertical in the test set-up, a new offset value is determined. This way applying no force equals 0N for all sensors.

Appendix S: Extra holes angled blocks



		General Tolerance: ± 0,1 mm	Material: Aluminium	Drawn by: Floor van Ruiten	A4
		General Roughness (Ra): 1,6 µm	Surface treatment: --	Phone: +31612399134	
Units: mm	Quantity: 2	Commissioned by: --		Date: 8-5-2025	Scale: 1:1 
Name: Angled block A		Revision: A		Number: D TSA03	



SECTION D-D



General Tolerance: ± 0,1 mm	Material: Aluminium	Drawn by: Floor van Ruiten	A4
General Roughness (Ra): 1,6 µm	Surface treatment: --	Phone: +31612399134	Date: 8-5-2025
Units: mm	Quantity: 1	Commissioned by: --	Scale: 1:1
Name: Angled block B		Revision: A	
Number: DTSA03		Third Angle Projection	

Appendix T: Bill of materials test set-up

Table 24 presents the parts for the test set-up. The hardware and software needed for the sensors are presented in Table 25.

Table 24: Bill of Materials test set-up

Item nr	Part	Description	Qty	Total qty	Material	Supplier/ Manufacturer	Costs
1	MBH4545/M	Bottom plate	1	1	Aluminium	Thorlabs	€390,69
2		Chuck assembly	1				-
2.1		Leaf springs	1	1	AW 6082	TCO university of Twente	€850,-
2.2	BA2S5/M	Spacer plate	2	2	Aluminium	Thorlabs	€52,24
2.3	DIN 988 6x12x1	Shim rings	6	6		Fabory	Ordered for inventory
2.5	DIN 912 M6x60	Bolts bottom	3	3		WH120	Inventory
2.6		Aluminium plates	3	3	Aluminium	Cube university of Twente	Not booked
2.7	DIN 912 M4x10	Bolts aluminium plates	12	12		WH120	Inventory
2.8	11843018	Screw eye	3	3	Carbon steel	Eriks	€16,-
2.9	Araldite 2021-1	Glue	1	1	Methacrylate	Rs online	€24,18 (together with 3.4)
3		Ball holder assembly	3				-
3.1		Ball holder	1	3	Aluminium	Cube University of Twente	Material available at WH120, not booked
3.2	66813.010.000	Ball	1	3	Chroomstaal HRC 60-66	Fabory	€6,-
3.3	DIN 912 M6x50	Bolts bottom	2	6		Fabory	Ordered for inventory
3.4	Araldite 2021-1	Glue	1	1	Methacrylate	Rs online	€24,18 (together with 2.9)
4		Sensor holder assembly	3				-
4.1	VH1/M	Sensor V clamp	1	3		Thorlabs	€119,34
4.2	MSC2	Post clamp	1	3		Thorlabs	€50,07
4.3	TRP20/M	Post	1	3		Thorlabs	€59,34
4.4	C6-D	Capacitive sensor	1	3		Lion precision	Available at WH120

4.5	DIN 912 M6x25	Bolt bottom	1	3		WH120	Inventory
5		Force application a/b	3				-
5.1	DTS25/M	Linear stage	1	3	Aluminium	Thorlabs	€596,07
5.2	DTSA01	Spacer plate	1	3	Aluminium	Thorlabs	€99,63
5.3	DIN 912 M6x25	Bolts bottom	4	12		WH120	Inventory
5.4	BA2S8/M	Thick block	1	3	Aluminium	Thorlabs	€143,34
5.5	DTSA03/M	Angled block	1	3	Aluminium	Thorlabs+holes added in WH120	€241,38
5.6	DIN 912 M6x60	Bolts bracket- linear stage	4	12		Fabory	Ordered for inventory
5.7	268-9142	Loadcell	1	3		Rs online	€220,74
5.8	DIN 912 M6x40	Bolts loadcell	2	6		WH120	Inventory
5.9	Nut M6	Nuts loadcell	2	6		WH120	Inventory
6		Rope	1	3	Dyneema	Amazon	€14,99

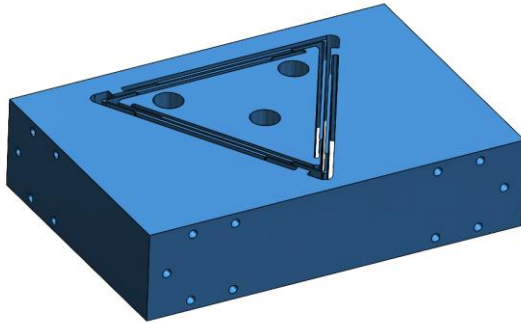
Table 25: Hardware and software loadcells and capacitive sensors

Part	Description	Purpose	Qty
Simulink real-time Matlab 2023b	Simulink	Conversion of analog to digital data and visualising test data	1
Baseline Education real-time target machine, Serial number: 10055	Speedgoat with IO 191 I/O module	Gathering analog data	1
Terminal Board: 17-Pin M12	Spring loaded terminal board	Connecting signals to speedgoat	1
Power adapter 60W	Power source analog amplifiers	Applying necessary power	1
Honeywell Sensotec DV 10 Transduces Amplifier	Analog amplifier	Amplification of the loadcell signals	3
CPL290	Capacitive sensor output	Calibration and amplification of capacitive sensor signals	1

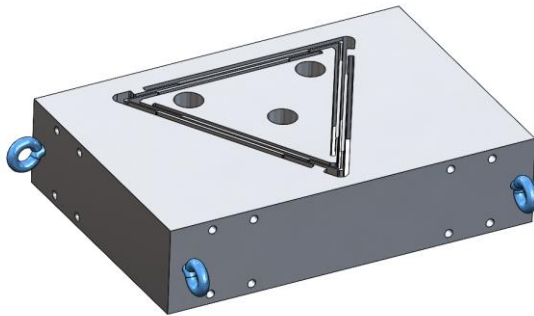
Appendix U: Assembly plan test set-up

Section 1: Assembling the test set-up

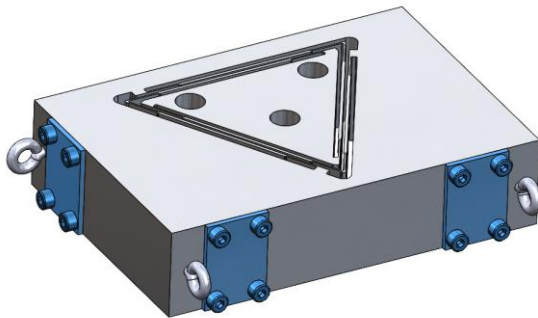
1. Start out with the leaf springs and clamp it while keeping the side holes clear.



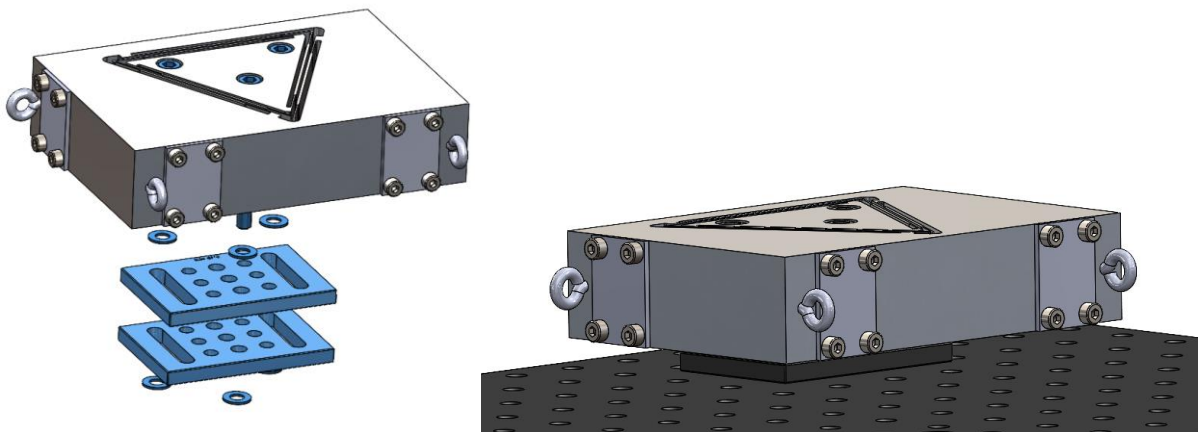
2. Insert the screw eyes to the chuck (with glue).



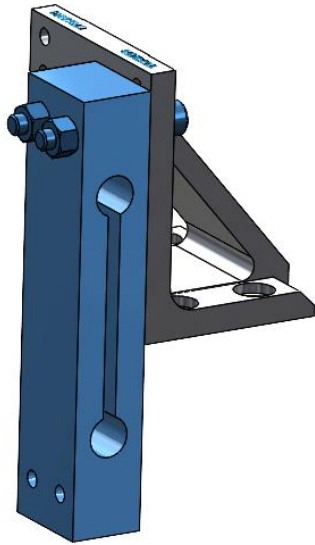
3. Secure the small aluminium plates to the chuck.



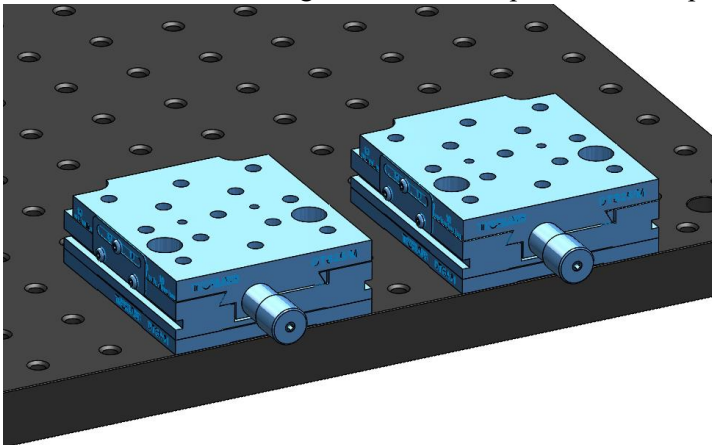
4. Secure the entire chuck-leaf spring mechanism to the bottom plate. Use shim rings and heightener plates in between. Make sure the triangle is hold in place while doing this and the outer side of the chuck is clear (to avoid loading the leaf springs).



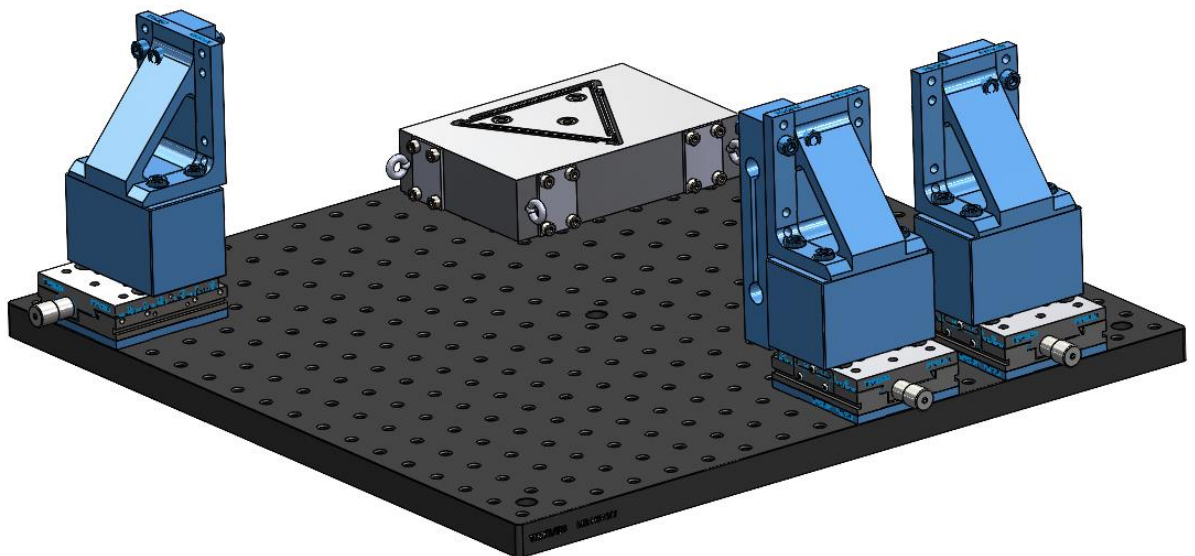
- Secure the three loadcells to angled brackets. Watch out that one part is mirrored. The cables coming out of the loadcells should be be on the topside.



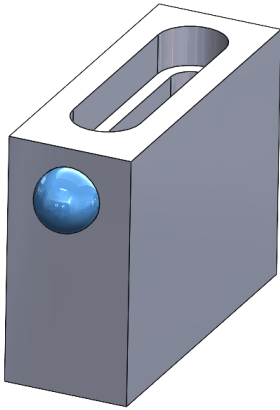
- Screw the three linear stages to the bottom plate with the spacer plates in between.



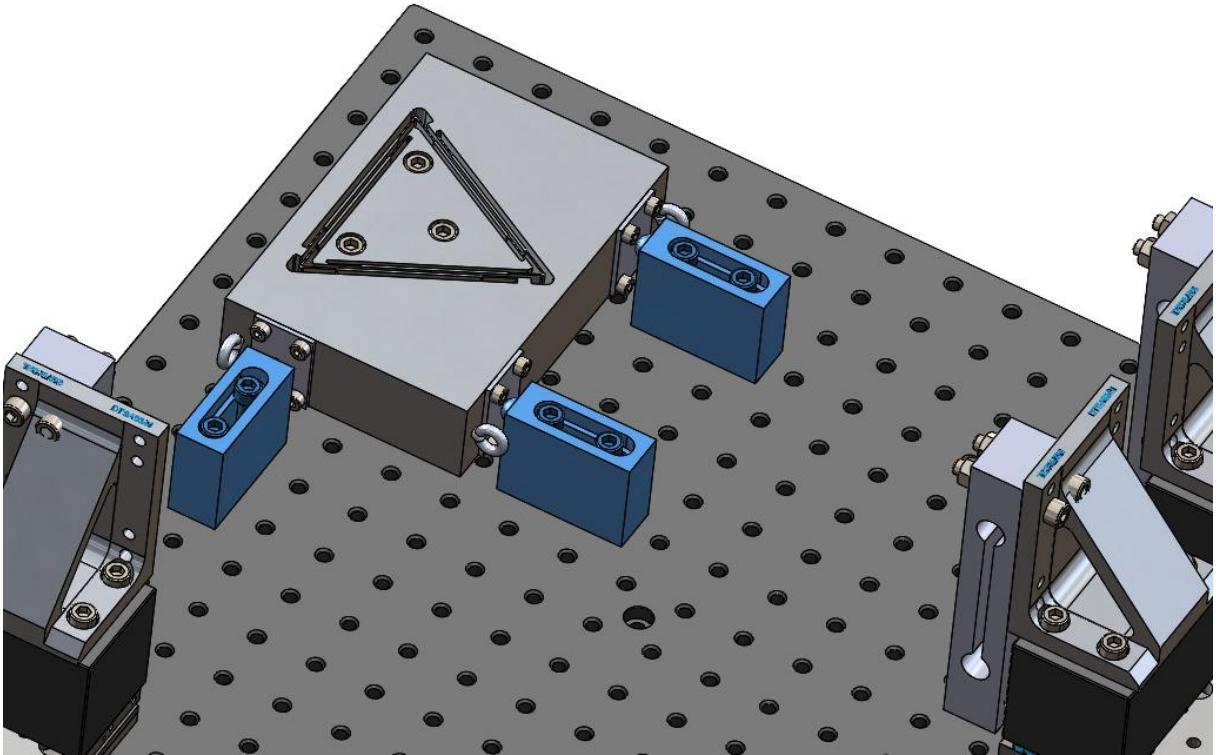
- Secure the loadcells on the linear stages. Use the spacer blocks in between. Watch out that one part is mirrored.



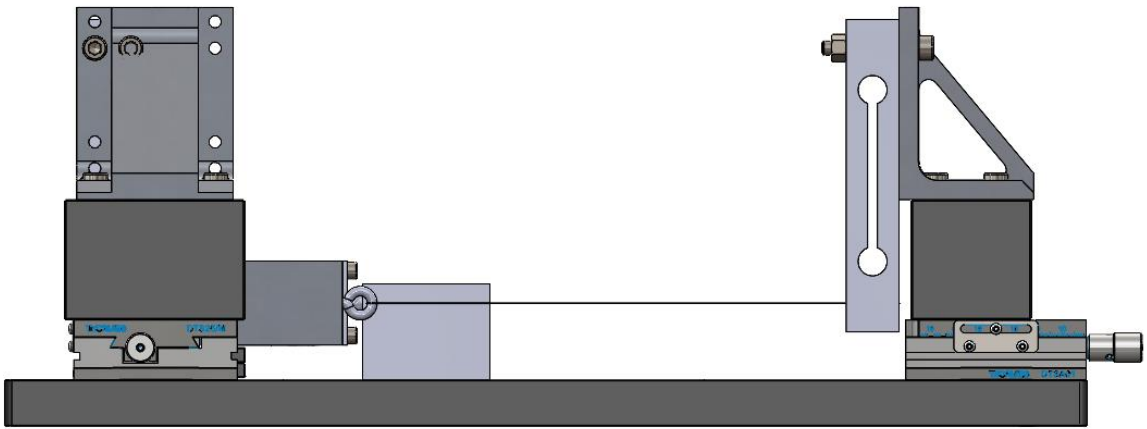
8. Glue three balls into holders (see section 2).



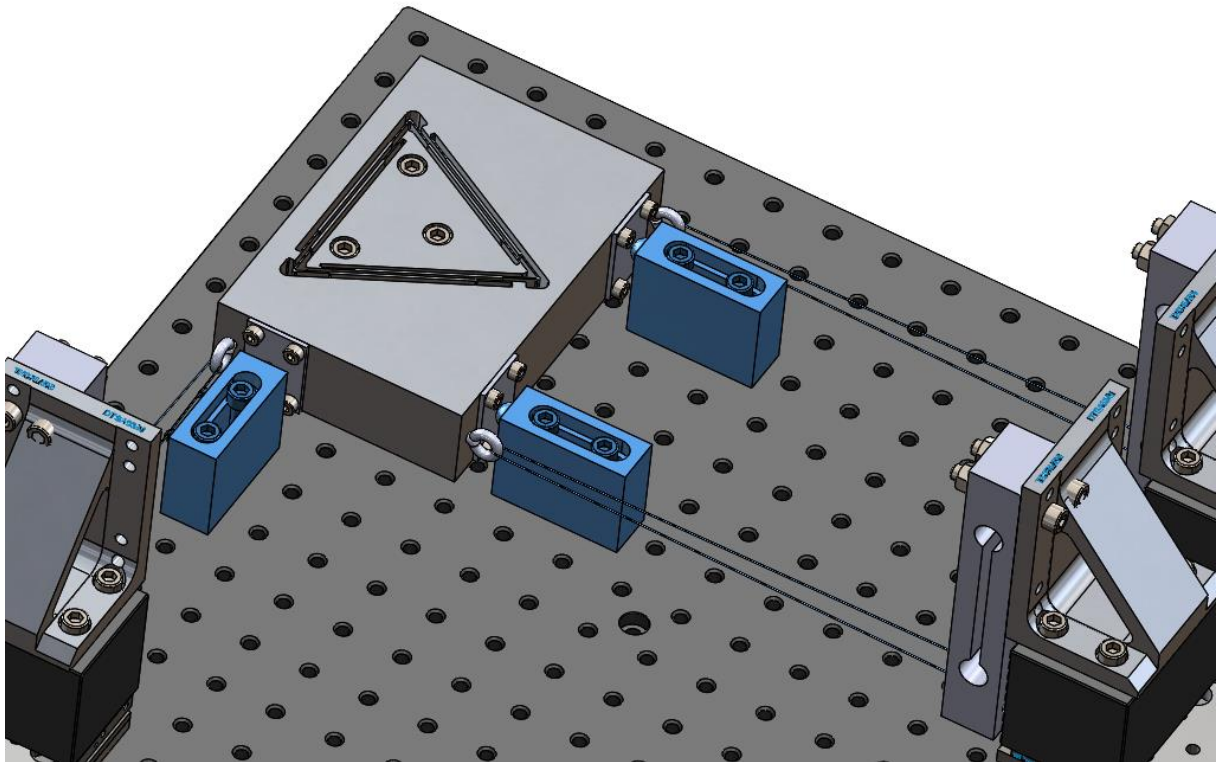
9. Secure the holders at the bottom plate such that the distance between the balls and the plates is approximately 0.5mm . Use for example a feeler gauge to achieve this while keeping the chuck in place.



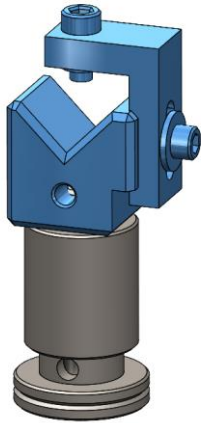
10. Tie the loadcells to screw eyes. Move the linear stage to get extra space to do this and make sure the outer side of the chuck goes against the balls while tying (to avoid loading the leaf springs). Release the ropes till the chuck is in it's neutral position.



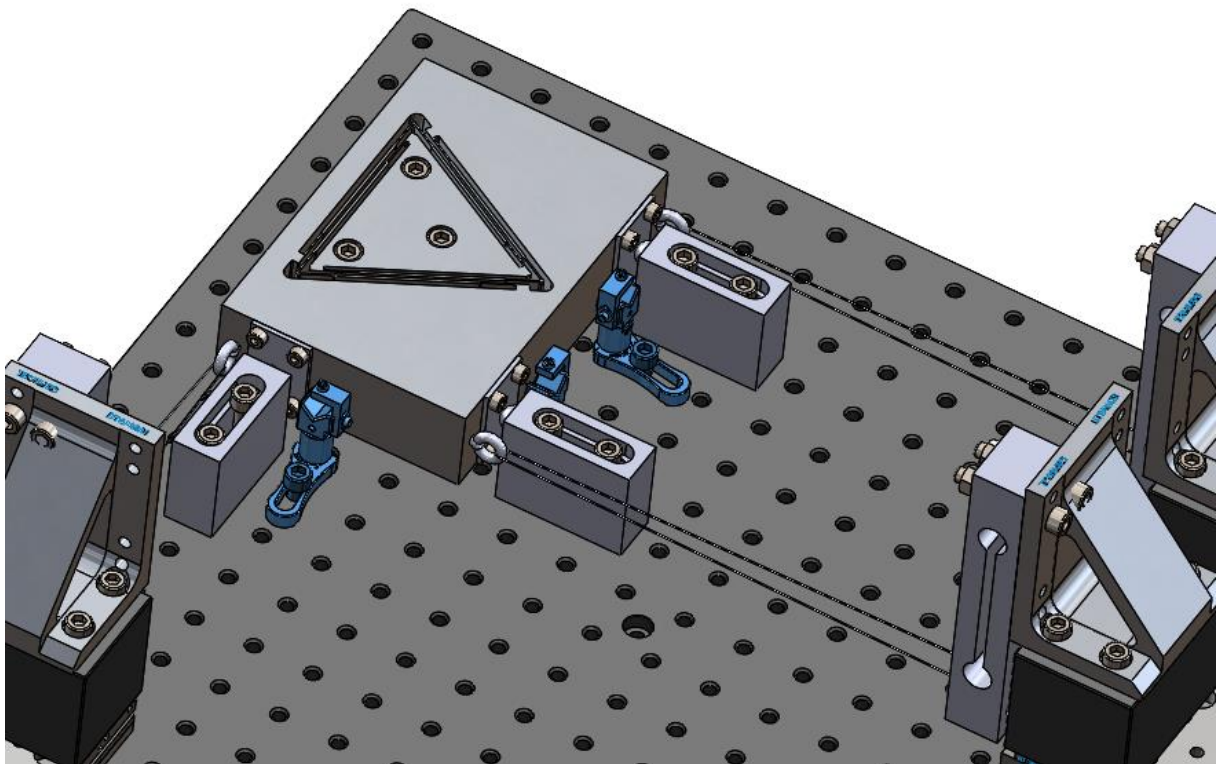
11. Resecure the holders at the bottom plate such that the distance between the balls and the plates is approximately 0.5mm . Use a feeler gauge to achieve this while the chuck is being kept in place by the ropes.



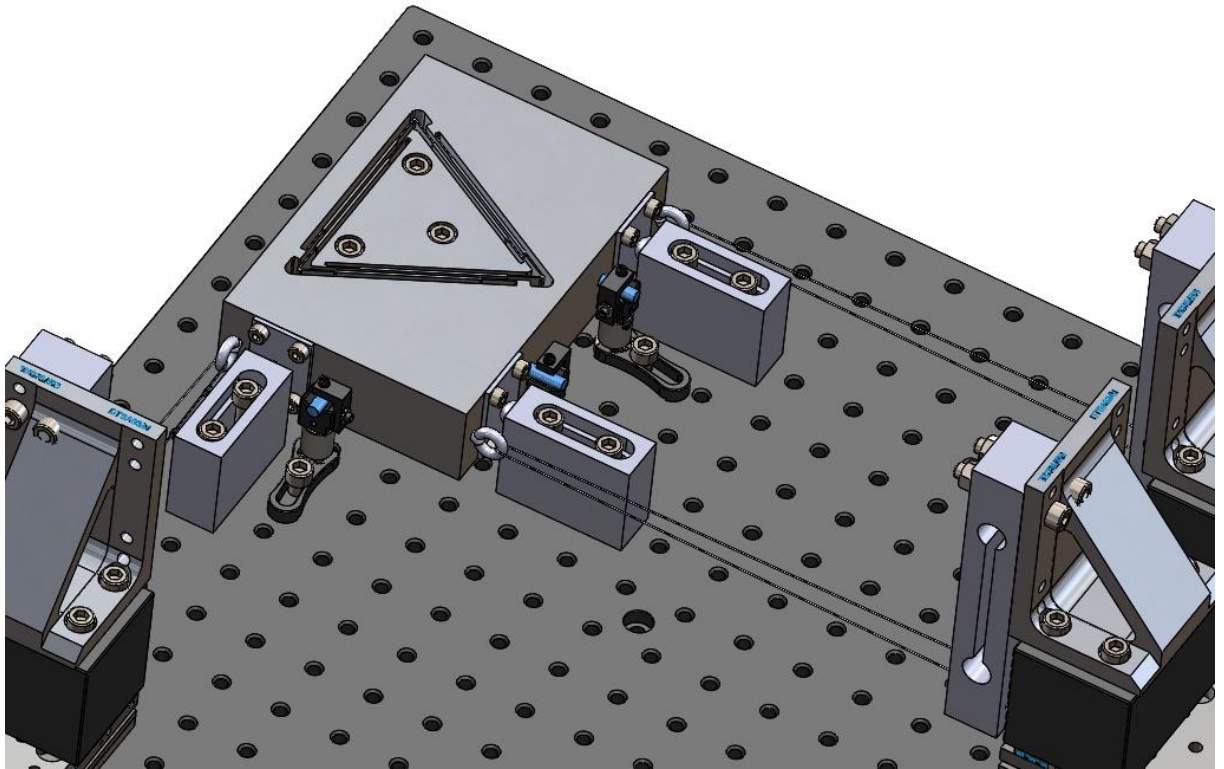
12. Screw three V blocks on the three post holders.



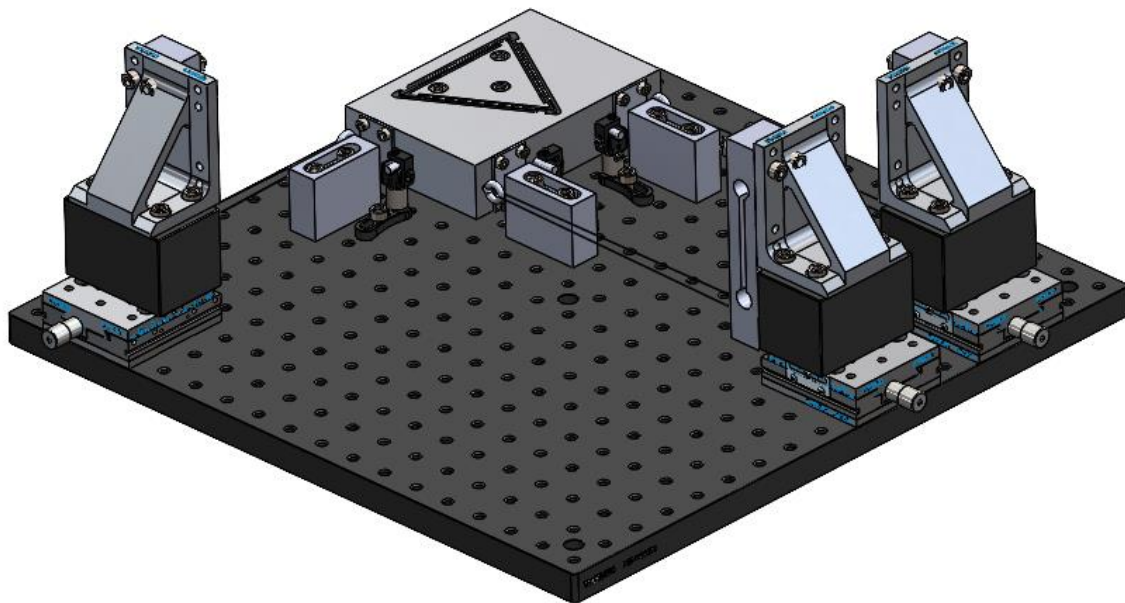
13. Secure these capacitive sensor holders to the bottom plate.



14. Secure the capacitive sensors such that the distance between the sensors and the chuck is 0.6mm . Use a feeler gauge to achieve this while the chuck is being kept in place by the ropes.



15. The test set up is ready for use.



Section 2: Glueing the balls to the ball holders

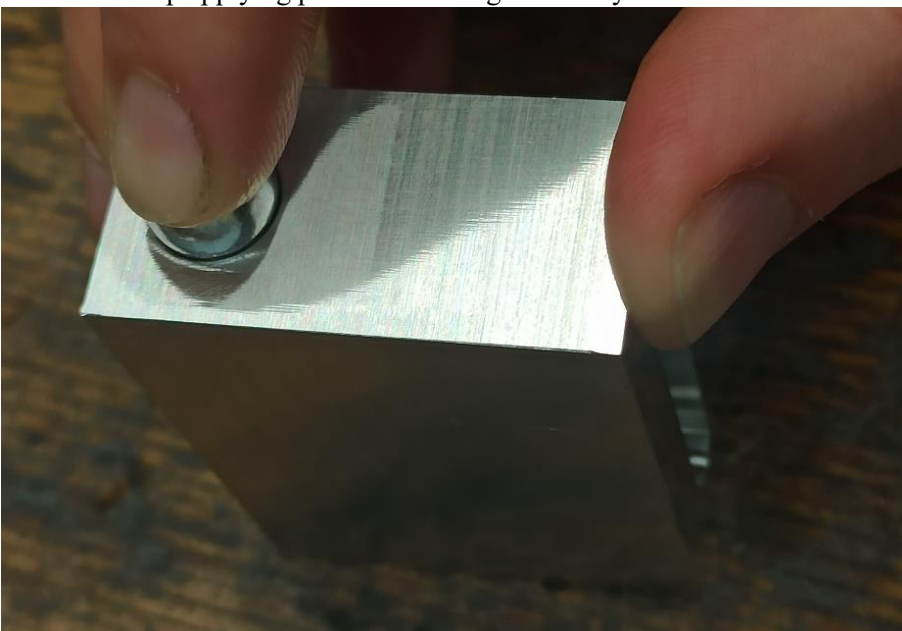
1. Mix the components of the Araldite 2021-1 and place the ball holder on a flat surface.



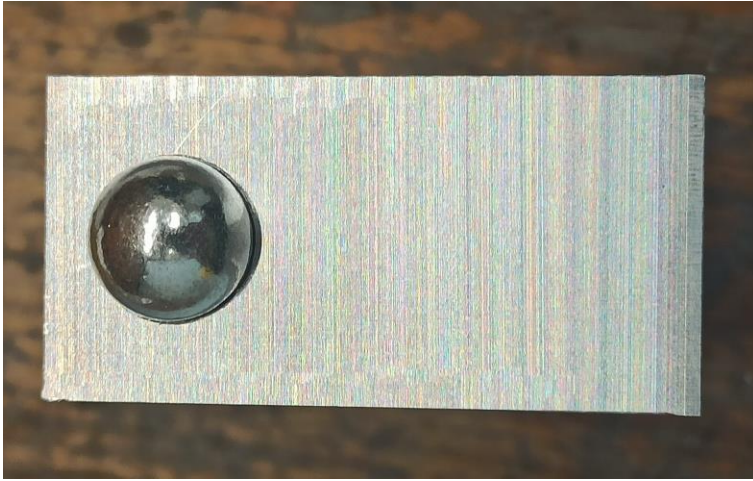
2. Apply glue in a circle in the cone of the ball holder.



3. Press the ball in the holder and hold for at least 4 minutes. Look at the mixed glue of the beginning to see if it dried and therefore turned yellow. If the mixed glue has not dried in those 4 minutes keep applying pressure till the glue is fully dried.



4. Leave the ball holder for at least 24 hours before applying pressure.



Appendix V: Determining offset value capacitive sensors

From (11) and (15) The normal displacements can be determined as

$$\begin{bmatrix} \delta_{n,1} \\ \delta_{n,2} \\ \delta_{n,3} \end{bmatrix} = \begin{bmatrix} 0 & 1 & \left(l_{c,1} - \frac{w}{2}\right) \\ 0 & 1 & \left(l_{c,2} - \frac{w}{2}\right) \\ 1 & 0 & \left(\frac{h}{2} - l_{c,3}\right) \end{bmatrix} \begin{bmatrix} 0 & 1 & \left(l_{s,1} - \frac{w}{2}\right) \\ 0 & 1 & \left(l_{s,2} - \frac{w}{2}\right) \\ 1 & 0 & \left(\frac{h}{2} - l_{s,3}\right) \end{bmatrix}^{-1} \left\{ \begin{bmatrix} y_{s,1} \\ y_{s,2} \\ x_{s,3} \end{bmatrix} + \epsilon \right\} \quad (35).$$

The offset ϵ needs to be determined based on measurements to reassure that $\begin{bmatrix} \delta_{n,1} \\ \delta_{n,2} \\ \delta_{n,3} \end{bmatrix} = 0$ when contact

is made. This point is clearly visible in the data as shown in Figure 16. Since there is no measurement data available where all points are exactly just touching, measurement data for three contacting points is needed to determine ϵ . During a test, the sensors are not the entire time within reach. Only when the final point makes contact this is the case, so three different tests are needed. The three data points are taken when balls come into contact with the surfaces, so not while releasing. For experiment B1 this

leads to $\epsilon_{B1} = \begin{bmatrix} -194 \\ -129 \\ -197 \end{bmatrix}$ and for B2 this gives $\epsilon_{B2} = \begin{bmatrix} -141 \\ -118 \\ -207 \end{bmatrix}$. There is a difference since the ball holders

have been moved in between the experiments.

Appendix W: Sensor noise test set-up

To map out the noise of the system a frequency response for all sensors is plotted (Figure 63). The results are shown up to the Nyquist frequency of the system.

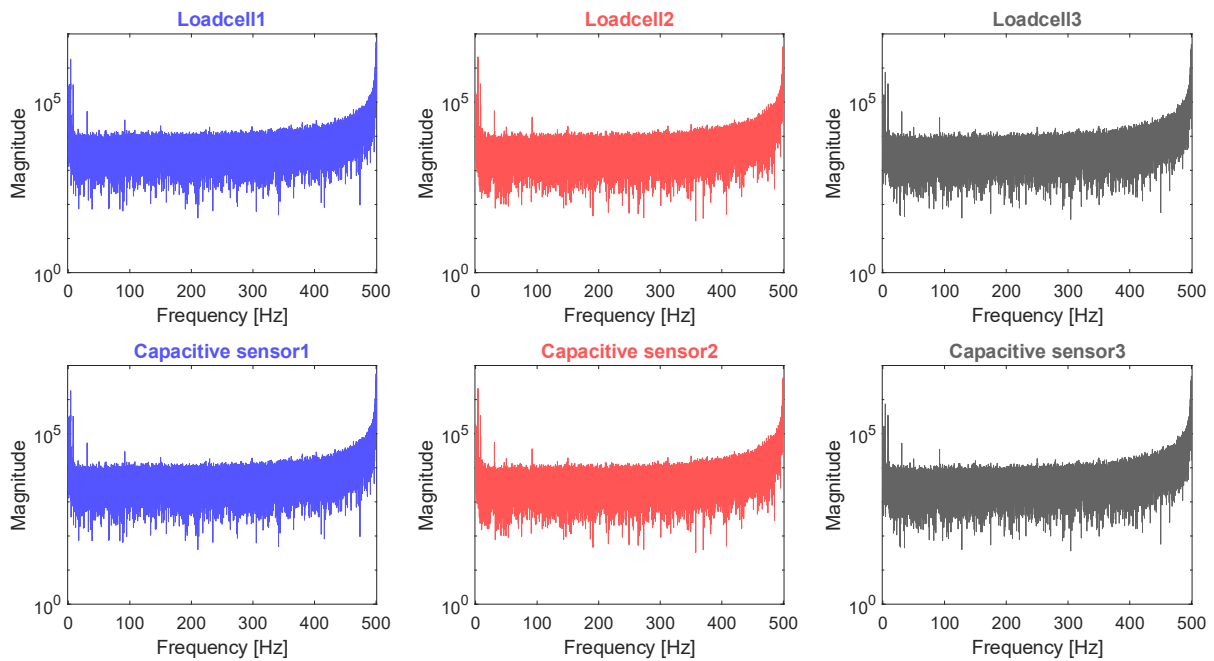


Figure 63: Frequency response for all measured signals when the test set-up is in resting state

It is clear from the figure that the values are approximately normally distributed. The influence seemingly goes up when getting closer to 500Hz, but noise with a higher frequency cannot be properly mapped. Putting a box over the test set-up, does not seem to make much of a difference (Figure 64). It is good to note that the data is measured over a short period of time, so a longer timespan might influence the results.

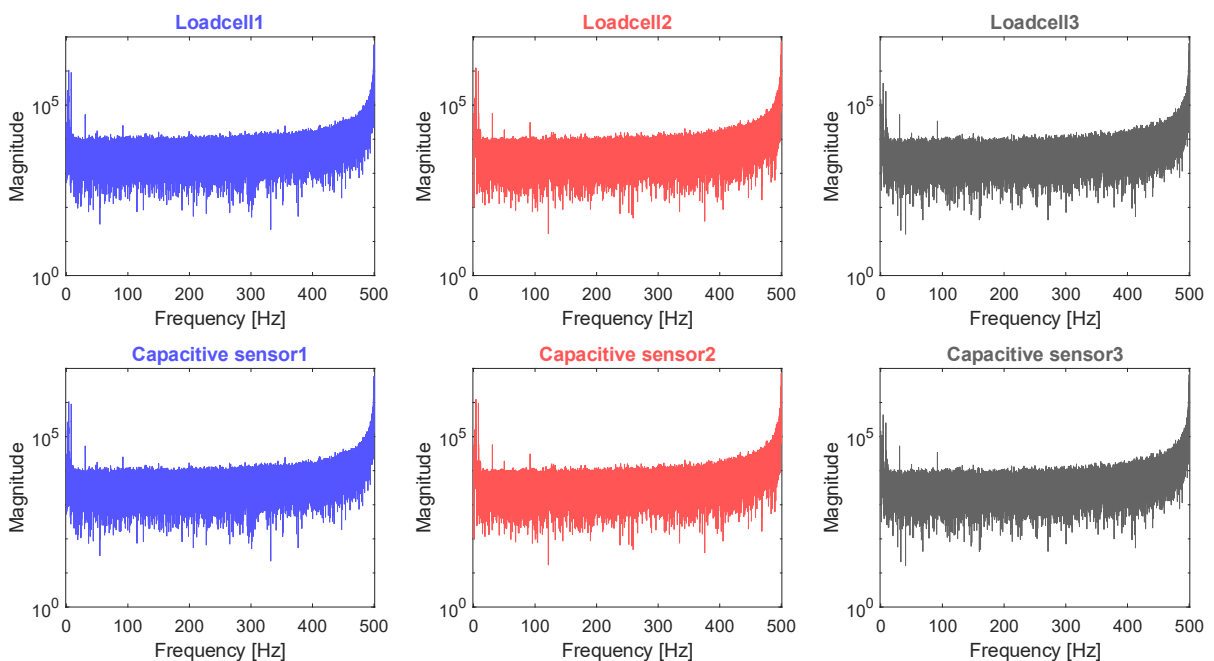


Figure 64: Frequency response for all measured signals while a box is placed over the test set-up

To have less influence of the noise, the measurements of the forces are averaged over 50 datapoints and the measurements of the capacitive sensors over 10 datapoints (Figure 65). The noise of the load cells clearly goes down, while the capacitive sensors do not change much. The sensors are already calibrated by the driver and mainly show variations due to movements of the chuck.

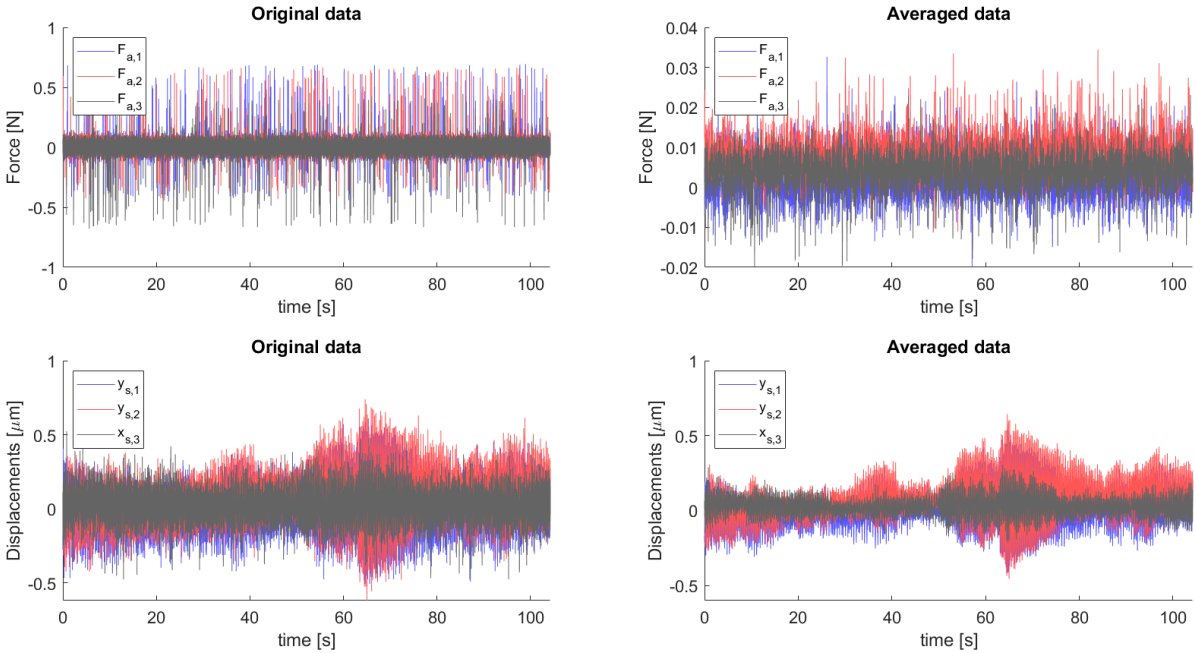


Figure 65: Measured data for the noise test without box and averaged measuring data

Appendix X: Determining the flexure stiffness

During the process of determining the flexure stiffness, no contact is made anywhere. Figure 66 shows the force-displacement plot when increasing $F_{a,2}$ while no other forces are applied to the chuck.

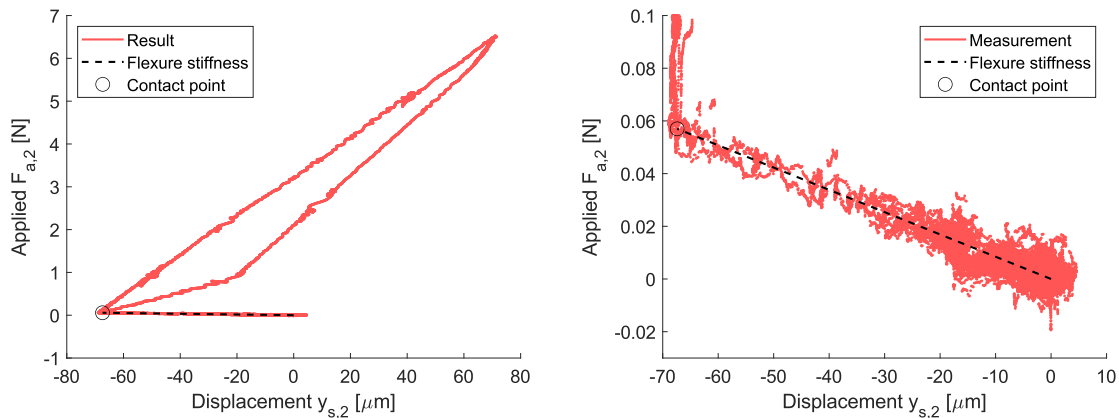


Figure 66: Results stiffness test without contact

The almost horizontal part of the figure resembles the stiffness of the leaf flexure mechanism. The stiffness is determined as 0.85N/mm which does match the 0.75N/mm calculated with SolidWorks quite closely (Appendix P). Both the force and displacement are not measured exactly at the contact. Since no other forces are applied, the applied force should resemble the contact force. The normal contact displacement could not be calculated, since the bigger rotations of the chuck let to the other sensors being out of reach.

The second part of the figure should resemble the contact stiffness, but this goes in the wrong direction. The chuck is likely rotating over the ball at the base, while sliding takes also place. A hysteresis curve presents itself when contact is made, which goes back to the contacting point. The test used to determine the contact stiffness is explained in chapter 4.

Appendix Y: Standard deviations experiment B

Table 26 shows the standard deviations for different alignment sequences based on the experiments B1 and B2.

Table 26: Standard deviations of the results of experiment B

Sequence	Spread	Value B1 [μm]	Value B2 [μm]
123	σ_x	0.33	0.38
	σ_y	0.28	1.02
231*	σ_x	0.33	–
	σ_y	0.20	–
132	σ_x	0.06	–
	σ_y	0.19	–
312	σ_x	0.93	0.59
	σ_y	0.33	0.54
231	σ_x	0.46	1.50
	σ_y	0.30	0.59
Total	σ_x	0.94	1.80
	σ_y	0.50	0.82